Università degli Studi di Perugia

Facoltà di Scienze Matematiche, Fisiche e Naturali

Dottorato di Ricerca in Fisica

XXII Ciclo

Tesi di Dottorato

Measurement of the $K^+ \to e^+\nu_e\gamma$ $(SD+)$ decay Branching Ratio with the NA62 experiment

Candidato

Roberto Piandani

Relatore

Prof.ssa Giuseppina Anzivino

Coordinatore

Prof. Maurizio Busso

Anno Accademico 2008-2009

Contents

Introduction

In this thesis the measurement of the Branching Ratio (BR) of the $K^+ \to e^+\nu_e\gamma$ SD+ decay is presented. This decay, together with the other radiative kaon decays, is one of the best environment to study the low energy effective theories as the Chiral Perturbation Theory (ChPT) or Light Front Quark Model (LFQM). The total amplitude of the $K^+ \to e^+\nu_e\gamma$ decay is a sum of "Inner Bremsstrahlung" (IB) and "Structure-Dependent" (SD) components, in addition to the IB and SD contributions also the interference between them is possible. The Structure-Dependent term has two components: the SD+ and the SD-, the sign is related to the polarization of the radiative photon. The IB contribution is derived from the $K^+ \to e^+\nu_e$ decay by the standard QED corrections. The Structure-Dependent part, related to the direct emission of the photon by the kaon, is predicted by the ChPT and LFQM.

The present work is based on part of the Data collected in summer 2007 by the NA62 experiment at the CERN Super-Proton-Synchrotron (SPS). The NA62 experiment consists of two phases, the phase 1, 2007 and 2008 Data taking, aims to measure the ratio of the decay amplitudes of the $K^+ \to e^+\nu_e$ and $K^+ \to \mu^+\nu_\mu$ decays, $R_K = \Gamma(K_{e2})/\Gamma(K_{\mu 2})$ exploiting the detector of the previous NA48 experiment. On the Standard Model (SM) framework this ratio is known with a good prediction, under the permill level; as a consequence of it, R_K is a sensitive test for the Lepton Universality and for New Physics beyond the SM.
Concerning R_K measurement, a detailed study of the $K^+ \to e^+\nu_e\gamma$ is fundamental to separate the IB component (to be included on R_K) from the SD components (representing a potential background to R_K).
The NA62 phase 2 aims to measure the BR of the ultra-rare kaon decay $K^+ \to \pi^+\nu\bar{\nu}$. The present experimental knowledge of this process is based on few events and doesn't have statistical power to distinguish between the SM theoretical prediction and models beyond it.

This thesis is organised in the following way:
In chapter 1, the theoretical motivation of the measurements is given, together with the underlying theoretical tools, and then the present experimental status is shown.

Chapter 2 contains the detailed descriptions of the beam line, the apparatus, the trigger and Data acquisition systems of the NA48/2 experiment, which are re-used in the first phase of NA62.

In order to check the theoretical predictions, a detailed Monte-Carlo (MC) simulation, presented in chapter 3, is used to compare and verify the expected MC distributions with the Data. The quantities derived by the simulation are essential for the BR measurement, in fact the signal and the normalization acceptances and the background contributions are estimated with MC events.

The set of cuts and conditions giving the signal selection are introduced in chapter 4.

Chapter 5 lists the set of cuts and conditions used to select the normalization channel $K^+ \to e^+\pi^0\nu_e$ used to estimate the kaon flux.

The results of the $K^+ \to e^+\nu_e\gamma$ SD+ BR are presented in chapter 6 together with the background evaluation and the study of systematic effects.

Chapter 1

Theoretical Introduction

Rare kaon decays offer the possibility of probing high energies scales by doing precise low energy measurements: the precision is obtained by looking at very rare decays and the advantage of the kaon system is the long lifetime of both K_L and $K^{\pm}$.

Depending on the type of particles involved in the final states, all decays can be grouped in different categories such as radiative, hadronic, leptonic etc . Radiative kaon decays, dominated by long distance physics, are sensitive to the nonpertubative aspects of the Quantum Chromo Dynamics (QCD) [1, 2] and, therefore, they cannot be reliably predicted. At present a convenient framework to study these decay modes is the Chiral Perturbation Theory. Within that model, the lack of information on strong interaction dynamics is parameterized in terms of a few unknown coupling constants that can be measured in some processes and then used to predict additional decay modes. Another available framework is the LFQM that uses a new definition of the time to quantizing the relativistic field theory to perform calculation at low energy QCD.

1.1 Chiral Perturbation Theory

Chiral Perturbation Theory provides a systematic framework for investigating strong interaction at low energies, as opposed to a pertubative treatment of QCD in terms of the running coupling constant.

At very low energies, below the resonance region ($E < M_\rho$), the hadronic spectrum contains only the octet of very light pseudoscalar mesons (π, K, η), whose interactions can be described using global symmetry considerations. This has allowed the development of a powerful theoretical framework, the Chiral Perturbation Theory, to analyze the low energy implications of the QCD symmetries. This formalism is based on two key ingredients: the concept of effective field theory [3, 4]

and the chiral symmetry properties of QCD Lagrangian [5]. The 8 pseudoscalar mesons can be associated to the multiplet of massless Goldstone bosons [6] arising from the spontaneous breakdown of the chiral symmetry.

At the lowest order in quarks momenta $O(p^2)$, the most general chiral Lagrangian compatible with Lorentz invariance and local chiral symmetry can be expressed in terms of only two parameters [7], f_π and B_0:

$$\mathcal{L}_2 = \frac{f_\pi^2}{4} Tr[D_\mu U (D^\mu U)^\dagger] + \frac{f_\pi^2}{4} Tr[\chi U^\dagger U \chi^\dagger] \tag{1.1}$$

where D_μ is the covariant derivative, U is a unitary matrix done in terms of a matrix of mesons field

$$U = exp\left[i\frac{\sqrt{(}2)}{f_\pi} \begin{pmatrix} \frac{\pi^0}{\sqrt{(}2)} + \frac{\eta}{\sqrt{(}6)} & \pi^+ & K^+ \\ \pi^- & \frac{-\pi^0}{\sqrt{(}2)} + \frac{\eta}{\sqrt{(}6)} & K^0 \\ K^- & \bar{K^0} & \frac{-2\eta}{\sqrt{(}6)} \end{pmatrix} \right],$$

and χ is defined as

$$\chi = 2B_0(s + ip)$$

where s and p the scalar and pseudoscalar quark densities. The constant f_π is the pion decay constant, which can be measured in decay $\pi \to \mu\nu$ ($f_\pi = 92.4$ MeV) while B_0 is not fixed by symmetry consideration only [8], but can be related to the quark condensate. Due to the fact that both f_π and B_0 are fixed, the ChPT can now provide absolute predictions of physical quantities. The nice features of the chiral approach is moreover the possibility to have a systematic estimate of higher order corrections. To perform calculations at the next to leading order in momenta, $O(p^4)$, the following ingredients are necessary:

1. The effective Lagrangian at order $O(p^4)$, $\mathcal{L}_4$ (eq. 1.2), to be considered at tree level;

2. The one loop graph associated with $\mathcal{L}_2$ Lagrangian (eq. 1.1);

3. The Wess Zumino [9] Witten [10] functional to take into account the chiral anomaly.

To evaluate the next to next to leading order calculation, $O(p^6)$, a much more complicated prescription has to be followed which involves different ingredients:

1. The effective Lagrangian at order $O(p^6)$, $\mathcal{L}_6$, to be considered at tree level;

2. The two loops graphs associated with $\mathcal{L}_2$ Lagrangian (eq. 1.1);

3. The one loop graphs associated with $\mathcal{L}_4$ Lagrangian (eq. 1.2);

4. The quantum correction to Wess Zumino Witten functional.

$$\begin{aligned}\mathcal{L}_4 &= L_1 Tr[D_\mu U (D^\mu U)^\dagger]^2 + L_2 Tr[D_\mu U (D_\nu U)^\dagger] Tr[D^\mu U (D^\nu U)^\dagger] \\ &+ L_3 Tr[D_\mu U (D^\mu U)^\dagger D_\nu U (D^\nu U)^\dagger] + L_4 Tr[D_\mu U (D^\mu U)^\dagger] Tr[\chi U^\dagger + U\chi^\dagger] \\ &+ L_5 Tr[D_\mu U (D^\mu U)^\dagger \chi U^\dagger + U\chi^\dagger] + L_6 [Tr(\chi U^\dagger + U\chi^\dagger)]^2 \\ &+ L_7 [Tr(\chi U^\dagger - U\chi^\dagger)]^2 + L_8 Tr(U\chi^\dagger U\chi^\dagger + \chi U^{\dagger\chi U^\dagger}) \\ &- iL_9 Tr[f^R_{\mu\nu} D^\mu U (D^\nu U)^\dagger + f^L_{\mu\nu} (D^\mu U)^\dagger (D^\nu U)] + L_{10} Tr(U f^L_{\mu\nu} U^\dagger f^{\mu\nu}_R) \\ &+ H_1 Tr(f^R_{\mu\nu} f^{\mu\nu}_R + f^L_{\mu\nu} f^{\mu\nu}_L) + H_2 Tr(\chi\chi^\dagger)\end{aligned} \tag{1.2}$$

In equation 1.2, L_i are the low-energy unrenormalized coupling constants and H_1 and H_2 are coupling constants with the field-strength tensors of external sources $f^R_{\mu\nu}$ and $f^L_{\mu\nu}$.

The number of unknown parameters increases as a function of the order of calculation. Nevertheless many of them can be extracted using low energy phenomenology, and not all the parameters are used to get particular prediction, therefore many kind of precesses can be computed using this theoretical tool. For more details on the ChPT see [8].

1.2 The Light Front Quark Model

The foundations of light-front (LF) quantization date back to Dirac [11] who showed that there are remarkable advantages in quantizing relativistic field theories at a particular value of delayed LF time $\tau = t + z/c$ rather than at a particular ordinary time t, where z is the position at the time t of the LF. In this formalism, a hadron is characterized by a set of Fock state functions representing the probability amplitudes for finding different combinations of bare quarks and gluons in the hadron at a given LF time τ. For example, a meson can be described by:

$$|M> = \sum_{q\bar{q}} \psi_{q\bar{q}/M} + \sum_{q\bar{q}g} \psi_{q\bar{q}g} |q\bar{q}g> \psi_{q\bar{q}g/M} + ... \tag{1.3}$$

These wave functions provide the essential link between hadronic phenomena at short distances (perturbative) and at long distances (non-perturbative).

For a particle with mass m and four-momentum $k = (k^0, k^1, k^2, k^3)$, the rela-

tivistic energy-momentum relation at equal-τ is given by

$$k^- = \frac{\mathbf{k}_\perp^2 + m^2}{k^+} \tag{1.4}$$

where the LF energy conjugate to τ is given by $k^- = k^0 - k^3$ and the LF momenta $k^+ = k^0 + k^3$ and $\mathbf{k}_\perp = (k^1, k^2)$ are orthogonal to k^- and form the LF three-momentum $\underline{k} = (k^+, \mathbf{k}_\perp)$. The rational relation given by equation 1.4 is drastically different from the irrational energy-momentum relation at equal-t given by

$$k^0 = \sqrt{\underline{k}^2 + m^2} \tag{1.5}$$

where the energy k^0 is conjugate to t and the three-momentum vector $\underline{k}$ is given by $\underline{k} = (k^1, k^2, k^3)$.

The important point here is that the signs of k^+ and k^- are correlated and thus the momentum k^+ is always positive because only the positive energy k^- makes the system to evolve to the future direction (i.e. positive τ), while at equal-t the signs of k^0 and $\underline{k}$ are not correlated and thus the momentum k^3 corresponding to k^+ at equal-τ can be either positive or negative. This provides a remarkable feature to the LF vacuum; the trivial vacuum of the free LF theory is an eigenstate of the full Hamiltonian.

This apparent simple description of the LF vacuum may yield a problem to understand the novel phenomena such as the spontaneous symmetry breaking and chiral symmetry breaking, because these were known as the direct consequences of the nontrivial vacuum structure of the various field theories. Nontrivial vacuum phenomena can still be realized in the LF quantization approach if one takes into account the nontrivial zero-mode ($k^+ = 0$) contributions [12].

The distinguished features in the LF approach are the dynamical property of rotation operators and the simplicity of the vacuum except the zero modes ($k^+ = 0$) [13]. In the LF quantization method, one can take advantage of the rational energy-momentum dispersion relation, equation 1.4, and build a clean Fock state expansion (similar to equation 1.3) of hadronic wave function based on a simple vacuum by decoupling the complicated nontrivial zero modes ($k^+ = 0$). The decoupling of zero modes can be achieved in the LFQM since the constituent quark and antiquark acquire appreciable constituent masses.

One meson bound state $|M>$ is represented by

$$|M> = \Psi^M_{Q\bar{Q}}|Q\bar{Q}>$$

where Q and $\bar{Q}$ are the effective dressed quark and antiquark. The model wave function in momentum space is given by

$$\Psi^M_{Q\bar{Q}} = \Psi^{JJ_3}_{\lambda_q\lambda_{\bar{q}}}(z,\mathbf{k}_\perp) = \sqrt{\frac{\partial k_n}{\partial z}}\phi(z,\mathbf{k}_\perp)\mathcal{R}^{JJ_3}_{\lambda_q\lambda_{\bar{q}}}(z,\mathbf{k}_\perp) \tag{1.6}$$

where $\phi(z,\mathbf{k}_\perp)$ is the radial wave function, $\frac{\partial k_n}{\partial z}$ is a Jacobi factor, and $\mathcal{R}^{JJ_3}_{\lambda_q\lambda_{\bar{q}}}(z,\mathbf{k}_\perp)$ is the spin-orbit wave function.

1.3 The $K^+ \to e^+\nu_e\gamma$ decay

The importance to study the $K^+ \to e^+\nu_e\gamma$ decay is that this process, as it will be shown later in this section, is sensible to the various theoretical models introduced in the previous sections and it allows to distinguish between them.

It is known that the radiative decays of $K^+ \to l^+\nu_l$, the $K^+ \to l^+\nu_l\gamma$ ($l = e, \mu$), receive two types of contribution to the total decay amplitude: "Inner Bremsstrahlung" (IB) and "Structure-Dependent" (SD), known also as Direct Emission (DE) [15, 16]; between the IB and the SD component there is a term of interference. Figure 1.1 shows the diagrams contributing to the decay. The SD contribution has two components: the SD+ and the SD-, the sign is related to the polarization of the radiative photon. While the IB component of the $K^+ \to e^+\nu_e\gamma$ decay is still helicity suppressed, as the $K^+ \to e^+\nu_e$ one, and contains the electromagnetic coupling constant α as well, the SD part gives the dominant contribution to the decay rate as it is free of helicity suppression. Similarly, the SD contribution is also important to the decay $K^+ \to \mu^+\nu_\mu\gamma$.

In the SM the decay amplitude of the SD part involves vector and axial-vector hadronic currents, that can be parametrized in terms of the vector form factor F_V and axial-vector form factor F_A. Theoretical calculation of F_V and F_A for the $K^+ \to X\gamma$ transition, where X represents every system of particles (leptons or hadrons), have been done in the ChPT at $O(p^4)$ [17] and $O(p^6)$ [18, 19, 20] and in the LFQM [20, 21, 22] frameworks.

1.3.1 Matrix elements and form factors

The decay amplitude, M of $K^+ \to e^+\nu_e\gamma$ can be written in terms of IB and SD contribution in the following way:

$$M = M_{IB} + M_{SD}$$

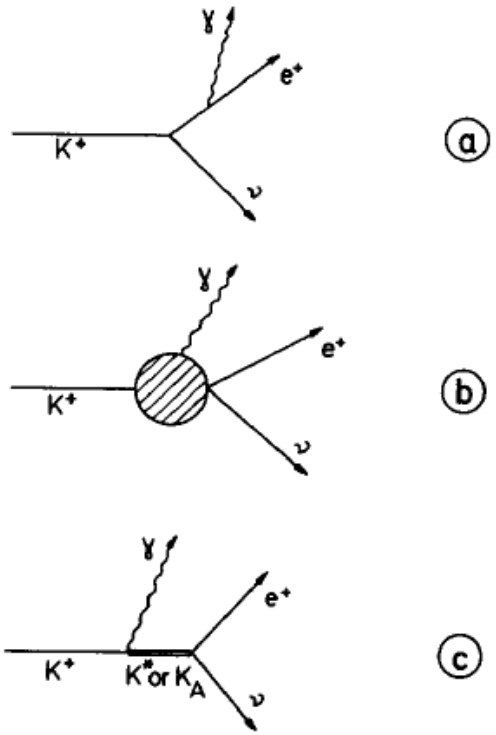

Figure 1.1: Diagrams contributing to $K^+ \to e^+\nu_e\gamma$ decay. (a) Inner Bremsstrahlung, (b) Structure-Dependent and (c) Structure-Dependent term with K^* and K_A mesons as intermediate states.

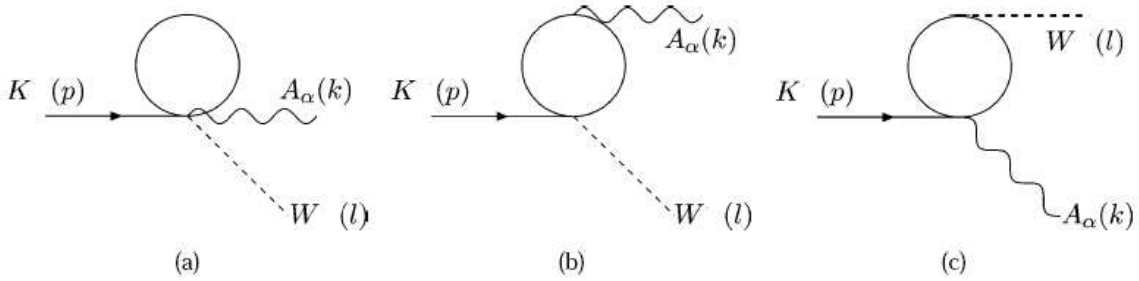

Figure 1.2: One-loop diagrams contributing to F_V

$$M_{IB} = ie\frac{G_F}{\sqrt{2}} sin\theta_c f_K m_e \epsilon^*_\alpha K^\alpha \tag{1.7}$$

$$M_{SD} = -ie\frac{G_F}{\sqrt{2}} sin\theta_c \epsilon^*_\mu L_\nu H^{\mu\nu}$$

where

$$K^\alpha = \bar{u}(p_\nu)(1+\gamma_5)\Big(\frac{p_K^\alpha}{p_K\cdot q} - \frac{2p_e^\alpha + \not{q}\gamma^\alpha}{2p_e\cdot q}\Big)v(p_e)$$

$$L_\nu = \bar{u}(p_\nu)\gamma_\nu(1-\gamma_5)v(p_e) \tag{1.8}$$

$$H^{\mu\nu} = \frac{F_A}{m_K}(-g^{\mu\nu}p_K\cdot q + p_K^\mu q^\nu) + i\frac{F_V}{m_K}\epsilon^{\mu\nu\alpha\beta}q_\alpha p_{K\beta}$$

$\epsilon_{\alpha,\mu}$ is the photon polarization vector, G_F is the Fermi constant, θ_c is the Cabibbo angle, f_K is the kaon decay constant, m_K is the kaon mass, p_K, p_ν, p_e, and q are the four-momenta of K^+, ν_e, e^+, and γ, and $F_{A(V)}$ are the axial-vector(vector) form factors. In the framework of ChPT at $O(p^6)$ the vector form factor F_V for $K^+ \to e^+\nu_e\gamma$ [18, 19, 20] can be written as:

$$\begin{aligned}
F_V(p^2) = \frac{m_K}{4\sqrt{2}\pi^2 f_K}\Big\{1 &- \frac{256}{3}\pi^2 m_K^2 C_7^r + 256\pi^2(m_K^2 - m_\pi^2)C_{11}^r + \frac{64}{3}\pi^2 p^2 C_{22}^r \\
&- \frac{1}{16\pi^2(\sqrt{2}f_K)^2}\Big[\frac{3}{2}m_\eta^2 \ln\Big(\frac{m_\eta^2}{\mu^2}\Big) + \frac{7}{2}m_\pi^2 \ln\Big(\frac{m_\pi^2}{\mu^2} + 3m_k^2 \ln\Big(\frac{m_K^2}{\mu^2}\Big) \\
&- 2\int [xm_\pi^2 + (1-x)m_K^2 - x(1-x)p^2] \times \ln\Big(\frac{xm_\pi^2 + (1-x)m_K^2 - x(1-x)p^2}{\mu^2}\Big)dx \\
&- 2\int [xm_\eta^2 + (1-x)m_K^2 - x(1-x)p^2] \times \ln\Big(\frac{xm_\eta^2 + (1-x)m_K^2 - x(1-x)p^2}{\mu^2}\Big)dx \\
&- 4\int m_\pi^2 \ln\Big(\frac{m_\pi^2}{\mu^2}\Big)\Big]\Big\}
\end{aligned} \tag{1.9}$$

where C_i^r are the renormalized coefficients [23] , m_π and m_η are the masses oh the pion and of the η meson, $p^2 = (p_K - q)^2$ and $x = \frac{p_K\cdot q}{2m_K^2}$. In the F_V computation

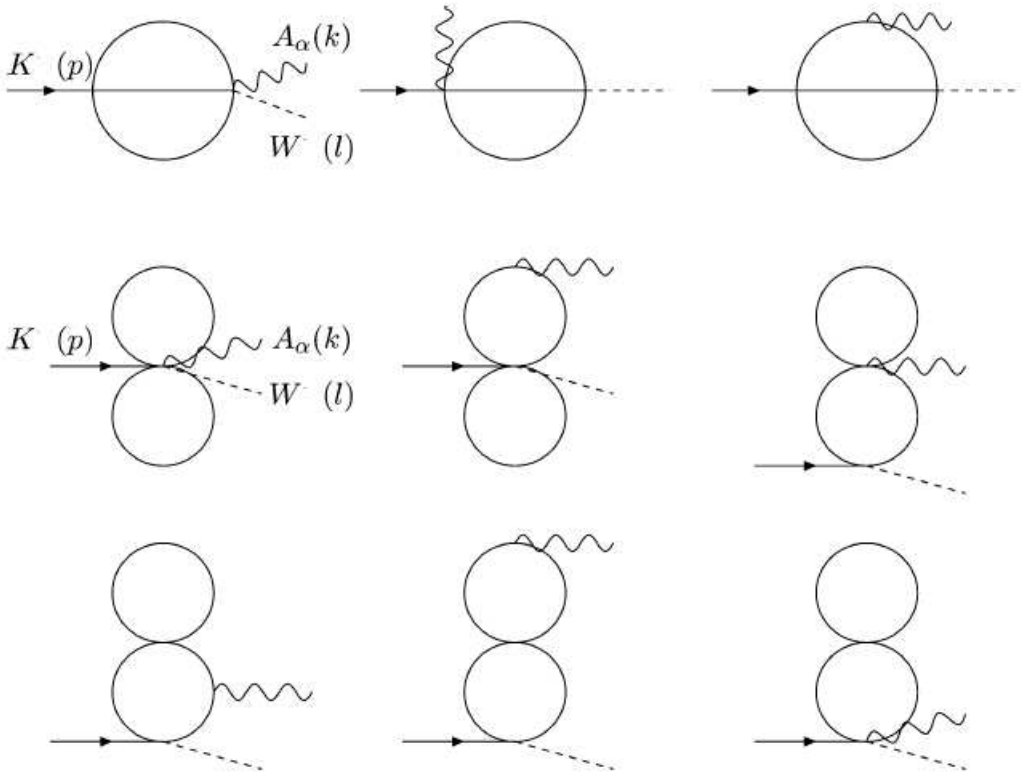

Figure 1.3: Two-loop diagrams contributing to F_A

only the tree level diagrams and the one-loop diagrams of figure 1.2 enter. The axial-vector form factor F_A at $O(p^6)$ can be written as [19, 20]:

$$\begin{aligned}
F_A(p^2) = {} & \frac{4\sqrt{2}m_K}{f_K}(L_9^r + L_{10}^r) + \frac{m_K}{6f_K^3(2\pi)^8}[142.65(m_K^2 - p^2) - 198.3] \\
& - 4\frac{m_K}{4\sqrt{2}f_K^3\pi^2}\Big\{(4L_3^r + 7L_9^r + 7L_{10}^r)m_\pi^2 \ln\left(\frac{m_\pi^2}{m_\rho^2}\right) + 3(L_9^r + L_{10}^r)m_\eta^2 \ln\left(\frac{m_\eta^2}{m_\rho^2}\right) \\
& + 2(8L_1^r - 4L_2^r + 4L_3^r + 7L_9^r + 7L_{10}^r)m_K^2 \ln\left(\frac{m_K^2}{m_\rho^2}\right)\Big\} \\
& - \frac{4\sqrt{2}m_K}{3f_K^3}\{2m_\pi^2(18y_{18}^r - 2y_{81}^r - 6y_{82}^r + 2y_{83}^r + 3y_{84}^r - y_{85}^r + 6y_{103}^r) \\
& + 2m_K^2(18y_{17}^r + 36y_{18}^r - 4y_{81}^r - 12y_{82}^r + 4y_{83}^r + 6y_{84}^r + 4y_{85}^r - 3y_{100}^r + 6y_{102}^r \\
& + 12y_{103}^r - 6y_{104}^r + 3y_{109}^r) + \frac{3}{2}(m_K^2 - p^2)(2y_{100}^r - 4y_{109}^r + y_{110}^r)\}
\end{aligned} \tag{1.10}$$

where L_i^r and y_i^r are the renormalized coupling constants [24, 25]. The tree level diagrams, the one-loop diagrams, figure 1.2 (a) and (b) and the two-loops diagrams

of figure 1.3 contribute to the F_A calculation. In reality, for the F_A determination, the only possible non-vanishing diagrams of figure 1.3 are the first three irreducible ones because the last six can be seen as a product of one-loop integrals and they don't give terms proportional to $(p \cdot q)$ necessary for the construction of F_A. Note that the first terms in 1.9 and 1.10 correspond to F_V and F_A at $O(p^4)$ [17], respectively.

In the framework of LFQM the expressions for F_V and F_A become [20]:

$$F_V(p^2) = 8m_K \int \frac{dzd^2K_\perp}{2(2\pi)^3}\Phi(z',k_\perp^2)\frac{1}{z-z'}\Big\{\frac{2}{3}\frac{m_u - z'(m_s-m_u)k_\perp^2\Theta}{m_u^2+k_\perp^2} - \frac{1}{3}\frac{m_s+(1-z')(m_s-m_u)k_\perp^2\Theta}{m_s^2+k_\perp^2}\Big\} \tag{1.11}$$

$$F_A(p^2) = 4m_K \int \frac{dzd^2K_\perp}{2(2\pi)^3}\Phi(z',k_\perp^2)\frac{1}{z-z'}\Big\{\frac{2}{3}\frac{m_u - Ak_\perp^2\Theta}{m_u^2+k_\perp^2} - \frac{1}{3}\frac{m_s+Bk_\perp^2\Theta}{m_s^2+k_\perp^2}\Big\} \tag{1.12}$$

where $A = (1-2z)z'(m_s-m_u) - 2zm_u$, $B = (1-2z)z'm_s + m_s + (1-2z)(1-z')m_u$, $\Phi(z',k_\perp^2)$ is the wave function of the quark, $z' = z(1-\frac{p^2}{M_K^2})$, $m_{u(s)}$ is the mass of quark u(s) and Θ is the derivative of the Φ respect to $K_\perp^2$.

1.3.2 Differential decay rate for the $K^+ \to e^+\nu_e\gamma$ decay

In order to describe the kinematics of $K^+ \to e^+\nu_e\gamma$ decay , the two variables x and y, are introduced:

$$x = \frac{2E_\gamma^*}{m_K}, \quad y = \frac{2E_e^*}{m_K}$$

with the following constraints:

$$0 \le x \le 1 - r_e, \quad 1 - x + \frac{r_e}{1-x} \le y \le 1 + r_e, \tag{1.13}$$

where E_γ^* and E_e^* are the energies of the photon and positron in the kaon rest frame, respectively, and $r_e = m_e^2/m_K^2$. The relation between the transfer momentum p^2 and x is given by:

$$p^2 = m_K^2(1-x).$$

In the K^+ rest frame, the partial decay rate for $K^+ \to e^+\nu_e\gamma$ is given by

$$d\Gamma = \frac{1}{(2\pi)^3}\frac{1}{8m_K}|M|^2 dE_\gamma^* dE_e^*, \tag{1.14}$$

using equations 1.7 and 1.14, the double differential decay rate can be derived

$$\frac{d^2\Gamma}{dxdy} = \frac{m_K^5}{64\pi^2}\alpha G_F^2 \sin^2\theta_c(1-\lambda)A(x,y), \tag{1.15}$$

where $\lambda = (x + y - 1 - r_e)/x$, and

$$A(x,y) = A_{IB}(x,y) + A_{SD+}(x,y) + A_{SD-}(x,y) + A_{INT+}(x,y) + A_{INT-}(x,y). \quad (1.16)$$

By integrating over the y variable in equation 1.15, the differential decay rate is obtained as a function of x

$$\frac{d\Gamma}{dx} = \frac{m_K^5}{64\pi^2}\alpha G_F^2 \sin^2\theta_c A(x) \quad (1.17)$$

where $A(x)$ represents the no constant part of the decay amplitude with the following explicit x dependence

$$\begin{aligned}
A_{IB}(x) &= \frac{4r_e f_K^2}{m_K^2}\Big[\frac{(x+r_e-1)[x^2+4(1-r_e)(1-x)]}{1-x} - \frac{x^2+2(1-r_e)(1-x+r_e)}{x} \\
&\quad \ln\frac{r_e}{1-x}\Big] \\
A_{SD+}(x) &= |F_V + F_A|^2 x^3\Big[\frac{1-x}{3} - \frac{r_e}{2} + \frac{r_e^3}{6(1-x)^2}\Big] \\
A_{SD-}(x) &= |F_V - F_A|^2 x^3\Big[\frac{1-x}{3} - \frac{r_e}{2} + \frac{r_e^3}{6(1-x)^2}\Big] \\
A_{INT+}(x) &= \frac{4r_e}{m_K} Re[f_K(F_V+F_A)^*]x\Big[\frac{1-x}{2} - \frac{r_e^2}{2(1-x)} + r_e\ln\frac{r_e}{1-x}\Big] \\
A_{INT-}(x) &= \frac{4r_e}{m_K} Re[f_K(F_V-F_A)^*]x\Big[\frac{-1+3x}{2} + \frac{r_e^2-2xr_e}{2(1-x)} + (x-r_e)\ln\frac{r_e}{1-x}\Big]
\end{aligned} \quad (1.18)$$

1.3.3 Numerical results

The behaviour of F_A and F_V as a function of the squared transfered momentum in the ChPT at $O(p^4)$, at $O(p^6)$ and in the LFQM are shown in figure 1.4. As it can be seen from the figures, the vector F_V and axial-vector F_A form factors at $O(p^4)$ are constants, as calculated in [17], while at $O(p^6)$ they exhibit a linear dependence from p^2 or, equivalently, from x; in the LFQM the x dependence is more complex.

To show the behaviour of the different contributions obtained with the ChPT and LFQM calculations, the IB and $SD^{\pm}$ parts of the differential decay Branching Ratio as a function of x are reported in figure 1.5(left). In the small x region, there is an enhancement for the IB part, whereas the $SD^{\pm}$ components are close to zero. The spectra of the differential decay Branching Ratio with respect to x in ChPT at $O(p^4)$, $O(p^6)$, and in the LFQM are plotted in figure 1.5(right). it can be seen that in the region $x < 0.7$ the decay Branching Ratio predicted in the LFQM is much smaller than the one in the ChPT. On the other hand, in the region $x > 0.7$

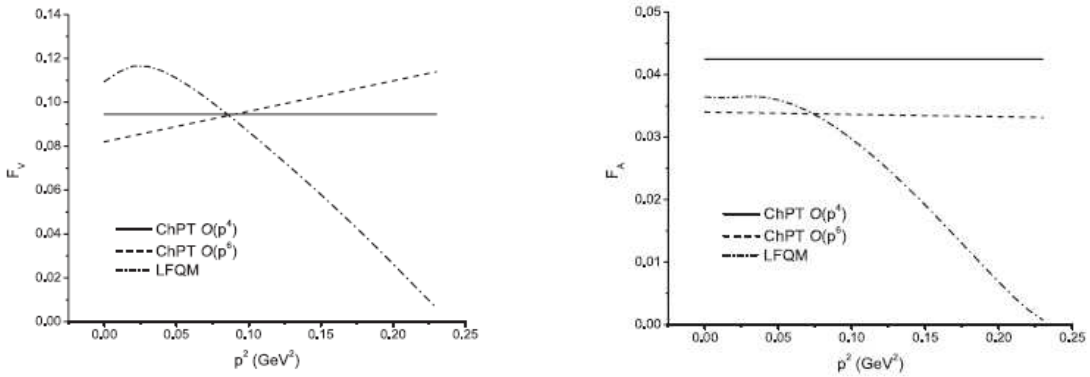

Figure 1.4: (Left) F_V as a function of the squared transfered momentum. (Right) F_A as a function of the squared transfer momentum [20].

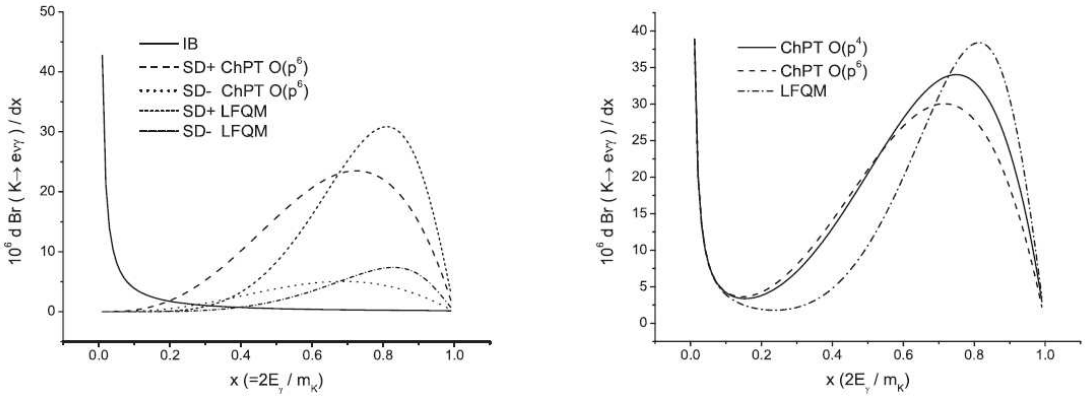

Figure 1.5: (Left) The IB and $SD^{\pm}$ parts of the differential Branching Ratio as a function of x. (Right) The differential Branching Ratio as a function of x [20].

the behaviour is reversed. The Branching Ratio of $K^+ \to e^+\nu_e\gamma$ decay can be calculated integrating over the variable x in equation 1.17. The results are reported in table 1.1 for (a) ChPT at $O(p^4)$, (b) ChPT at $O(p^6)$ and (c) the LFQM. The cuts

Model	Cut	IB	SD^+	SD^-	INT^+	INT^-	Total
(a)	x = 0.01	$1.65 \cdot 10^{-1}$	1.34	$1.93 \cdot 10^{-1}$	$6.43 \cdot 10^{-5}$	$-1.10 \cdot 10^{-3}$	1.70
	x = 0.1	$0.69 \cdot 10^{-1}$	1.34	$1.93 \cdot 10^{-1}$	$6.43 \cdot 10^{-5}$	$-1.10 \cdot 10^{-3}$	1.60
(b)	x = 0.01	$1.65 \cdot 10^{-1}$	1.15	$2.58 \cdot 10^{-1}$	$6.22 \cdot 10^{-5}$	$-1.21 \cdot 10^{-3}$	1.57
	x = 0.1	$0.69 \cdot 10^{-1}$	1.15	$2.58 \cdot 10^{-1}$	$6.22 \cdot 10^{-5}$	$-1.21 \cdot 10^{-3}$	1.47
(c)	x = 0.01	$1.65 \cdot 10^{-1}$	1.12	$2.59 \cdot 10^{-1}$	$4.33 \cdot 10^{-5}$	$-1.29 \cdot 10^{-3}$	1.54
	x = 0.1	$0.69 \cdot 10^{-1}$	1.12	$2.59 \cdot 10^{-1}$	$4.33 \cdot 10^{-5}$	$-1.29 \cdot 10^{-3}$	1.44

Table 1.1: The Branching Ratio of $K^+ \to e^+\nu_e\gamma$ decay (in units of 10^{-5}) in (a) ChPT at $O(p^4)$, (b) ChPT at $O(p^6)$ and (c) the LFQM with the cuts x = 0.01 and x = 0.1, respectively [20].

at $x = 0.01$ or $x = 0.1$ are the lower extremes of the integrals because for $x \to 0$, or

equivalently $p^2 \to p^2_{max}$, the IB term diverges.

1.4 Experimental status

The PDG 2008 [14] quotes

$$BR(K^+ \to e^+\nu_e\gamma(SD^+)) = (1.53 \pm 0.23) \cdot 10^{-5}$$

resulting from a combination of two counting experiments at CERN [26, 27], both of which were sensitive mainly to the SD^+ term. In [26], 56 events with $E^*_\gamma > 100\ MeV$, $E^*_e > 236\ MeV$ and $\theta^*_{e\gamma} > 120°$ have been identified, whereas the other experiment [27] has collected 51 events with $E^*_\gamma > 48\ MeV$, $E^*_e > 235\ MeV$ and $\theta^*_{e\gamma} > 140°$. In these kinematical regions, background from $K^+ \to e^+\pi^0\nu_e$ decay (Ke3) is kinematically suppressed because $E^{*max}_e(K_{e3}) = 228 MeV$. For their calculations the two experiments consider constant form factors like the ChPT at $O(p^4)$ model prediction.

Comparing the experimental value and the theoretical one from table 1.1 it can be seen that the various theoretical models predict a Branching Ratio smaller than the experimentally measured one.

As a consequence of the large experimental error ($\sim 15\%$), the current measurement is not able to discriminate between the theoretical models; it is important to increase the number of signal events to start a valid discrimination among the models.

A new measurement of the Branching Ratio is necessary also to obtain a precise estimation of $K^+ \to e^+\nu_e\gamma$ (SD+) contribution to the background of the $K^+ \to e^+\nu_e$ decay in the R_K ratio, the main motivation of the NA62 phase I experiment.

Finally, to complete the knowledge of the entire process $K^+ \to e^+\nu_e\gamma$, it will be necessary to observe and to measure the other components, the IB, the SD- and the INT$^\pm$.

Recently the KLOE collaboration, using the DAΦNE accelerator in Frascati, has published a new measurement of the differential decay rate of the $K^+ \to e^+\nu_e\gamma$ SD+ togheter with a measurement of the form factors [28]. The measurement is based on the observation of 1484 $K^+ \to e^+\nu_e\gamma$ SD+ events with $E^*_{gamma} > 10\ MeV$ and $E^*_e > 200\ MeV$. Figure 1.6 show the measured differential decay rate compared with different theoretical predictions. The comparison of the measured spectrum with the ChPT prediction suggests the presence of a form factor dependent by the transferred momentum as predicted by ChPT at $O(p^6)$ and suggest the failure of the LFQM to give a good description of the $K^+ \to e^+\nu_e\gamma$ process. Concerning the

Branching Ratio, they define the ratio $R_\gamma = \Gamma(K \to e\nu_e\gamma)/\Gamma(K \to \mu\nu_\mu)$ and quote the value:

$$R_\gamma = (1.483 \pm 0.066_{stat} \pm 0.013_{sys}) \cdot 10^{-5}$$

in a kinematical region with $E^*_\gamma > 10\ MeV$ and $E^*_e > 200\ MeV$, and with a $K^+ \to e^+\nu_e\gamma$ IB contribution of 1.32(1)%. In the analysis they didn't distinguish between the SD+ and SD- $K^+ \to e^+\nu_e\gamma$ components. Using a $K^+ \to e^+\nu_e\gamma$ MC based on the ChPT at $O(p^4)$ to evaluate the amount of $K^+ \to e^+\nu_e\gamma$ SD+ with $E^*_\gamma > 10\ MeV$ and $E^*_e > 200\ MeV$ the correction coefficient is:

$$corr_{op4} = \frac{N(K^+ \to e^+\nu_e\gamma SD+, E^*_\gamma > 10\ MeV, E^*_e > 200\ MeV)}{N(K^+ \to e^+\nu_e\gamma SD+, all)} = 0.65.$$

Using a $K^+ \to e^+\nu_e\gamma$ MC based on the ChPT at $O(p^6)$ to evaluate the amount of $K^+ \to e^+\nu_e\gamma$ SD+ with $E^*_\gamma > 10\ MeV$ and $E^*_e > 200\ MeV$ the the correction coefficient is:

$$corr_{op6} = \frac{N(K^+ \to e^+\nu_e\gamma SD+; E^*_\gamma > 10\ MeV, E^*_e > 200\ MeV)}{N(K^+ \to e^+\nu_e\gamma SD+; all)} = 0.66.$$

Multiplying the result by the $K \to \mu\nu_\mu$ Branching Ratio, $(63.55 \pm 0.11)\%$ [14], and dividing by the correction coefficient, the result of the $K^+ \to e^+\nu_e\gamma$ SD+ Branching Ratio assuming the ChPT at $O(p4)$ model is:

$$BR(K^+ \to e^+\nu_e\gamma SD+) = (1.430 \pm 0.065_{stat} \pm 0.013_{sys}) \cdot 10^{-5}$$

and assuming the ChPT at $O(p^6)$ is:

$$BR(K^+ \to e^+\nu_e\gamma SD+) = (1.409 \pm 0.064_{stat} \pm 0.013_{sys}) \cdot 10^{-5}$$

The form factors parameters have been obtained by fitting the measured E^*_γ distribution with the theoretical differential decay width, with the vector form factor expanded at the first order of x: $F_V = V_0(1 + \lambda(1 - x))$. The axial form factor F_A, is assumed to be independent on p^2 as predicted by ChPT at $O(p^6)$. The results of the fit, shown in figure 1.6 bottom, are:

$$V_0 + F_A = 0.125 \pm 0.007_{stat} \pm 0.001_{syst},$$

$$\lambda = 0.38 \pm 0.20_{stat} \pm 0.02_{syst}.$$

These results confirm at $\sim 2\sigma$ the presence of a slope in the vector form factor F_V.

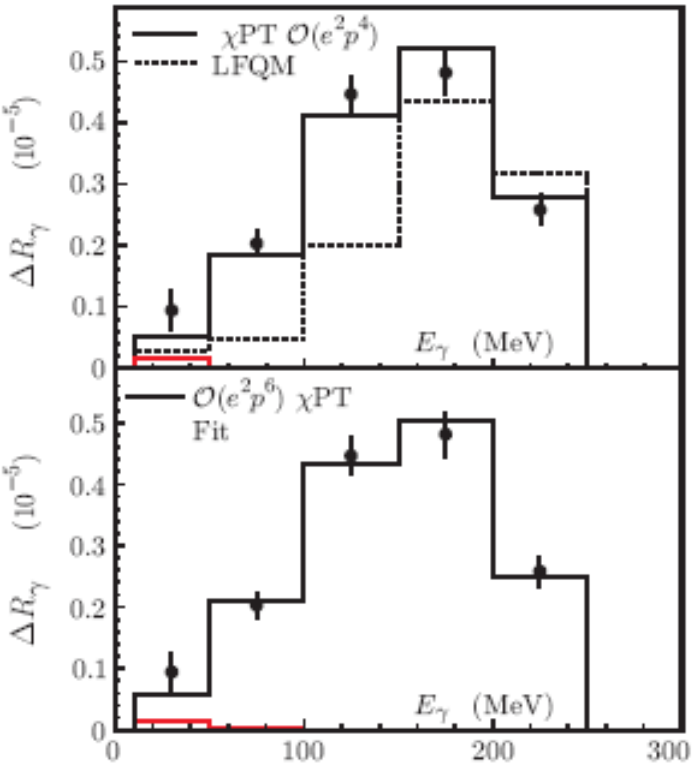

Figure 1.6: $\Delta R_\gamma = [1/\Gamma(K_{\mu 2})] \times [d\Gamma(K \to e\nu_e\gamma)/dE^*_\gamma]$ vs E^*_γ. On top Data (black dots) are compared to ChPT prediction at $O(p^4)$ and to the LFQM. At the bottom Data are fitted to ChPT at $O(p^6)$. The IB contribution is shown (red line).

Chapter 2

The NA62 experiment, phase I

The NA62 collaboration used the existing NA48/2 apparatus used by the NA48, NA48/1 and NA48/2 collaboration [29], located at the CERN-SPS north area (Fig. 2.1). A schematic view of the detector is given in figure 2.3.

The main goal of the NA48 experiment were the search of direct CP violation in the neutral kaon system through the measurement of

$$Re(\epsilon'/\epsilon) = 1 - \frac{\Gamma(K_L \to \pi^0\pi^0)\Gamma(K_S \to \pi^+\pi^-)}{\Gamma(K_S \to \pi^0\pi^0)\Gamma(K_L \to \pi^+\pi^-)}$$

with an accuracy of $2 \cdot 10^{-4}$ [30].

The NA48/1 experiment studied rare K_S decay and hyperon physics.

The main goals of the NA48/2 experiment were: a high statistics study of the charge asymmetry in $K^\pm \to 3\pi$ decays in order to improve information on direct CP violation, and perform Chiral Perturbation Theory tests with $K^\pm \to \pi^\pm\gamma\gamma$, $K^\pm \to \pi^\pm\pi^0\gamma$ and $K^\pm \to e^+\pi\pi\nu_e$ rare decays [31].

The main goal of NA62 phase I is a test of V-A theory and the $e-\mu$ universality through the measurement of the ratio of the leptonic kaon decays K_{l2}, $R_K = \frac{\Gamma(K\to e\nu)}{\Gamma(K\to\mu\nu)}$. Due to the high accuracy of the theoretical prediction [32], the measurement of R_K is a good test for the SM and is useful to set stringent constraints to "New Physics" models as, for example, the Minimal Supersymmetric Standard Model (MSSM) [33].

The main goal of NA62 phase 2 is the measurement of the ultra-rare kaon decay $K^+ \to \pi^+\nu\bar{\nu}$ Branching Ratio [34, 35]. The collaboration aims to collect $O(100)$ events during two years of Data taking in order to improve the present experimental knowledge of this process, based on 7 events [36] which doesn't have statistical power to distinguish between the SM theoretical prediction and models beyond it.

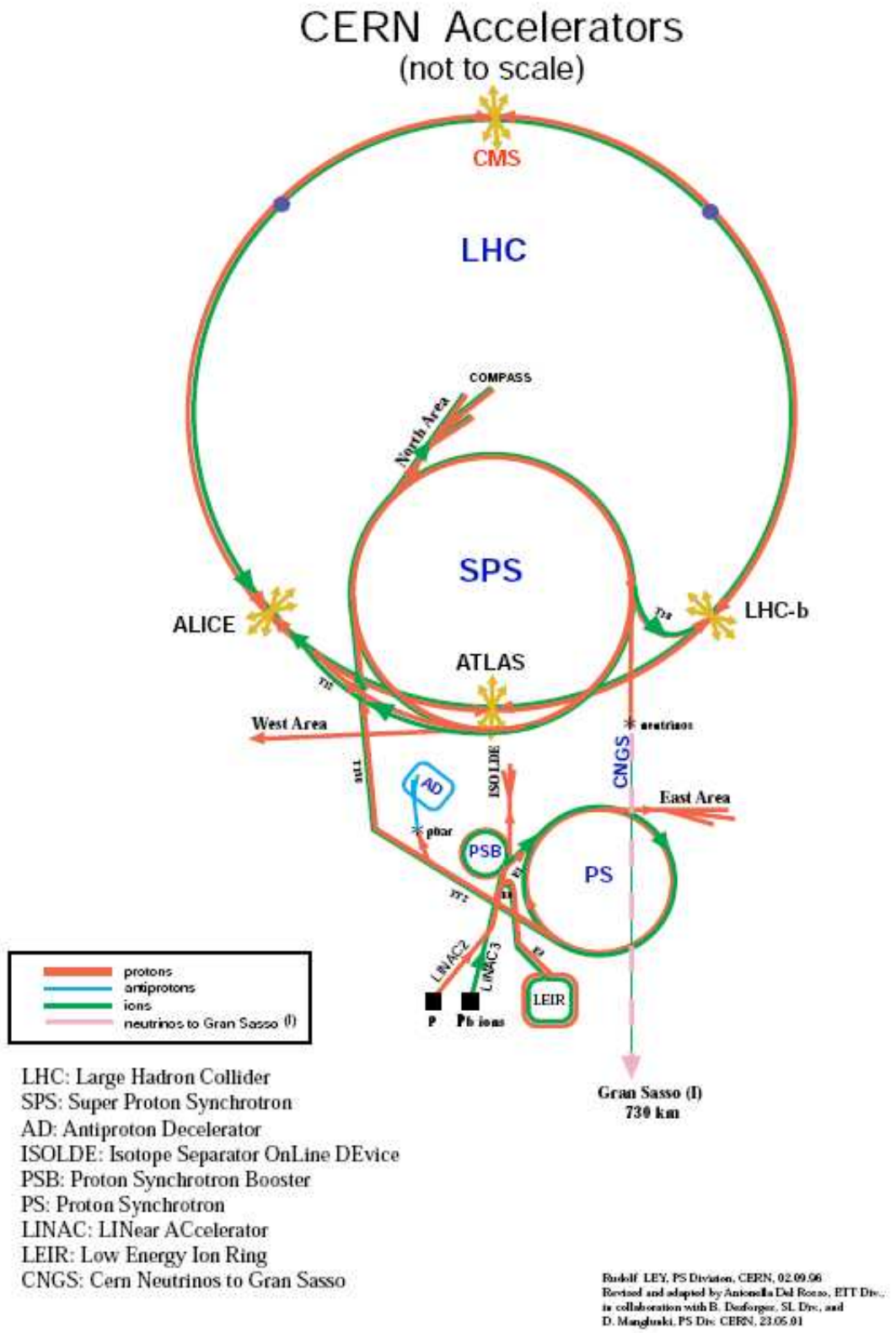

Figure 2.1: CERN accelerator complex. The NA48/2 detector is located in the SPS north area.

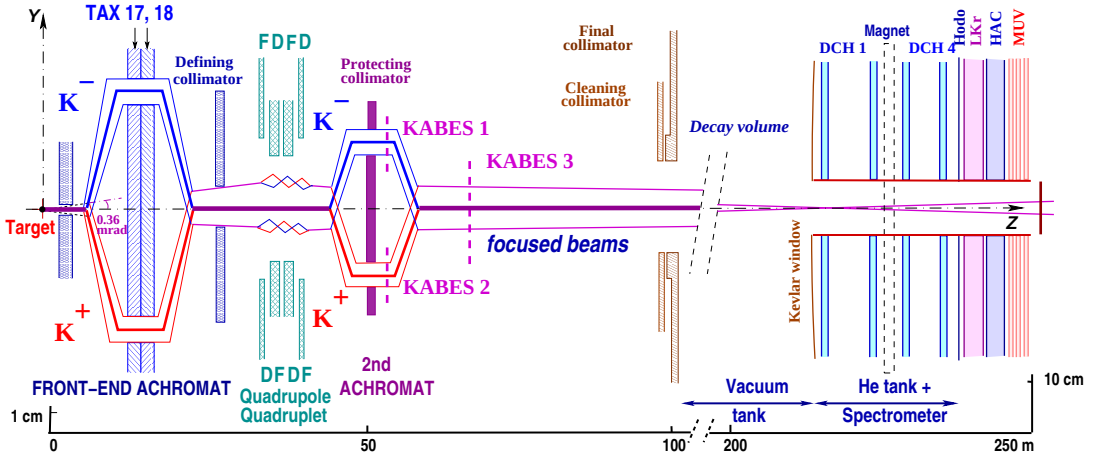

Figure 2.2: Schematic view of the NA48/2 beam line (vertical plane).

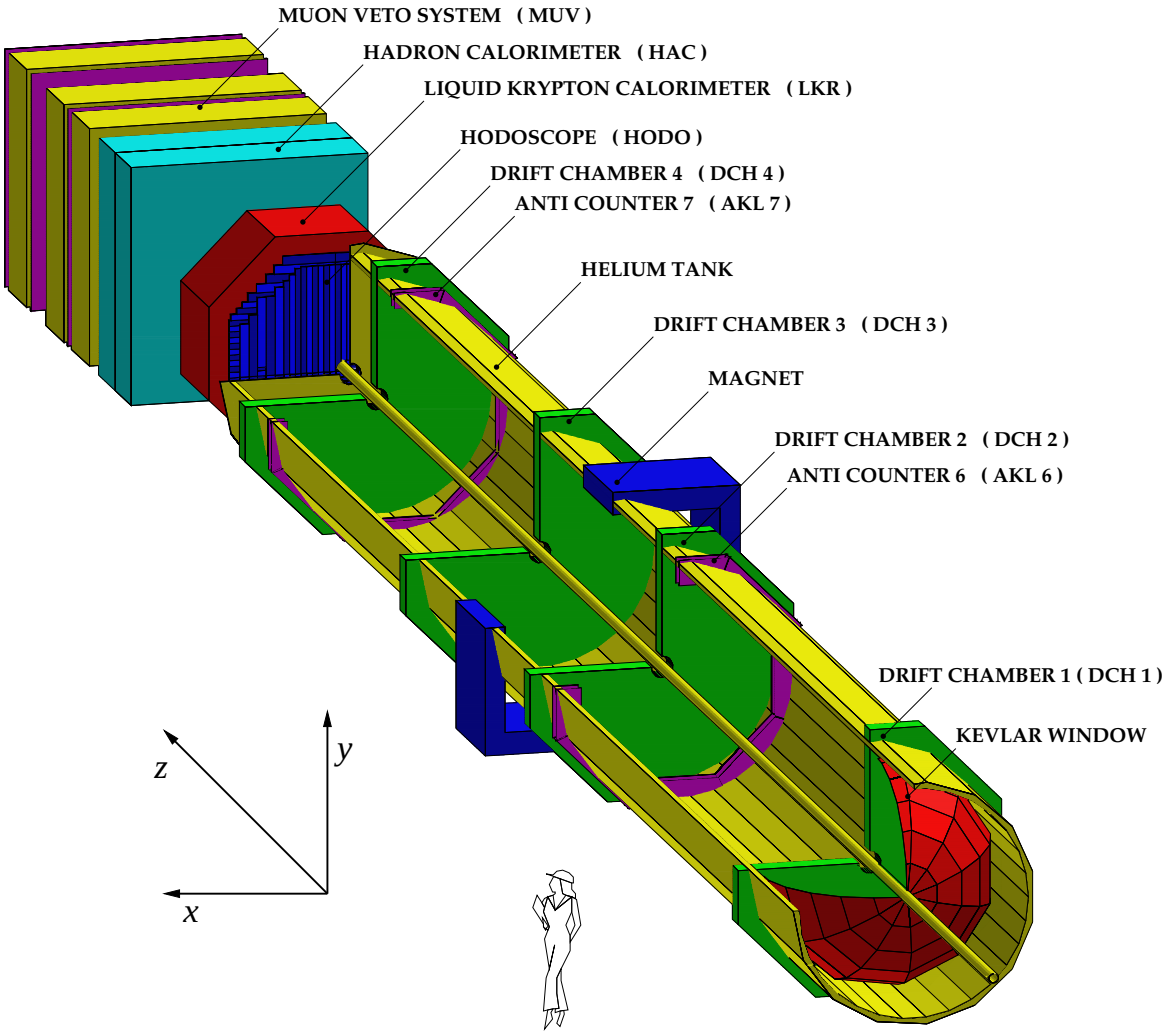

Figure 2.3: Schematic view of the NA48/2 detector.

2.1 Coordinate System

The coordinate system of the experiment is cartesian: the z axis coincides with the axis of the beam pipe and points towards the end of the detector; the y axis goes vertically from bottom to top; the x axis is horizontal and placed in such a way to define a right-handed system.

The position of all sub-detectors is given assuming the origin corresponds to the $K^{\pm}$ production target, while, at analysis level, the reference point of the system is placed ~ 120 m downstream the NA48/2 target and ~ 19 m from the last collimator.

2.2 Beam line

The kaon beam line can provide high intensity charged kaons of both polarities (Fig. 2.2). Kaons are produced by 400 GeV/c momentum protons impinging on a Be target. A system of dipole magnets selects a non separated kaon beam with momentum of 75 ± 2 GeV/c. Pions contribution in the beam is about 9 times greater than kaons. The kaon momentum is not measured directly event by event, but the average value is obtained using reconstructed $K^+ \to \pi^+\pi^+\pi^-$ decays. The measured momentum spread is $\Delta P_K^{RMS}/P_K = 2\%$.

2.3 Decay Volume

The total decay volume length is ~ 114 m. The cylindrical vacuum tank containing the two beams (*Blue Tube*) has an inner diameter of 1.92 m, increased up to 2.4 m in the last 48 m of the decay region. The volume is evacuated to a pressure $< 10^{-4}$ mbar to avoid interactions of kaon decay products before their detection and also to minimize interaction of the not decayed particle of the beam. The tank is closed at the end by a 0.8 mm ($\sim 3 \cdot 10^{-3} X_0$) thick convex hemispherical shaped, 1.3 m radius, Kevlar window to separate the vacuum from the following volume, filled with helium gas at atmospheric pressure, which contains the drift chambers of the magnetic spectrometer.

A small residual magnetic field, mostly due to the Earth field, is present in the decay region: it has been carefully measured and mapped using Hall probes before the 2003 Data taking to allow a posteriori correction on reconstructed tracks and to include its effect in Monte-Carlo simulation.
Downstream the Kevlar window, the beam containing mainly undecayed kaons and pions, travels in vacuum in a carbon fiber pipe of 0.152 m diameter and 1.2 mm

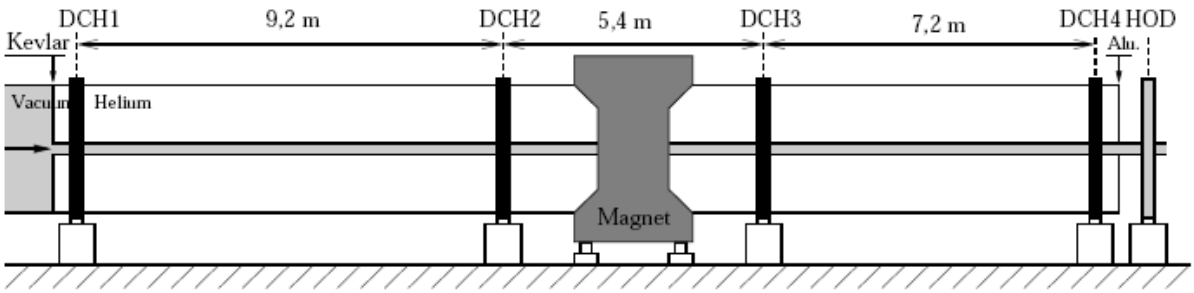

Figure 2.4: Lateral view of the magnetic spectrometer.

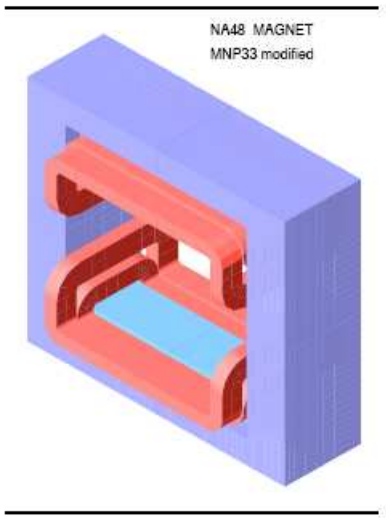

Figure 2.5: Spectrometer dipole magnet.

thick.

2.4 Magnetic Spectrometer

The magnetic spectrometer is composed of four drift chambers (DCH) and one dipole magnet placed between the second and the third chamber (Fig. 2.4). The central aperture between the magnet poles is 2.45×2.40 m^2 to match the electromagnetic calorimeter acceptance. Two pairs of coils (Fig. 2.5) give a vertical field of 0.37 T at the centre of the magnet. The field integral along the axis between the second and third drift chamber corresponds to a 263 MeV/c transverse momentum kick.

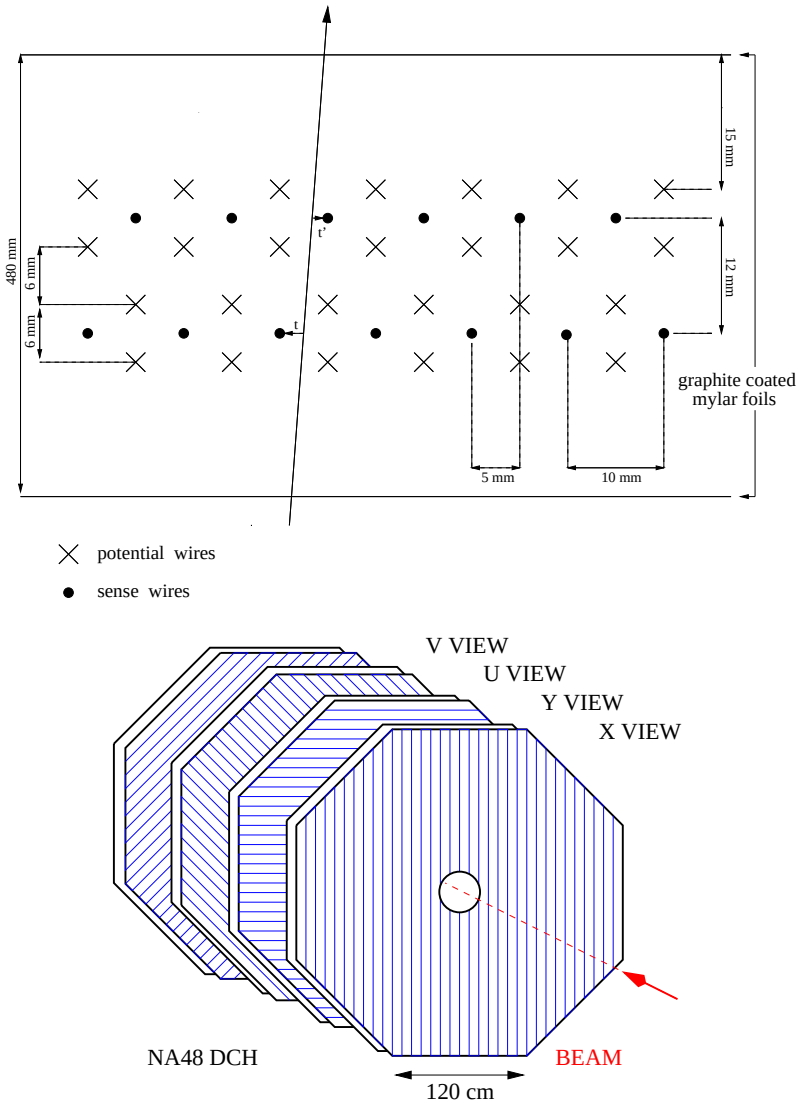

Figure 2.6: Drift cell geometry (Top) and *DCH* views orientation (Bottom).

The spectrometer is housed in a stainless steel cylindrical vessel, $\sim$ 23 m long and 2.8 m internal diameter, kept at atmospheric pressure. The volume is filled with pure helium to reduce multiple Coulomb scattering and the probability of particle interactions with the medium. The four drift chambers have an octagonal shape with a transverse width of 2.9 m. Each chamber contains eight planes of grounded sense wires (Fig. 2.6(Top)), oriented in four different directions, orthogonal to the beam axis: 0° (X, X'), 90° (Y, Y'), $-45°$ (U, U') and 45° (V, V') (Fig. 2.6(Bottom)). Each so called "view" contains two planes staggered by half wire pitch to resolve the left-right ambiguities and to increase the spatial resolution of the reconstructed point. The total number of wires per plane is 256 and the maximum drift time is 100 ns, corresponding to the half wire pitch of 5 mm, obtained operating with a Ar 50% + C_2H_6 50% gas mixture. The resolution of the spatial position of the

reconstructed hit is better than 100 μm and the resulting momentum resolution of the magnetic spectrometer is:

$$\frac{\sigma(P)}{P} = 0.47\% \oplus 0.020 \cdot P(GeV)\%.$$

The first term is related to the multiple scattering in the helium tank and drift chambers, while the second one to the spatial point resolution of the chambers. The resolution of track time measurement is ~ 0.7 ns.

2.4.1 Track Reconstruction

The off-line track reconstruction is divided in two steps in order to achieve an efficient determination of the number of charged particles crossing the detector, their direction, momentum and crossing time:

1. the first step considers only the detected hits in the four chambers of the spectrometer:

   - space points are reconstructed using the firing wires positions;
   - space points on the first and second chambers are connected to form mini-tracks;
   - a complete track is formed if the y projection of the mini-track extrapolation to the fourth chamber is close to a space point to better then 4 cm;
   - at the level of the first step of the track reconstruction the drift time information is not used in order to reduce the combinatory of the space points.

2. in the second step the drift time measurements are considered:

   - the drift time is used to improve the space resolution of the impact points;
   - a quality variable is associated to each track, taking into account the hit position on each view, and it is used to reject bad tracks;
   - momentum and track charge are then calculated exploiting an accurate map of the magnetic field.

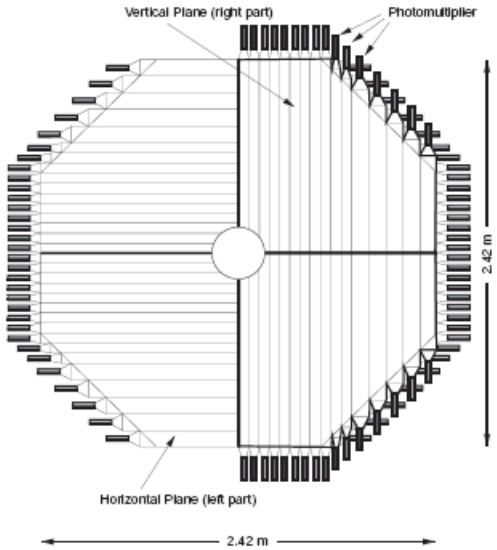

Figure 2.7: Charged hodoscope horizontal and vertical planes.

2.5 Charged hodoscope

The charged hodoscope (*CHOD*) consists of two planes of plastic scintillator segmented into horizontal and vertical strips and arranged in four quadrants (Fig. 2.7). The thickness of a single counter is 2 cm ($\sim 0.5X_0$) and the width for counters is 6.5 cm close to the beam pipe and 9.9 cm for the other ones. The length varies from 0.6 m up to 1.21 m. The radius of the central hole, where the beam pipe is inserted, is 10.8 cm.

The distance between the two planes (0.74 m) and the distance of the second plane from the calorimeter (0.8 m) have been chosen in order to reduce the effect of back splash particles from the *LKr* front end.

The detector is divided into four quadrants to produce topological and multiplicity triggers: a single track event will generate a signal (*Q1*) due to time coincidence of the hits in the correspondent quadrant of the two planes.

After off-line corrections the single track *CHOD* time resolution is:

$$\sigma_t \sim 250ps$$

2.6 Electromagnetic calorimeter

Liquid krypton has been adopted, in a quasi-homogeneous configuration, allowing for the full development of electromagnetic showers ($> 99\%$ containment for 50 GeV) within an octagonal shaped cylindrical volume of 1.25 m inscribed circle diameter

and 1.27 m depth ($\sim 27X_0$) (Fig. 2.8 (left)).

Thin *Cu-Be* ribbons (Fig. 2.8 (right)) have been chosen to construct the electrodes in the form of longitudinal towers of about 2×2 cm^2 cross-section. The active volume is divided into 13248 ($2\times2\times127$) cm^3 double ionization cells with the central ribbon as anode. The transverse dimensions of the cells increase as a function of the distance from the front of the calorimeter up to a maximum of 1.1% at the back. They define a projective geometry of the calorimeter (LKr) pointing at about 110 m upstream it, realized in order to achieve the best possible accuracy in the measurement of the angle between the flight path of photons and the beam direction. To ensure a good uniformity of the response over the whole surface of the calorimeter, the distance between electrodes must be known with high accuracy. For this reason the electrode ribbons are held by five spacer plates that fix their transverse position at five longitudinal positions in addition to the front and back planes. The tension of the ribbon is $\sim 2N$. The feed through the spacing plates gives to the electrodes a peculiar zig-zag shape ("Accordion geometry") that minimizes inefficiencies coming from showers developing inside the anode (Fig. 2.9). The physical properties of the Kr are reported in table 2.1. To precisely control the temperature, the calorimeter

Atomic number	36
Mass number	84
Density at 120 K	2.41 g/cm^3
Radiation length	4.7 cm
Nuclear interaction length	60 cm
Moliere radius	6.1 cm
Boiling point at 1 bar	199.8 K
Critical energy	21.51 MeV
Radioactivity	500 Bq/cm^3
Electron drift velocity at 5 kV/cm	0.37 cm/μs

Table 2.1: Liquid krypton physical properties

has been enclosed in a cryostat, made of an outer aluminium vessel and an inner stainless steel container vacuum insulated: the system keeps the temperature of the LKr calorimeter at 121 K within $\pm0.1K$. The whole cryostat introduces some passive material ($\sim 0.65X_0$) in front of the LKr that corresponds to a 50 MeV loss in reconstructed photon energy.

Only about 60 out of the 13248 LKr cells, knows as "dead cells", have electronic faults (faulty preamplifiers, bad pedestal and/or a very unstable response to calibration pulses) preventing their correct utilization. The position of this cells is visible in figure 2.10 where the illumination of the calorimeter is reported.

After calibration and corrections, the energy resolution (Fig. 2.11) of the LKr

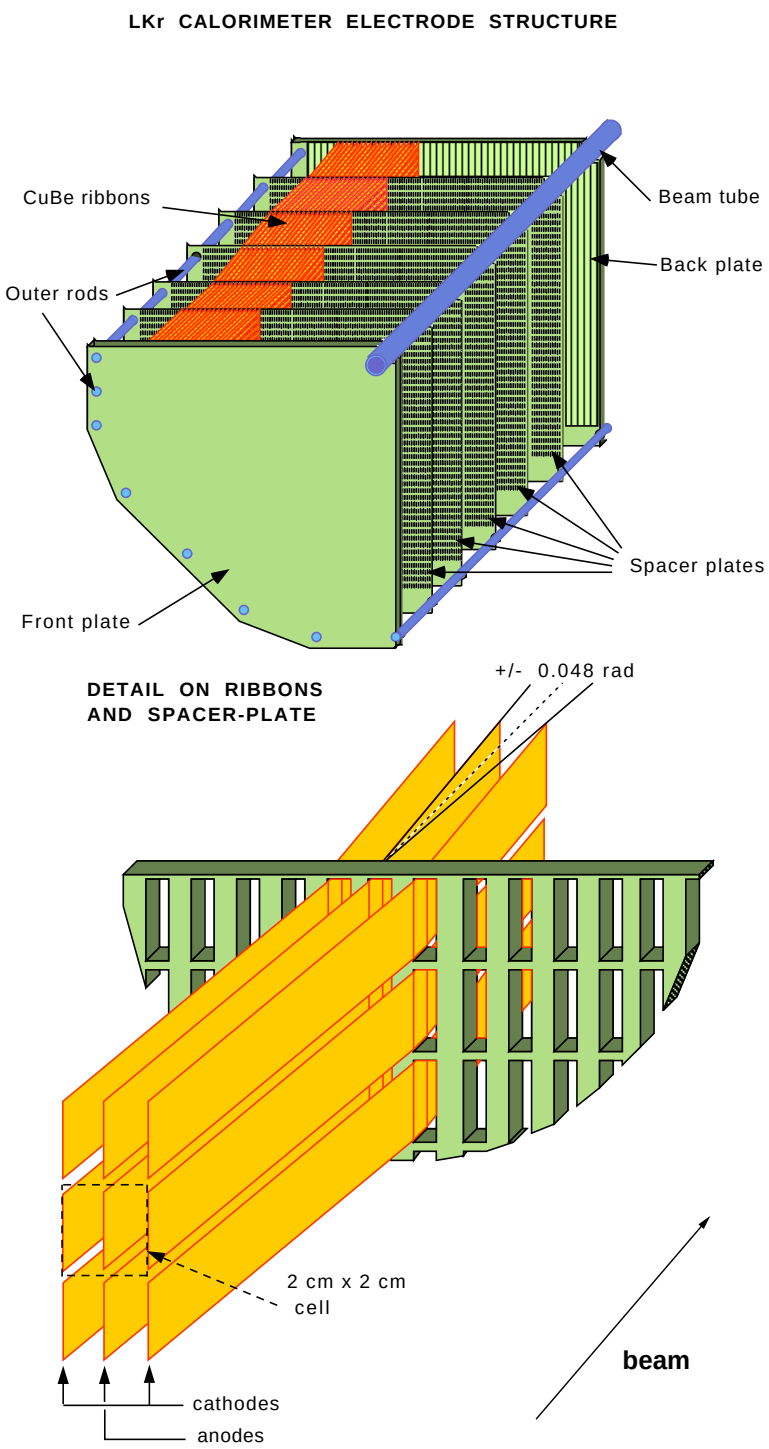

Figure 2.8: *LKr* electrode (left) and cell (right) structure.

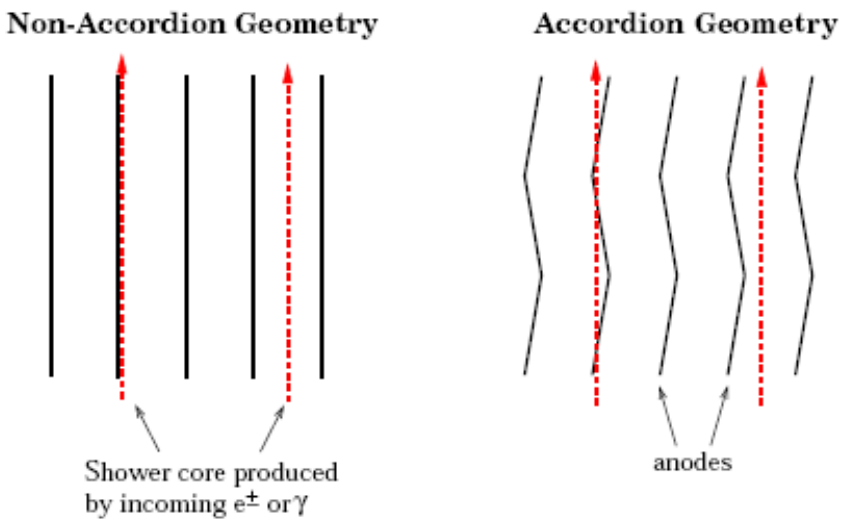

Figure 2.9: "Accordion" geometry for the calorimeter electrodes.

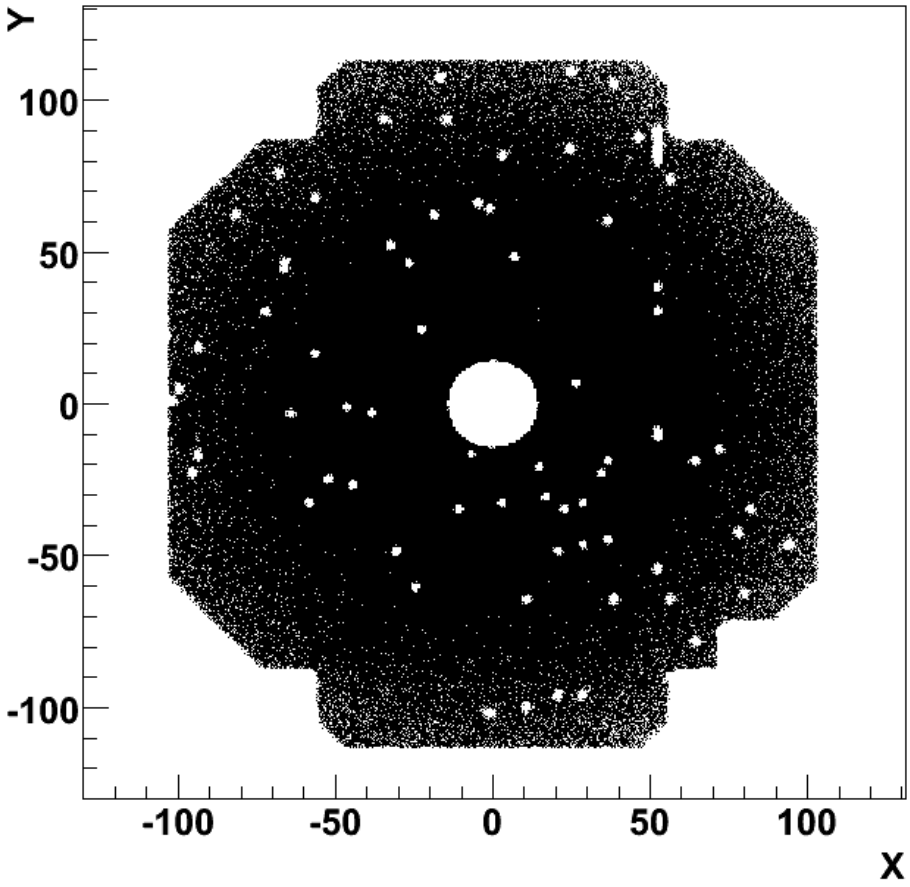

Figure 2.10: Position of the "dead cells" in the calorimeter.

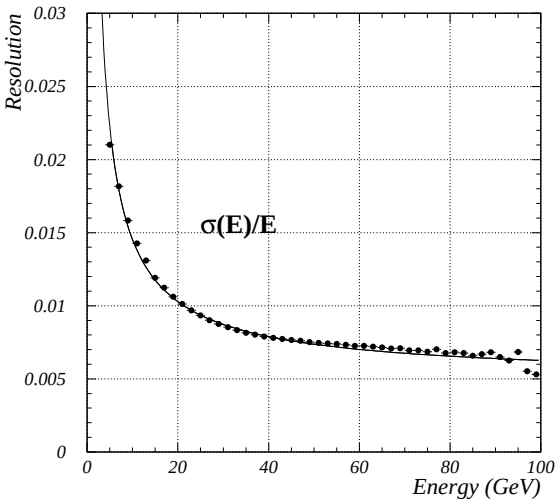

Figure 2.11: *LKr* energy resolution as a function of the energy.

calorimeter can be parametrized as:

$$\frac{\sigma(E)}{E} = \frac{3.2\%}{\sqrt{E_{GeV}}} \oplus \frac{10\%}{E_{GeV}} \oplus 0.5\%$$

The first term depends on stochastic sampling fluctuations, the second one on electronic noise and Kr natural radioactivity and the last one on inhomogeneities, material in front of the calorimeter and the non perfect intercalibration of the cells.

Good spatial and time resolutions are also achieved:

$$\sigma_{x,y} = (\frac{4.2\%}{\sqrt{E_{GeV}}} \oplus 0.5\%) \text{ cm}$$

$$\sigma_t = (\frac{2.5}{\sqrt{E_{GeV}}}) \text{ ns}$$

2.6.1 Cluster Reconstruction

A pattern recognition technique allows to determine which cells belong to the same shower, the energy deposition, crossing time, position and shower transverse size. A cluster is defined if one cell ("seed") has an energy larger than 100 MeV after pedestal subtraction, if it has more energy than any of the eight surrounding cells and if its energy satisfies the following condition:

$$E_{seed} > 0.18GeV + 1.8 \cdot E_{average}$$

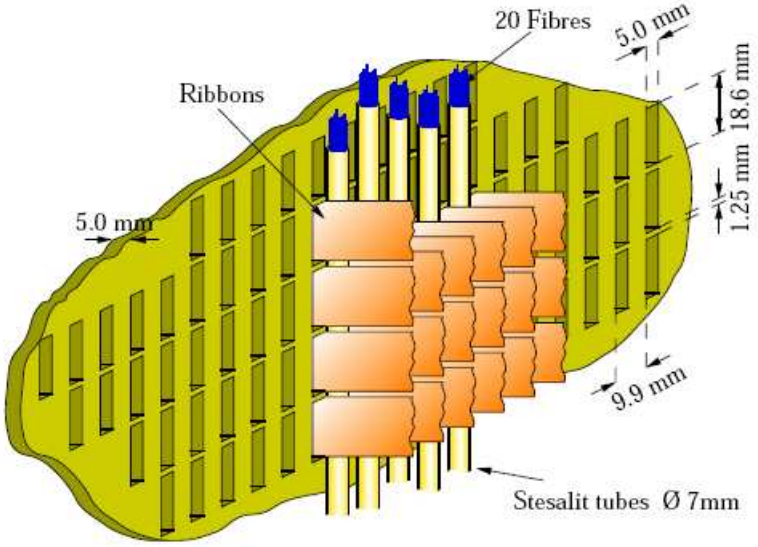

Figure 2.12: Sketch of the neutral hodoscope fibers.

where E_{seed} and $E_{average}$ (the average energy deposition of the eight surrounding cells) are in GeV.

The following steps are applied to extract the physical parameters of the shower:

- The cluster energy is evaluated performing a loop over the clusters, including in each cluster from a minimum of 69 to a maximum of 121 cells (22×22 cm^2 squared box) centered on the seed position; if a cell belongs to more than one cluster, then its energy content is shared among the clusters according to their profile distribution; the energy of the cluster is corrected for energy loss due to proximity to the hole of the beam pipe and calorimeter borders, dead cells and energy scale of the calorimeter.

- The cluster position is estimated using the centre of gravity of the energy deposition in 3×3 cells box around the seed position.

- The cluster development size is calculated independently in both x and y directions as the R.M.S of the energy distribution in a 5×5 cells box around the seed position.

- The cluster time is defined as the average of the event time recorded by the cells in the 5×5 cells box around the seed one.

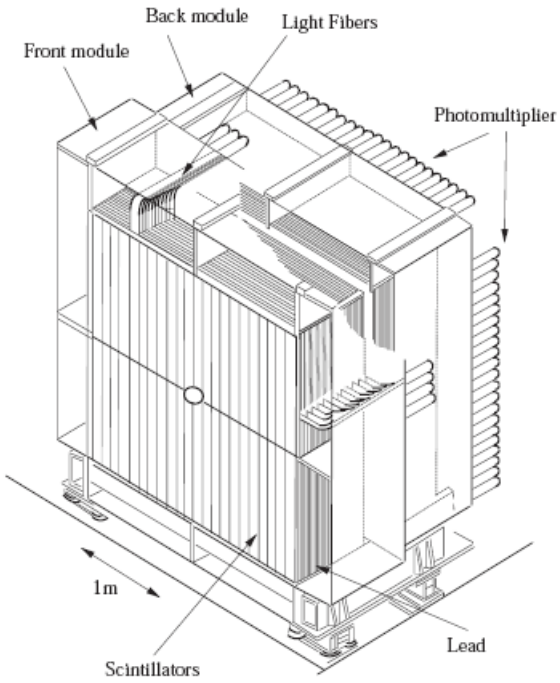

Figure 2.13: Hadron calorimeter layout.

2.7 Neutral hodoscope

In the inner part of the electromagnetic calorimeter, at the depth of $\sim 9.5X_0$, a scintillating fiber hodoscope is placed. The *NHOD* is made of 256 vertical bundles of scintillating fibers (Fig. 2.12) contained in an epoxy-fiberglass tube (7 mm in diameter and 2 m in length) and immersed directly in the liquid krypton. The neutral hodoscope provides an independent measurement of the time of the shower and acts as an independent source of minimum bias trigger (T0N) to check the efficiency of the neutral trigger systems.
The *NHOD* was developped to be fully efficient for cluster with energy ∼25 GeV and its efficiency fall down for energy below 10 GeV.

For showers of energy greater than 15 GeV the typical time resolution is:

$$\sigma_t = 250 \text{ ps}$$

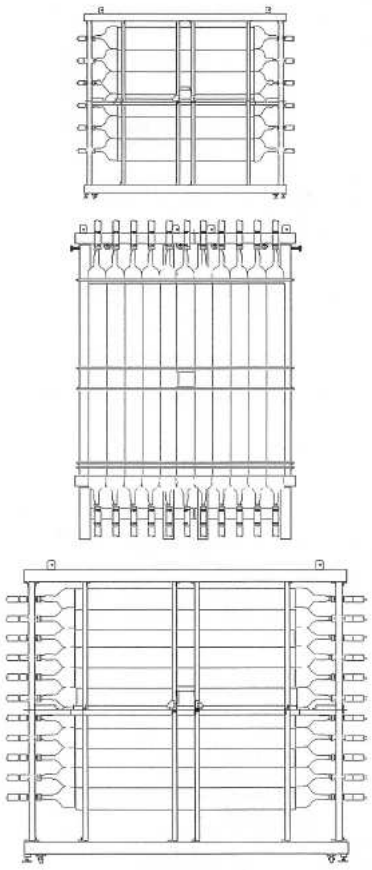

Figure 2.14: Geometry of the muon veto panes.

2.8 Hadron calorimeter

The hadron calorimeter (HAC) consists of an iron-scintillator sandwich of 1.2 m total thickness ($\sim 6.7\ \lambda_{Int}$). It is longitudinally divided into two separate modules (front and back), each consisting of 24 iron plates, 25 mm thick, of dimension 2.7×2.7 m^2, alternated with 24 scintillator planes, 4.5 mm thick, each of them divided into 44 half-strips per plane arranged in vertical and horizontal direction (Fig. 2.13).

The HAC energy resolution is:

$$\frac{\sigma_E}{E} = \frac{0.65}{\sqrt{(E)}}$$

where E is in GeV.

2.9 Muon veto counter

The complete muon veto counter array (MUV) consists of slightly overlapping long flat strips of plastic scintillator arranged in three planes, alternatively in vertical and horizontal direction, each one preceded by a 0.8 m ($\sim 5\ \lambda_{Int}$) thick iron wall to provide absorption of hadrons (Fig. 2.14). The array occupied a longitudinal space of 4.3 m including additional 0.4 m wall behind the third plane to absorb backward-going products of interactions at the rear of the beam line.

The reconstruction efficiency for single-muon events is $> 99\%$.

2.10 Trigger system

The NA62 trigger is a multilevel system, designated to have in principle no dead time and to be able to cope with rates of particles in the detectors at the level of 1 MHz.
The full acquisition system is pipelined, synchronized by a 40 MHz clock. Every 25 ns the detectors write their output to a circular memory 204.8 μs deep.

The system (Fig. 2.15) is divided in two parts: the Charged and the Neutral Trigger. The two sub-systems are controlled by the *Trigger Supervisor (TS)* that collects all the information and takes the final decision to read-out or discard the event.

2.10.1 Charged trigger

The Charged Trigger system consists of two levels: the Pre-Trigger ($L1C$) and the $L1C$ Trigger Supervisor ($L1TS$).

The Pre-Trigger is a fast hardware system that collects information from drift chamber, charged and neutral hodoscope and synchronizes signals before sending them to the next level; below, how the various detector produce the trigger signals is reported:

- the *CHOD* provides a simple information on the topology of event; sub-coincidences between the horizontal and the vertical plane are used to identify different topological classes of events. The definition of the sub-coincidences comes from a time and space coincidence between the hits in a group of horizontal scintillators and the hits in a group of vertical scintillators. The groups are composed of 7 scintillators near the beam pipe or from the remaining 9 scintillators of the quadrant far from it. Hence for each quadrant we have 4

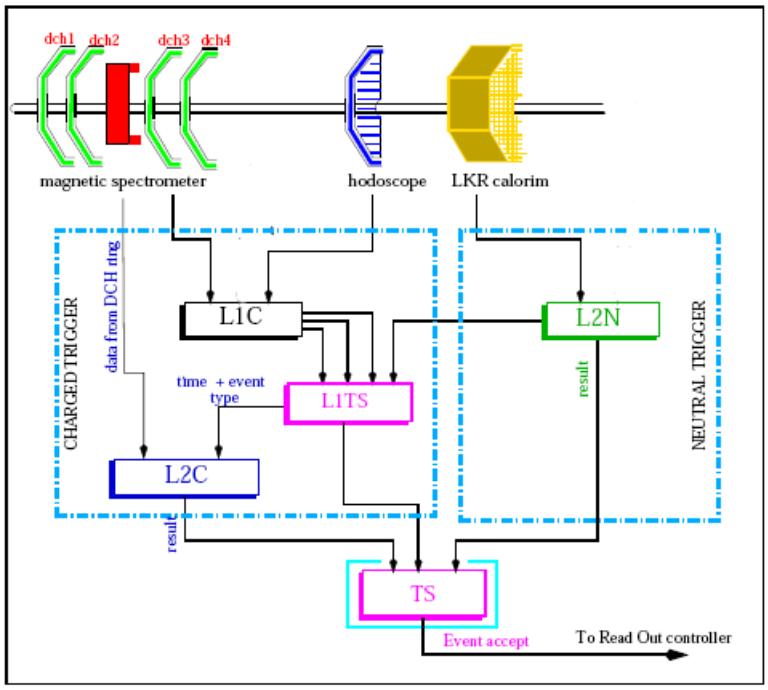

Figure 2.15: Schematic view of the NA62 trigger.

sub-coincidences for a total number of 16 sub-coincidences. After that definition the following signals are possible:
Q_1: a single coincidence; it tags decay with at least a charged particle in the acceptance; it is quite noisy and fires easily on accidentals;
Q_2: two coincidences; it tags decays that have at least two charged particles; the signal is purer than Q_1, but the efficiency is lower.

- the *NHOD* triggers on a shower in the *LKr*; the signals sent to the Pre-Trigger system provide a time measurement of the neutral events, independent of that obtained from the calorimeter:
  T0N signal is a loose coincidence between opposite halves of the Neutral Hodoscope, the signal is useful as minimum bias trigger for efficiency studies;

- the *DCHs* provides informations on the number of hits in the 4 views of the 4 chambers, this informations are combined to produce triggers to select events with a different number of charged particles; one example of drift chambers trigger is explains in section 2.10.4.

The *L1C* Trigger Supervisor combines the Pre-Trigger signals with calorimeter energy information coming from the Neutral Trigger; some loose selection based on topology and energy of the events is made; before going to the *L1TS*, some signals

can enter a prescale module to downscale of a given factor, the number of triggers per burst.

2.10.2 Neutral trigger

The Neutral Trigger is implemented in a 40 MHz dead-time free pipeline. The total latency of the pipeline is 128 clock cycles, 3.2 μs. Every 25 ns, the trigger reconstructs on-line a set of physical quantities, like total energy, center of gravity, kaon vertex position and number of *LKr* peaks in both horizontal and vertical projections. With these reconstructed quantities, it performs a selection and sends the information to the Trigger Supervisor and partially to the Charged Trigger chain. The following are some examples of signal produced by the Neutral Trigger:

- *NT-PEAK*: more than two *LKr* cluster peaks in at least one projection (x or y);
- *NT-NOPEAK*: an energy deposition in the *LKr* calorimeter greater than 30 GeV with a center of gravity smaller than 25 cm and a kaon decay position smaller than 90 m;
- *LKrMBias*: a minimum deposited energy in the electromagnetic calorimeter greater than 10 GeV.

2.10.3 Trigger supervisor

The Charged and Neutral Trigger results are sent to the Trigger Supervisor (TS) [37], a fully pipelined 40 MHz digital system which correlates the information coming from different trigger sources and takes the final decision on the selection of the event. It also provides a final trigger word and time-stamp and sends to the Read Out Controllers (*ROC*) the command to record the event information before the end of the 200 μs Data persistence time.

All the trigger signal arrived to the TS, coming from the Charged and Neutral Trigger, are sent to external acquisition units, called Pattern Units, for monitoring purposes and for the trigger efficiency studies.

2.10.4 $K^+ \to e^+\nu_e\gamma$ trigger logic

$K^+ \to e^+\nu_e\gamma$ events are characterized by one charged track reconstructed by the magnetic spectrometer and two clusters in the electromagnetic calorimeter. The

trigger should be able to select events with one charged track and with a certain amount of energy in the *LKr*.

As a consequence of the characteristics of the signal, the $K^+ \to e^+\nu_e\gamma$ are selected using both Charged and Neutral triggers information. The trigger signal is the following:

$$Q_1 \times LKrMBias \times 1TRKLM$$

where $1TRKLM$ is a signal based on the number of hits in the drift chambers considering a set of coincidence and OR to produce the following conditions:

$$\begin{aligned} &\Big((N_{hits}(1,1) < 15) + (N_{hits}(3,1) < 15) + (N_{hits}(4,1) < 15)\Big) \times \\ &\Big((N_{hits}(1,2) < 15) + (N_{hits}(3,2) < 15) + (N_{hits}(4,2) < 15)\Big) \times \\ &\Big((N_{hits}(1,4) < 15) + (N_{hits}(3,4) < 15) + (N_{hits}(4,4) < 15)\Big) \end{aligned} \tag{2.1}$$

where $N_{hits}(i,j)$ is the number of hits in the view i of drift chamber j.

The $Q1$ components ensures the presence of at least one charged track, the $LKrMBias$ ensures a certain amount of energy in the calorimeter, and the $1TRKLM$ ensure a low multiplicity in the spectrometer (1 track).

2.11 Data acquisition and format

The NA62 data acquisition system (Fig. 2.16) is composed by 11 Sub-Sector PCs, 8 Event Builders PCs and one Control PC. All PCs are connected to a Fast Ethernet Switch operating at 100 Mbit/s. Any given Sub-Detector PC stores the Data recorded by the connected detector during the SPS burst. Data are assembled, partitioned in eight blocks and sent to the Event Builder PCs in such a way that all the information on any single event are in the same block and go to same PC. The Event Builders arrange the Data in complete *RAW* events that are sent to ten disk-servers (average capacity $\sim$ 10 TB) at the CERN computing center via a Giga-Switch connection. In case of an event number mismatch from different sub-detectors, the whole burst is discarded. In normal conditions the amount of transferred Data from the experiment to the disks is around $\sim$ 3TB/day. The *RAW* Data are processed by a software program (*L3*) running on the CERN Batch System (*LSF*) that performs the event reconstruction, filters the Data and creates different output streams. The program output are in *COmPACT* [38] format containing reconstructed information and physics quantities. Both *COmPACT* and *RAW* files are recorded on tapes. The average time from data acquisition until the end of processing is $\sim$ 30 minutes: this

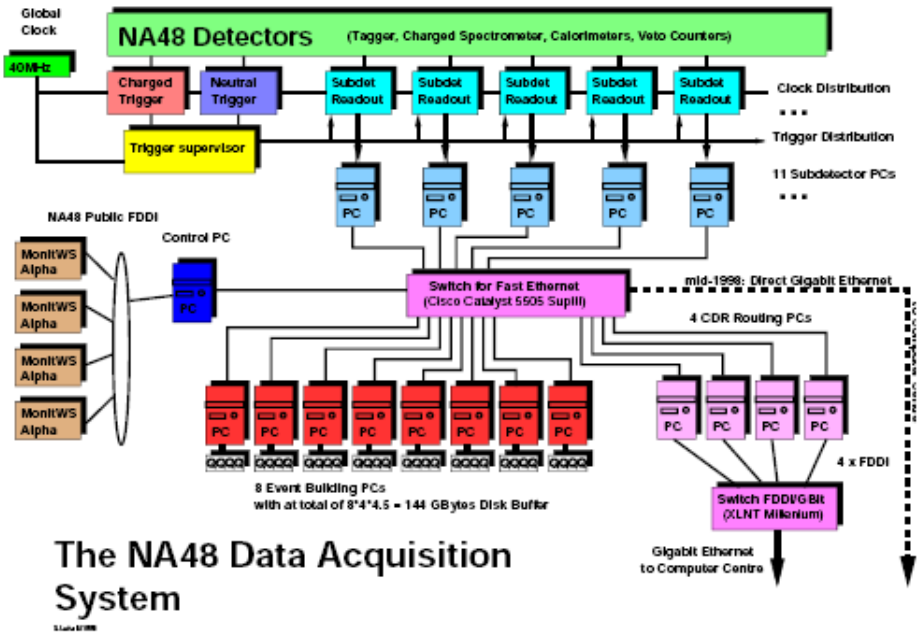

Figure 2.16: Schematic view of the NA48/2 DAQ system.

allows a quite fast feedback to check the Data quality. The overall efficiency of the offline processing is slightly greater than 99%. The typical size on one *RAW* burst is $\sim$ 500 MB while a typical *COmPACT* file is $\sim$ 120 MB. *RAW* Data are sometime reprocessed to apply the best recomputed calibration constants. During this process the *SuperCOmPACT* format is produced to reduce the total amount of Data and to speed up the analysis time.

2.11.1 The *L3* filter

During the 2007 run, when the *RAW* Data were processed, two main streams were produced according with the *L3* condition:

1. The $K^+ \to e^+\nu_e$ stream:
   - at least one track reconstructed in the magnetic spectrometer;
   - (5 $<$ charged track momentum $<$ 90) GeV/c;
   - the ratio between the energy released in the calorimeter and the charged track momentum greater than 0.6.
2. The $K^+ \to \mu^+\nu_\mu$ stream:
   - at least one track reconstructed in the magnetic spectrometer;
   - (charged track momentum $<$ 90) GeV/c;

2.12 Data taking

Data were collected during the summer 2007 for a total of $\sim$ 120 days. In order to reduce possible systematic effects due to detector left-right asymmetry, beam lines and spectrometer magnet polarities were frequently reversed. The Data taking was divided in several periods; the difference between the periods were on beam geometry, beam intensity, trigger conditions and on the presence of a lead wall between the two planes of the charged hodoscope. The lead wall has been used to stop all the charged particles except the muons in order to study the interactions of muons in the calorimeter. The wall has been present in the first part of the Data taking ($\sim$ 64 days).

During the Data taking some special runs with different beams (muon beam, beam without kaons and K_L beam) were also collected in order to study some systematic effects and background coming from the other particles of the beam as muons and pions.

2.12.1 The period 5

The period 5, for now on P5, $\sim$ 53 days long, represents $\sim$ 40% of the whole statistics. During this period the lead wall has been removed from its position and the kaon beam has been only a K^+ beam. During the P5 $\sim 2.14 \cdot 10^9$ total triggers have been collected, divided into 80551 good bursts. The main triggers used were:

$$Q_1 \times LKrMBias \times 1TRKLM$$

$$Q_1 \times 1TRKLM/150$$

where 150 is a downscaling factor.

The P5 is the period of Data taking used for the analysis described in this thesis because it is the most stable. For the entire period the beam type and trigger conditions have not been changed. On the contrary, the other periods are of short duration with different beam and trigger conditions.

Other motivation in the use of the P5 is the absence of the lead wall providing the full acceptance of the calorimeter, necessary to increase as much as possible the signal candidates available for the analysis.

Chapter 3

Monte-Carlo Simulation

The measurement of the $K^+ \to e^+\nu_e\gamma$ SD+ Branching Ratio is based of several steps:

1. the choice of the conditions and cuts to select the signal events;
2. the measurement of the signal selection acceptance;
3. the measurement of the number of kaons decayed during the Data taking period inside the fiducial decay region;
4. the residual background contamination.

In order to measure the acceptances and the residual background contamination, a detailed Monte-Carlo simulation of the signal and background decay channels is necessary.

3.1 The simulation

Monte-Carlo simulation has been used to optimize selection conditions, evaluate acceptances and analyze the composition of the physical background. The official NA48/2 software (*CMC*) [39] is based on the *GEANT3 CERNLIB* package [40] and includes:

- a full beam optics and geometry simulation;
- the simulation of the small residual magnetic field in the decay region upstream of the spectrometer;
- a detailed description of detector materials, geometry and reconstruction, including time collection of light in scintillators, single wire efficiency, electron drift time in DCHs and *LKr* dead cells position;

- the simulation of physical processes such as electron-positron annihilation, bremsstrahlung, Compton scattering, δ ray production, hadronic interactions, continuous energy loss, multiple scattering and photoelectric effect;

- secondary particle production; some examples of particular interest for the analysis, as it will be seen in the next sections, are:

  - $\mu \to e\nu\bar{\nu}$: the charged muon decay ($BR \sim 100\%$) can occur within the experimental volume affecting the track reconstruction (direction and momentum);

  - $\pi^0 \to \gamma\gamma$: the double γ decay of the π^0 ($BR = (98.823 \pm 0.034)\%$), due to its short mean free path ($c\tau = 25.1$ nm), is assumed to occur at the same position as the kaon decay;

  - $\pi^0 \to \gamma e^+ e^-$: the Dalitz decay of the π^0 ($BR = (1.174 \pm 0.035)\%$);

  - $\pi^0 \to e^+ e^- e^+ e^-$: the Double Dalitz decay of the π^0 ($BR = (3.34 \pm 0.16) \cdot 10^{-5}$).

CMC simulates only one charged kaon beam, K^+ or K^-, and only one decay mode, $K \to e\nu_e\gamma$ or $K \to e\pi^0\nu_e$ or etc.., for each sample. A number of events proportional to the kaon flux measured with $K^+ \to e^+\pi^0\nu_e$ decay, described in chapter 5, and proportional to the number of triggers collected per run, has been simulated for each decay sample. In this way, all the characteristics of the Data sample, like the ratio between samples of both sign of achromat and spectrometer magnetic fields, are reproduced in the Monte-Carlo.

Each decay is generated in the kaon rest frame, boosted to the laboratory frame and then propagated through the detector. Kaon momentum and decay position are simulated in a wider range with respect to the selected one to prevent bias from resolution effects:

- 65 GeV/c $\leq P \leq$ 85 GeV/c

- -22 m $\leq z_{decay} \leq$ 95 m

Simulated Data are recorded in the same format (*COmPACT*) of the experimental Data and then converted in *SuperCOmPACT*, allowing the use of the same analysis tools.

3.2 The $K^+ \to e^+\nu_e\gamma$ simulation

The $K^+ \to e^+\nu_e\gamma$ generator allows the simulation of all the 3 components, the IB, the $SD+$ and the $SD-$ separately. $K^+ \to e^+\nu_e\gamma$ $(SD+)$ events are been generated according to the 3 theoretical models, as described in the previous chapter with the possibility to use also the new form factors values measured by the KLOE collaboration. *CMC* allows to choose the model to use for the generation of the decay.

3.3 Background simulation

Channel	BR
$K^+ \to e^+\pi^0\nu_e$	$(5.07 \pm 0.04)\%$
$K^+ \to e^+\pi^0\nu_e\gamma$	$(2.56 \pm 0.16) \cdot 10^{-5}$
$K^+ \to e^+\pi^0\pi^0\nu_e$	$(2.2 \pm 0.4) \cdot 10^{-5}$
$K^+ \to e^+\nu_e$	$(1.55 \pm 0.07) \cdot 10^{-5}$
$K^+ \to \pi^+\pi^0$	$(20.66 \pm 0.08)\%$
$K^+ \to \pi^+\pi^0\pi^0$	$(1.761 \pm 0.022)\%$
$K^+ \to \mu^+\nu_\mu$	$(63.55 \pm 0.11)\%$
$K^+ \to \mu^+\pi^0\nu_\mu$	$(3.353 \pm 0.034)\%$
$K^+ \to e^+\nu_e\gamma$ (IB)	$1.65 \cdot 10^{-6}$
$K^+ \to e^+\nu_e\gamma$ $(SD-)$	$2.58 \cdot 10^{-6}$

Table 3.1: Decay channels contributing to the background to the $K^+ \to e^+\nu_e\gamma(SD+)$ decay and their Branching Ratios (PDG 2008 [14]); the value of the Branching Ratio of the other two $K^+ \to e^+\nu_e\gamma$ components is the theoretical one (table 1.1) taken from [20].

All the other kaon decays are background to the signal, but some of them, due to the final state characteristic or the Branching Ratio value, are more relevant. Only a restricted sample of decay channels has been simulated and analyzed with the same signal selection code in order to optimize the selection criteria. In particular, only decays with one charged particle in the final state have been taken into account. Table 3.1 shows a list of the decays, with their Branching Ratio, considered for the background evaluation. They can fake the signal final state in the following ways:

- $K^+ \to e^+\pi^0\nu_e$: this channel can fake the $K^+ \to e^+\nu_e\gamma$ decay in the following two ways: if the neutral pion decays into two photons and one of them is lost, absorbed before the LKr or out of the calorimeter acceptance, the final state is identical to the signal one; if the π^0 decays in the Dalitz mode and the electron and one positron are lost, the two final states are identical.

- $K^+ \to e^+\pi^0\nu_e\gamma$: this channel can simulate the signal in many ways, the most straightforward is when all the decay products of the π^0 aren't detected.
- $K^+ \to e^+\pi^0\pi^0\nu_e$: in this case the background mechanism depends on the decay type of the two π^0.
- $K^+ \to e^+\nu_e$: this channel has the same final state of the signal if the positron emits a radiative photon.
- $K^+ \to \pi^+\pi^0$: in the case that the π^0 decays in two photons, if one photon is lost and the π^+ is mis-identified as a positron, the $K^+ \to \pi^+\pi^0$ has the same signature of the signal; if the π^0 decays in γe^+e^-, there are two possible cases: 1) the positron and the electron are lost, and the π^+ is mis-identified as a positron; 2) the charged pion and the electron are lost.
- $K^+ \to \pi^+\pi^0\pi^0$: also in this case the background mechanism depends on the decay type of the two π^0 and the pion mis-identification as a positron.
- $K^+ \to \mu^+\nu_\mu$: this decay produces the same signature of the signal if the muon is identified as a positron and a photon is produced via the bremsstrahlung process.
- $K^+ \to \mu^+\pi^0\nu_\mu$: in the case that the π^0 decays in two photons, if one photon is lost and the μ^+ is mis-identified as a positron, the $K^+ \to \mu^+\pi^0\nu_\mu$ has the same signature of the signal; if the π^0 decays in γe^+e^-, there are two possible cases: 1) the positron and the electron are lost and the μ^+ is mis-identified as a positron; 2) the muon and the electron are lost.

A muon, coming for example from $K^+ \to \mu^+\nu_\mu$, can be mis-identified as a positron in the following two ways:

1. the muon can release completely its energy in the calorimeter by a *catastrophic bremsstrahlung*;
2. the muon can decay in a positron through the process $\mu^+ \to e^+\nu_e\bar{\nu_\mu}$:

A charged pion, coming for example from $K^+ \to \pi^+\pi^0$, can be mis-identified as a positron in the following two ways:

1. the π^+ can release completely his energy in the calorimeter;
2. the π^+ can decay in a positron through the process $\pi^+ \to e^+\nu_e$ ($BR = (1.230 \pm 0.004) \cdot 10^{-4}$).

As it is explained in the next chapter (section 4.2) a charged track is identified as a positron asking that the ratio between the energy released in the calorimeter and the momentum of the track is ~ 1, considering that a positron releases all his energy in the *LKr*.

In order to better treat the rejection of the background channels with muons in the final state, the two different samples, with or without the muon decay, were studied separately.

3.4 Monte-Carlo checks

Due to the very low $K^+ \to e^+\nu_e\gamma$ statistics ($BR \sim 10^{-5}$), the reliability of the Monte-Carlo simulation has been checked using $K^+ \to e^+\pi^0\nu_e$ events. This decay mode has been used for the kaon flux measurement (chapter 5) due to its similarity to the signal. All the MC distributions have been normalized to the kaon flux.

Figure 3.1 shows the MC/Data comparison for the squared missing mass, defined as $(P_K - P_e)^2$. Figure 3.2 shows the MC/Data comparison for the z coordinate of the decay vertex. In figures 3.3, 3.4 and 3.5, the MC/Data comparisons for the positron momentum and for the energy of the 2 photons coming from the π^0 decay are reported, in the last figure there is also the K-less contribution obtained from a special run without the kaon beam in order to consider the beam halo background. All MC/Data comparisons exhibit a good agreement. Some problems have been found for the last comparison, 3.5, where there is a discrepancy in the right part of the distribution; this discrepancy is due to a not very good normalization of the K-less contribution. The good results obtained for the MC/Data comparison validate the MC simulation.

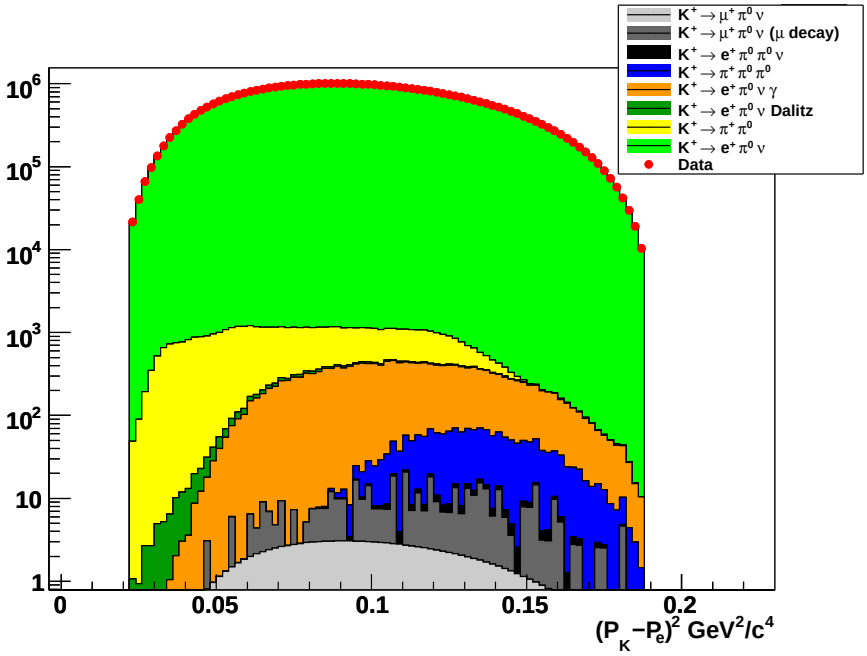

Figure 3.1: MC/Data comparison for the squared missing mass: the dots represent the Data, $K^+ \to e^+\pi^0\nu_e$ and different background MC contributions are plotted in colour according to the legend.

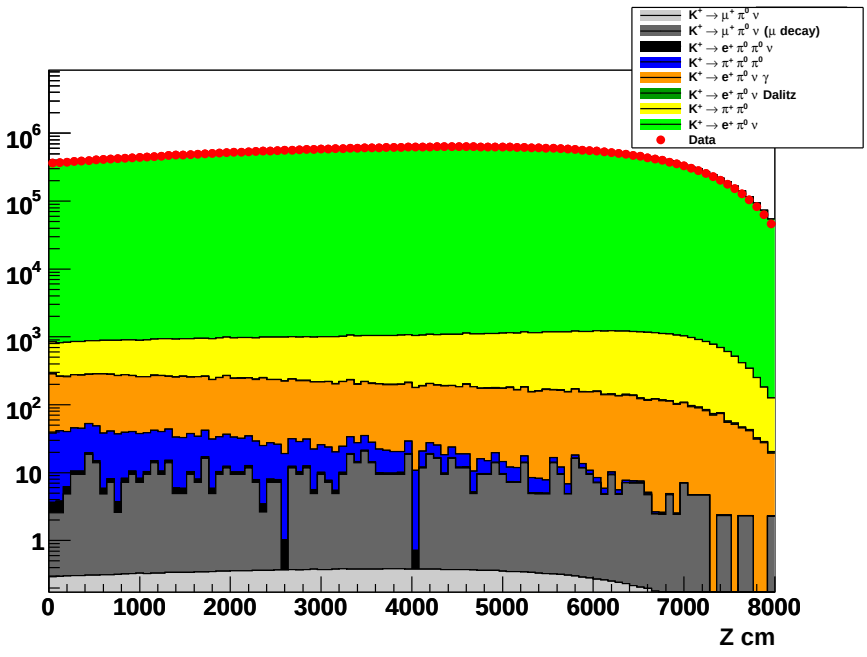

Figure 3.2: MC/Data comparison for the decay vertex: the dots represent the Data, $K^+ \to e^+\pi^0\nu_e$ and different background MC contributions are plotted in colour according to the legend

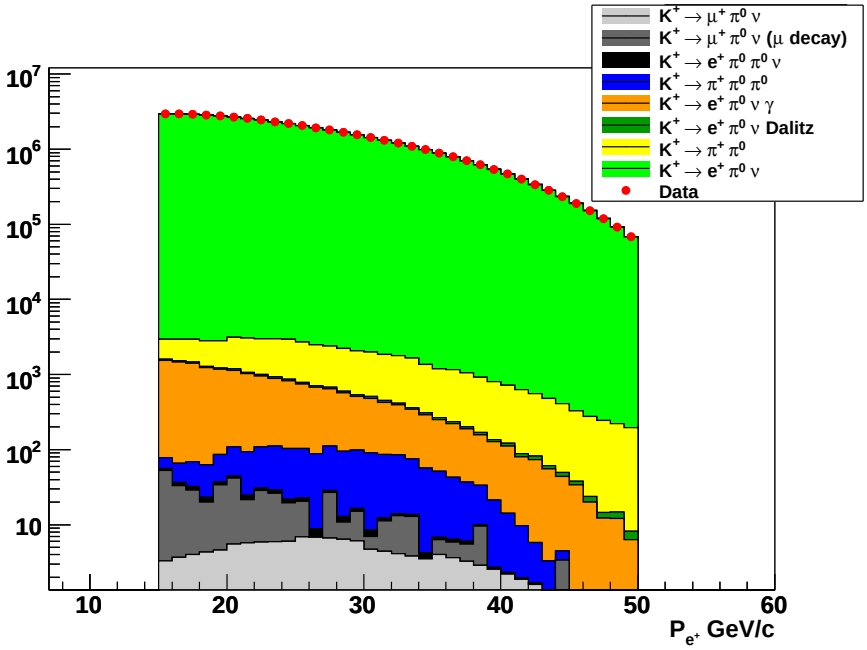

Figure 3.3: MC/Data comparison for the squared missing mass: the dots represent the Data, $K^+ \to e^+\pi^0\nu_e$ and different background MC contributions are plotted in colour according to the legend

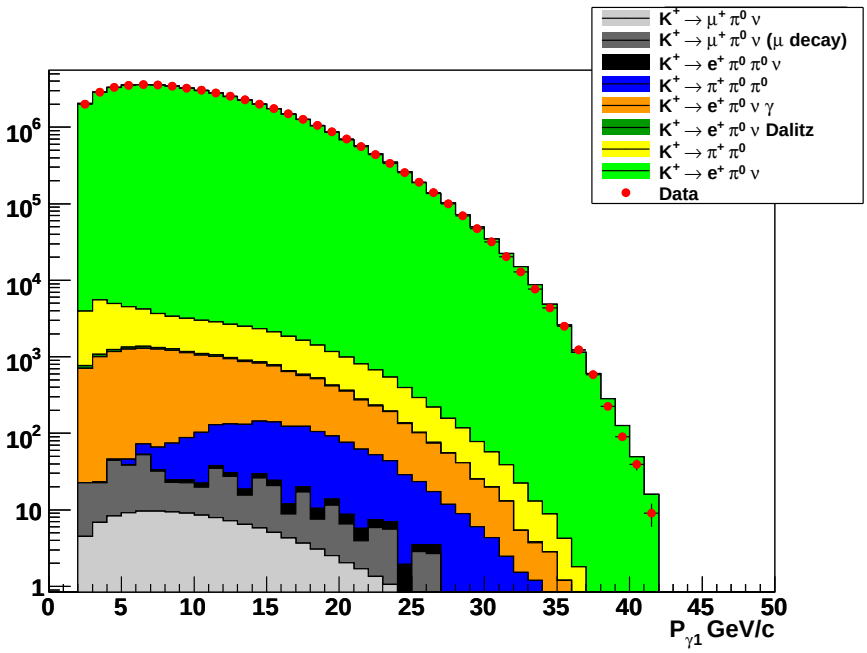

Figure 3.4: MC/Data comparison for the squared missing mass: the dots represent the Data, $K^+ \to e^+\pi^0\nu_e$ and different background MC contributions are plotted in colour according to the legend

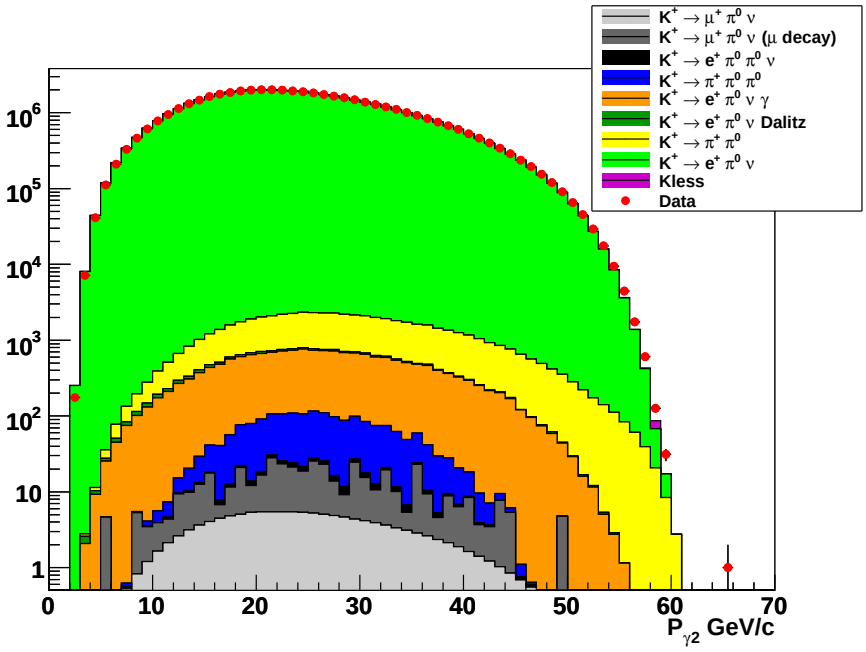

Figure 3.5: MC/Data comparison for the squared missing mass: the dots represent the Data, $K^+ \to e^+\pi^0\nu_e$ and different background MC contributions are plotted in colour according to the legend

Chapter 4

Event selection

The selection aims to distinguish signal events from the background sources; particular attention has been payed to the rejection of $K^+ \to e^+\pi^0\nu_e$ and $K^+ \to \pi^+\pi^0$ decays whose Branching Ratios are orders of magnitude higher with respect to the signal one.

To properly evaluate acceptance corrections and to measure the amount of residual background, the same selection criteria have been applied to Data and MC samples, except for requirements on time which are not simulated by *CMC*.

The first part of the selection is dedicated to select one good charged track, identified as a positron, produced in the fiducial decay region and coming from the decay vertex of the kaon. Then, the cluster multiplicity in the LKr is considered; in particular, only one good cluster, not associated to the charged track, is requested. The final part of the selection takes into account the kinematics of the $K^+ \to e^+\nu_e\gamma$ decay, imposing a condition on the angle between the positron and the candidate radiative photon. The final separation between the signal and the main background, $K^+ \to e^+\pi^0\nu_e$ and $K^+ \to \pi^+\pi^0$, is done using the squared missing mass variables, that represent the invariant mass of the neutral particles not visible with the magnetic spectrometer.

4.1 Preliminary Corrections

To fix different anomalous effects, a set of specific corrections is applied to Data and MC events, before performing the event reconstruction. Details of the corrections applied, listed in table 4.1, are given below:

"Blue" Field

The small residual magnetic field in the vacuum tank bends the trajectories of

charged decay products so that the direction measured at *DCHs* is slightly different from the one at the decay point.

A precise map of the "blue" field [1] allows to correct track direction before reconstructing the longitudinal position of the kaon decay vertex.

DCH Alpha and Beta

A miscalibration of the spectrometer magnetic field and a misalignment of one of the *DCHs* located downstream the magnet, spoil the momentum measurement inducing a wrong $K^{\pm}$ mass reconstruction. $K^+ \to \pi^+\pi^+\pi^-$ events have been used to study such effect because they can be fully reconstructed employing *DCH* spectrometer information only [41].

- *Magnetic field miscalibration*: because $\frac{\Delta p}{p} = \frac{\Delta B}{B}$, it can be demonstrated that $\frac{m_{3\pi} - m_{K^+}}{m_{K^+}} \simeq 0.2 \cdot \frac{\Delta B}{B}$, $m_{3\pi}$ is the reconstructed kaon mass and m_{K^+} is the average value of experimentally measured kaon mass given by the PDG [14]; the effect is independent on the track charge; the corrected track momentum p can be expressed as:

  $$p = p_0 \cdot (1 + \beta)$$

  where p_0 is the uncorrected quantity and $\beta = \frac{\Delta B}{B} = \frac{m_{K^+} - m_{3\pi}}{0.1046}$;

- *DCH misalignment*: the displacement of one *DCH* downstream the magnet gives opposite effects according to the track sign and the magnetic field direction; the correction can be parametrized as:

  $$p = p_0 \cdot (1 + \alpha \cdot q \cdot p_0)$$

  where p_0 is the uncorrected momentum, $\alpha = \frac{m^+_{3\pi} + m^-_{3\pi}}{1.7476}$ and q is the particle charge ($\pm$). As the K^+ is reconstructed from two positive and one negative tracks, its mass is shifted in opposite direction compared to the K^- (two negative and one positive tracks). If the magnet polarity is swapped, the sign of the mass splitting is swapped as well and the explicit dependence of the correction and the determination with magnetic field sign can be omitted.

The whole Data sample of P5 has been analyzed in order to evaluate, on a burst by burst basis, the β value. As described before, to evaluate the α correction a K^- beam is necessary. As only a K^+ beam is present during the P5, at the end of this period a run with both the kaon polarities has been taken to evaluate the

[1] the fact that the cylindrical vacuum chamber is painted blue gives the nickname to the magnetic field.

corresponding α parameter. The coefficient obtained has been then used to apply the correction for the entire P5.

LKr **Non-Linearity**
A threshold applied to the calorimeter cells readout introduces a non-linear response between the deposited and measured energy which is not reproduced by the MC simulation. Then a correction to eliminate this non-linearity is applied to the Data.

Correction	**Data**	**MC**
Blue Field	$\surd$	$\surd$
DCH Alpha and Beta	$\surd$	$\surd$
LKr Non-Linearity	$\surd$	X

Table 4.1: Corrections summary ($\surd$ = applied, X = not applied).

4.2 Charged track requirements

The selection requires only one charged track in a time window of $[118 \div 158]$ ns with the following conditions:

- when a particle crosses the magnetic spectrometer, the corresponding track is reconstructed and a quality variable, based on the number of the hits in each *DCH* view, is computed; a minimum value of 0.7 for the track quality is requested;
- regions close to the beam pipe and to the edge of the sub-detectors are removed:
  1. cut on the radial distance at the first, second and the fourth drift chambers:
  $$12\,\text{cm} < R_{DCH} < 105\,\text{cm}$$
  2. octagonal shaped cut and requirements on the minimum track radial distance from the beam pipe at the electromagnetic calorimeter:
  $$R_{LKr} > 15\,\text{cm}$$
  3. cut on the radial distance from the beam pipe at the two planes of the charged hodoscope:
  $$14\,\text{cm} < R_{CHOD1} < 105\,\text{cm}$$

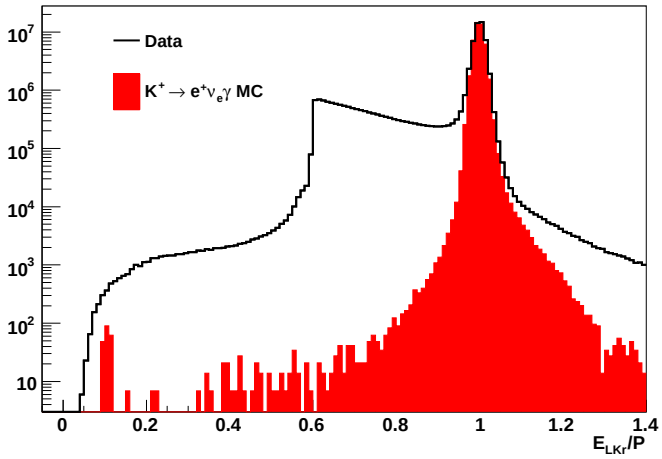

Figure 4.1: E_{LKr}/P distribution for Data, black line, and MC of signal, red; the cut visible at $\sim$ 0.6 in the Data distribution is due to the *L3* filter. The MC normalization is arbitrary.

$$14\,\text{cm} < R_{CHOD2} < 105\,\text{cm}$$

- only tracks with a momentum between 15 GeV/c and 50 GeV/c are selected, the lower value is related to the trigger request of a minimum energy of 10 GeV in the calorimeter; the upper value is chosen in order to maximize the rejection of the $K^+ \to \pi^+\pi^0$ background.

The identification of the charged track is performed studying the ratio between the energy deposition in the calorimeter (E_{LKr}) and the momentum measured with the magnetic spectrometer (P). In case of positrons, this quantity has a sharp peak at unity because all the energy has been fully released as electromagnetic shower. For pions and hadrons in general, the distribution is quite broad starting from 0 up to 0.9 (Fig. 4.1),because they do not deposit all their energy. For non-interacting minimum ionizing particles, such as muons, it peaks at small values.

In order to calculate the E_{LKr}/P, the correct cluster has to be associated to the charged track. The particular shapes of the different distributions allow to identify the particles.

The following conditions have the aim to associate one cluster to the charged track and to identify it with a positron:

- the radial distance between the associated candidate cluster and the extrapolated track position at the *LKr* must be smaller than 1.5 cm;

- the cluster-track time difference must be smaller than 5 ns, the distribution is reported in figure 4.2;

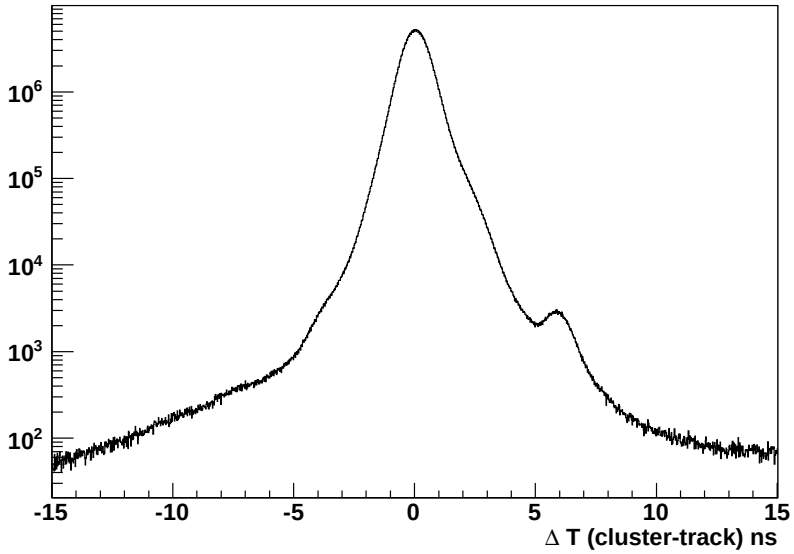

Figure 4.2: Cluster-track time difference. The asimmetry of the peack, with a large number of events at positive ΔT, is due to the pion contamination and the small peak at 6 ns is due to pion back splash in the wall of the hadronic calorimeter.

- the E_{LKr}/P must be in the interval $0.95 < E_{LKr}/P < 1.1$ to identify the track as a positron.

4.3 Decay vertex reconstruction

The determination of the decay vertex (called Charged Vertex) can be obtained by computing the Closest Distance of Approach (CDA) between the nominal kaon trajectory and positron trajectory corrected for the "blue" field effect. The CDA vertex coordinate Z_{VCDA} can be defined in terms of the coordinates of points P_1 and P_2, belonging to the two tracks (Fig. 4.3), as follows:

$$Z_{VCDA} = \frac{Z(P_1) + Z(P_2)}{2}$$

where P_1 and P_2 are the points along the two tracks where the distance between them assumes the minimum value. Figure 4.4 shows the reconstructed Z_{VCDA}, the dashed line represent the final collimator position.

The signal selection requires $(0 < Z_{VCDA} < 8000)$ cm. The lower value is chosen in order to minimize effects from the presence of the final collimator (~ -1800 cm) that could not be well enough modeled in the simulation, while the upper value rejects events decaying too close to the main detector to be properly reconstructed.

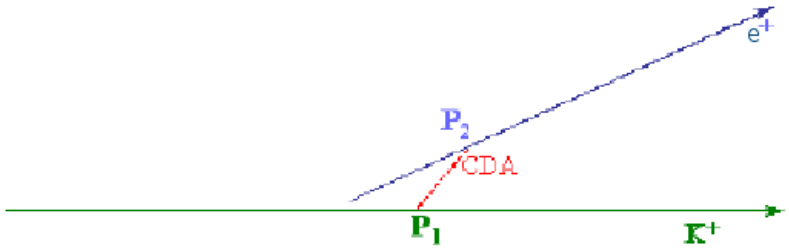

Figure 4.3: Schematic view of the Z_{VCDA} evaluation technique.

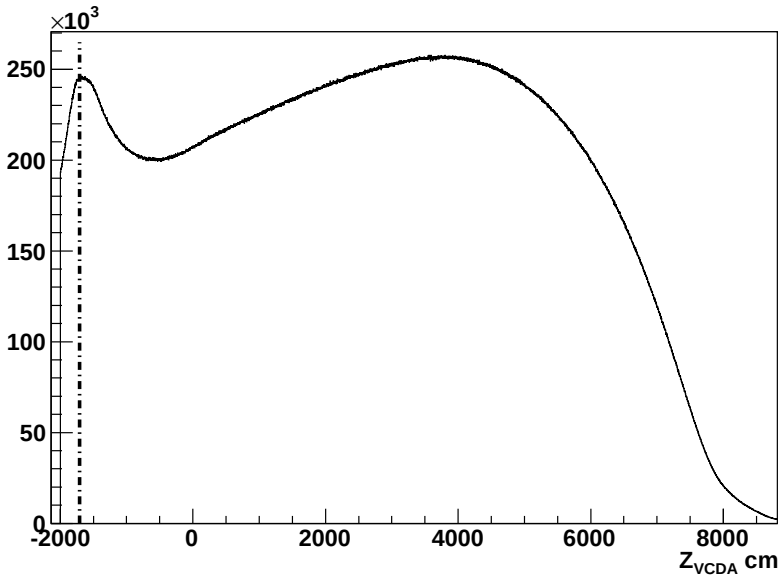

Figure 4.4: Longitudinal coordinate of the Charged Vertex; the dashed line represent the final collimator position.

To ensure that the charged track comes from the kaon decay only, events with $CDA < 2$ cm are selected; the CDA distribution is reported in figure 4.5.

4.4 Electromagnetic cluster requirements

Provided the cluster reconstruction (section 2.6.1) has been successfully performed, the following additional conditions must be satisfied:

- the clusters must be in the same time window of the charged track $[118 \div 158]ns$;
- the cluster-track time difference must be smaller than 5 ns;

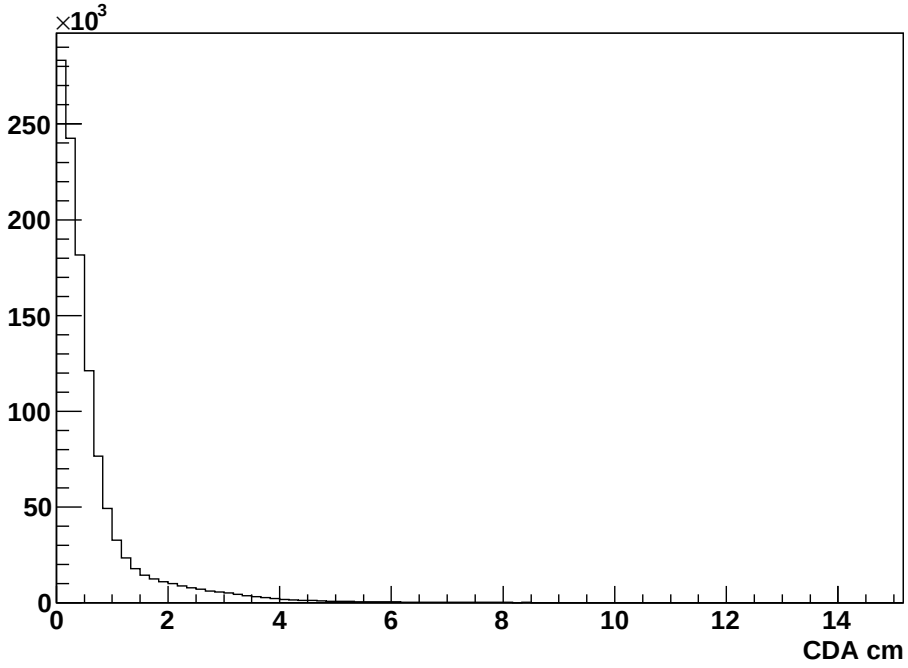

Figure 4.5: CDA distribution.

- the clusters must be fully contained within the electromagnetic calorimeter active volume, the same acceptance region applied to the charged track impact point;

- the distance from the closest LKr dead cell must be greater than 2 cm to avoid any energy loss and ensure a good energy reconstruction;

- to avoid clusters overlapping, a minimum distance from the positron impact point at the LKr equal to 20 cm has been required;

- the energy of the clusters must be greater than 2 GeV, this value is the minimum energy compatible with a good cluster reconstruction;

- to reject events in which the cluster is due to bremsstrahlung of the charged track, a minimum distance of 6 cm between the cluster and the extrapolation of the positron track to the calorimeter, without considering the magnet curvature, is required. As it can be seen from the figure 4.6, at a distance close to 0 cm there is a peak due to events for which the cluster is produced by a bremsstrahlung photon. To justify the assumption of the bremsstrahlung process as a source of the additional photon close to the positron track, the distribution of the $K^+ \to e^+\nu_e$ MC has been reported. A good $K^+ \to e^+\nu_e$ event is characterized by only one cluster associated to the positron; a second

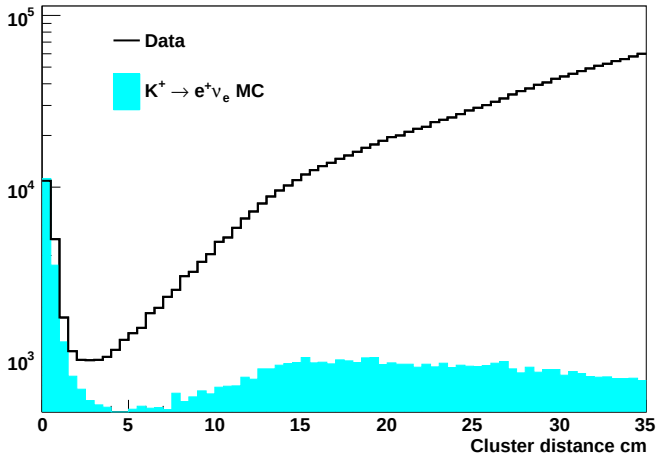

Figure 4.6: Distance between the extrapolation of the charged track without magnet curvature to the LKr cluster: Data, in black line and MC of $K^+ \to e^+\nu$ in cyan. The MC normalization is arbitrary.

cluster in the events can only be due to a secondary photon produced by the bremsstrahlung process.

Clusters that satisfy the conditions described above, are recognized as associated to the radiative photon.

Only events with one well reconstructed track identified as a positron, and only one cluster compatible with the radiative photon are further analyzed.

4.5 Kinematical selection

The final part of the signal selection takes into account the kinematics of the decay. Considering the conservation of the momentum and of the spin, it is possible to obtain the favoured $K^+ \to e^+\nu_e\gamma$ event configurations displayed in figure 4.7(a,b,c). In the case of $SD+$, the radiative photon and the positron have opposite directions in the kaon rest frame. On the contrary, in the case of $SD-$ and IB, the γ and the positron have the same direction. In the kaon rest frame there is also a difference in the energy spectrum of the γ (Fig. 4.8) and of the positron (Fig. 4.9). For the $SD+$ component, the photon energy is peaked close to the kinematical limit of $\sim m_K/2$; for the IB component, the radiative γ has the energy close to zero and for the $SD-$ one the energy distribution is between the two limits. For the positron energy, the situation is slightly different. For the $SD+$ and IB components, the energy distribution is peaked at the same kinematical limit with a little shift between the two peaks, while the $SD-$ component produces a distribution at lower value of

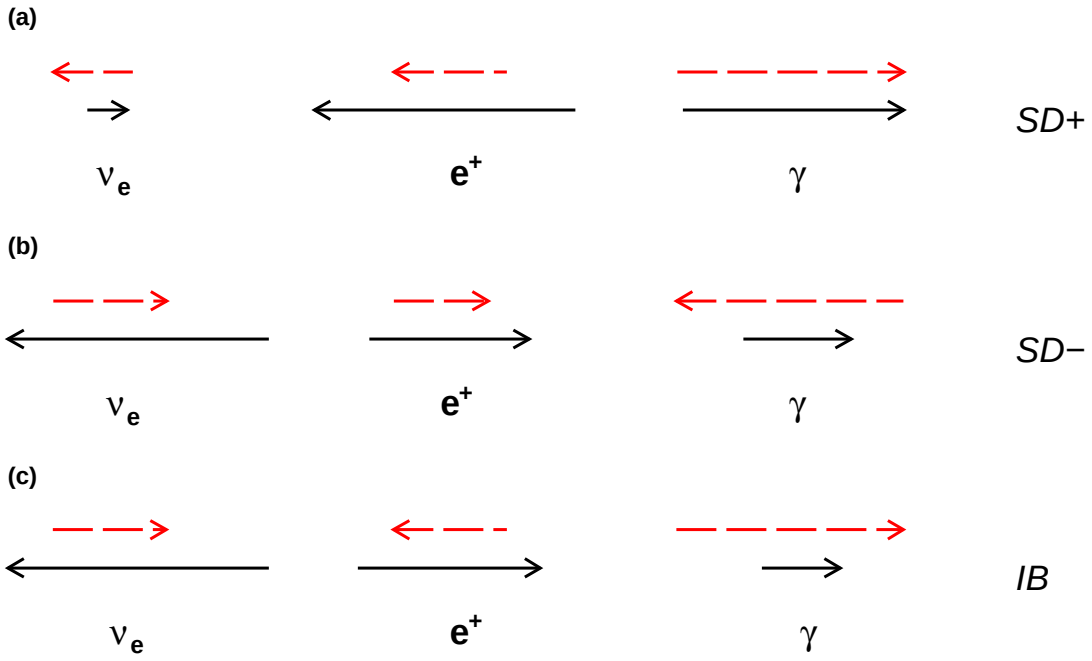

Figure 4.7: Favoured $K^+ \to e^+\nu_e\gamma$ events configuration: (a) $SD+$, (b) $SD-$ and (c) IB (dashed arrows represent the spin and continuous arrows represent the particle momentum).

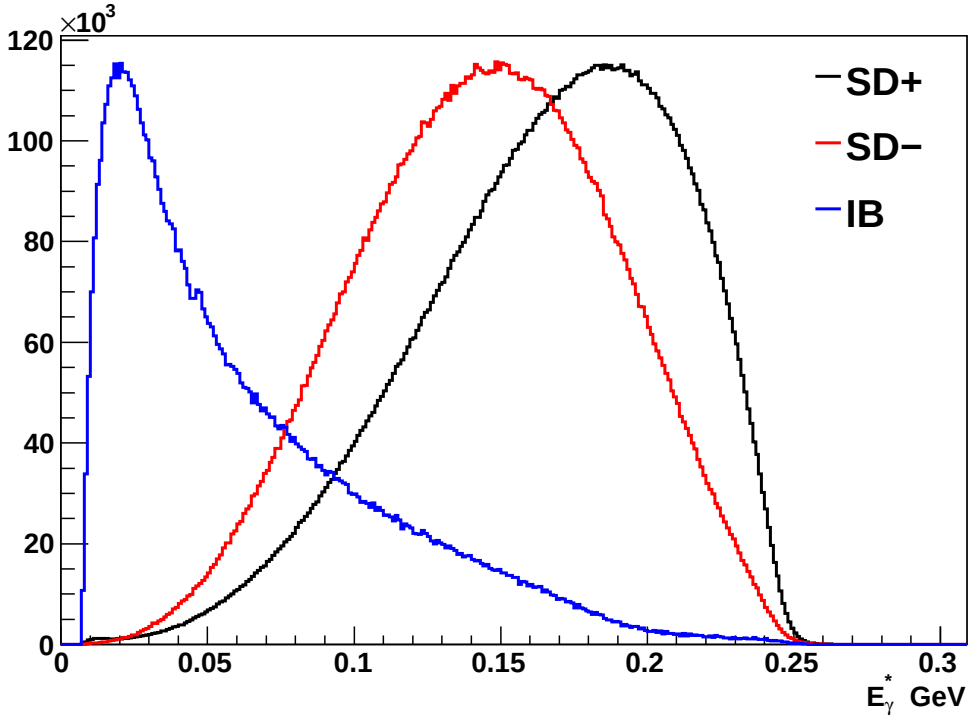

Figure 4.8: Energy distributions in the kaon rest frame for the radiative photon.

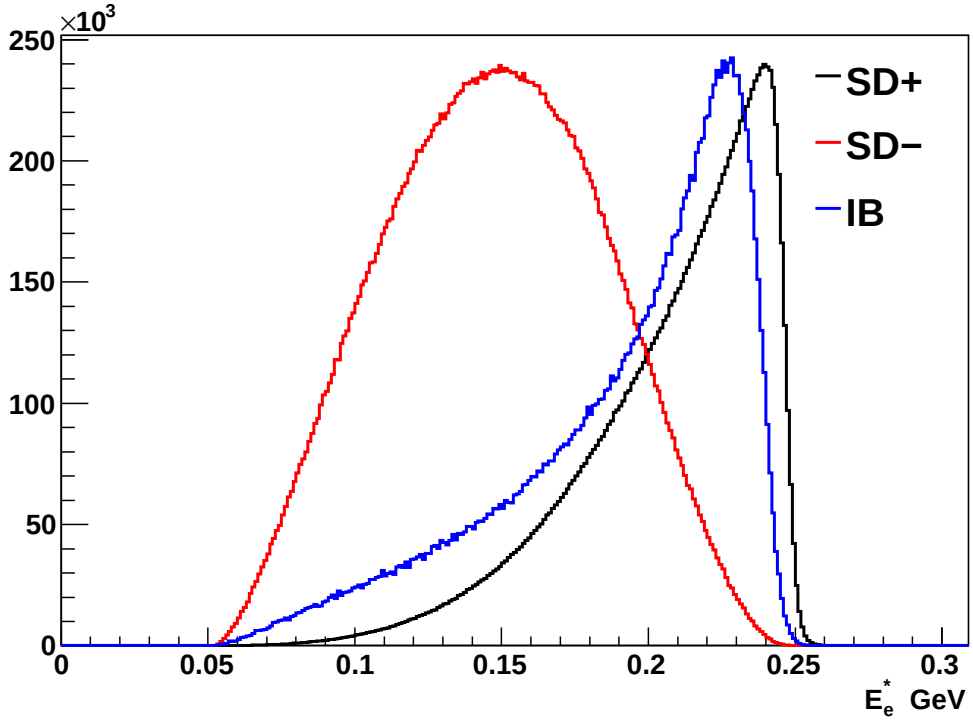

Figure 4.9: Energy distributions in the kaon rest frame for the positron.

energy. The difference in the decay kinematics between the three $K^+ \to e^+\nu_e\gamma$ components can be seen also in the Dalitz plot reported in figure 4.10. To separate the signal from background due to the $K^+ \to e^+\nu_e\gamma$ components other than $SD+$ and from the residual $K^+ \to e^+\nu_e$ events, the condition $cos(\theta^*_{e\gamma}) < -0.720$ is applied. This condition corresponds to the requirementof an angle $\theta^*_{e\gamma} \geq 136°$; figure 4.11 shows $cos(\theta^*_{e\gamma})$ distribution. The value used for the cut is a compromise between a good signal to background ratio (S/B) and a good statistics left at the end of the selection.

After the application of all the cuts and the conditions described above, the residual main background contribution comes from the $K^+ \to e^+\pi^0\nu_e$ with one photon lost. To reject this background, the squared missing mass spectrum, defined as the difference between the kaon 4-momentum and the positron 4-momentum ($(P_K - P_e)^2$), is used. As it can be seen from figure 4.12, the signal distribution is around zero with a tail at positive value of the missing mass due to the presence of the radiative photon. For the $K^+ \to e^+\pi^0\nu_e$ decay the distribution has positive values up to the kinematical limit at 0.18 GeV^2/c^4. The non perfect agreement between Data and MC is due to the $K^+ \to \pi^+\pi^0$ decay not included in the plot. The squared missing mass cut is $-0.012\ GeV^2/c^4 < (P_K - P_e)^2 < 0.012\ GeV^2/c^4$, all the events outside this region are rejected. The upper limits of this condition corresponds to

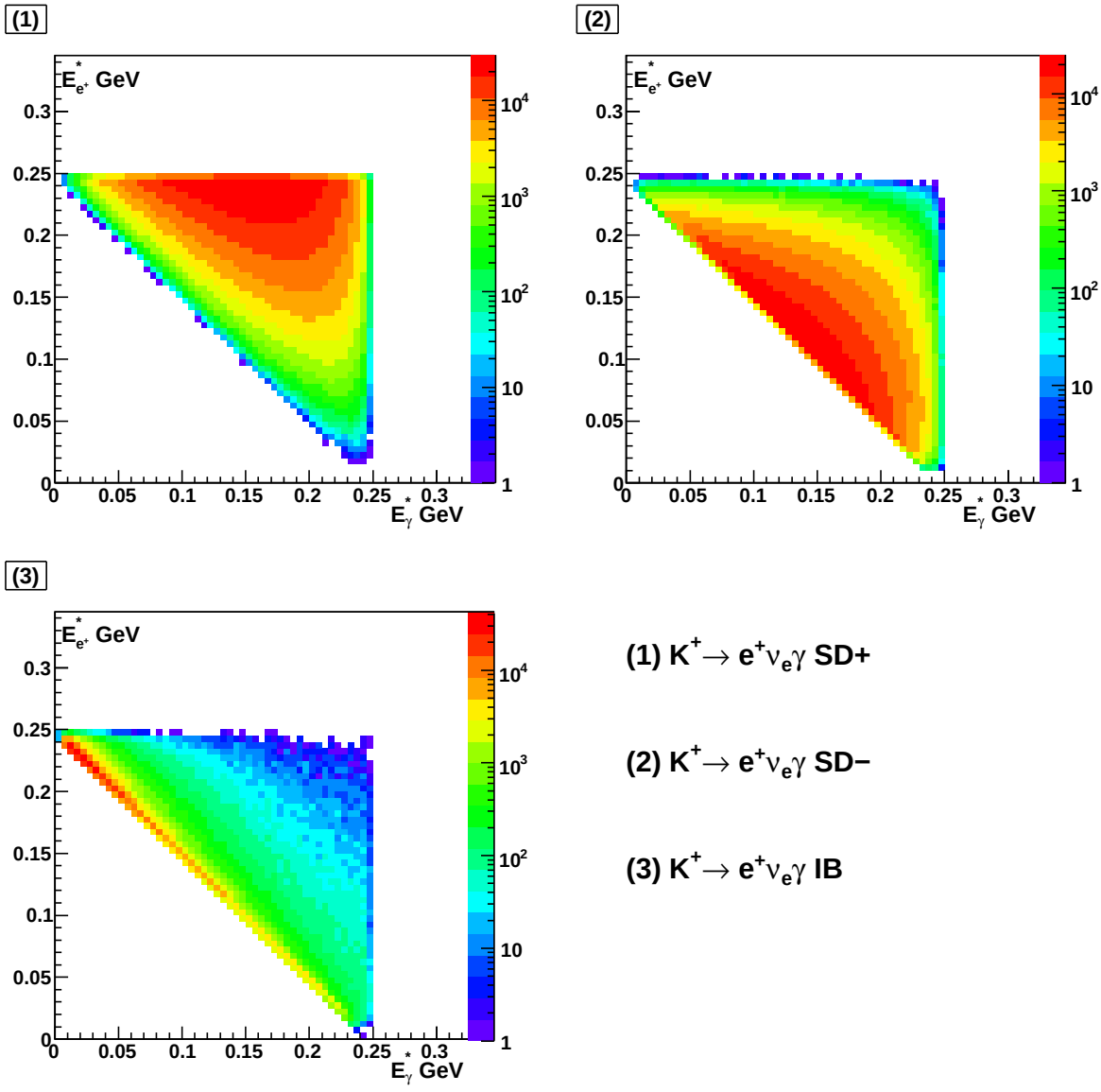

Figure 4.10: Dalitz plot for the three $K^+ \to e^+\nu_e\gamma$ components.

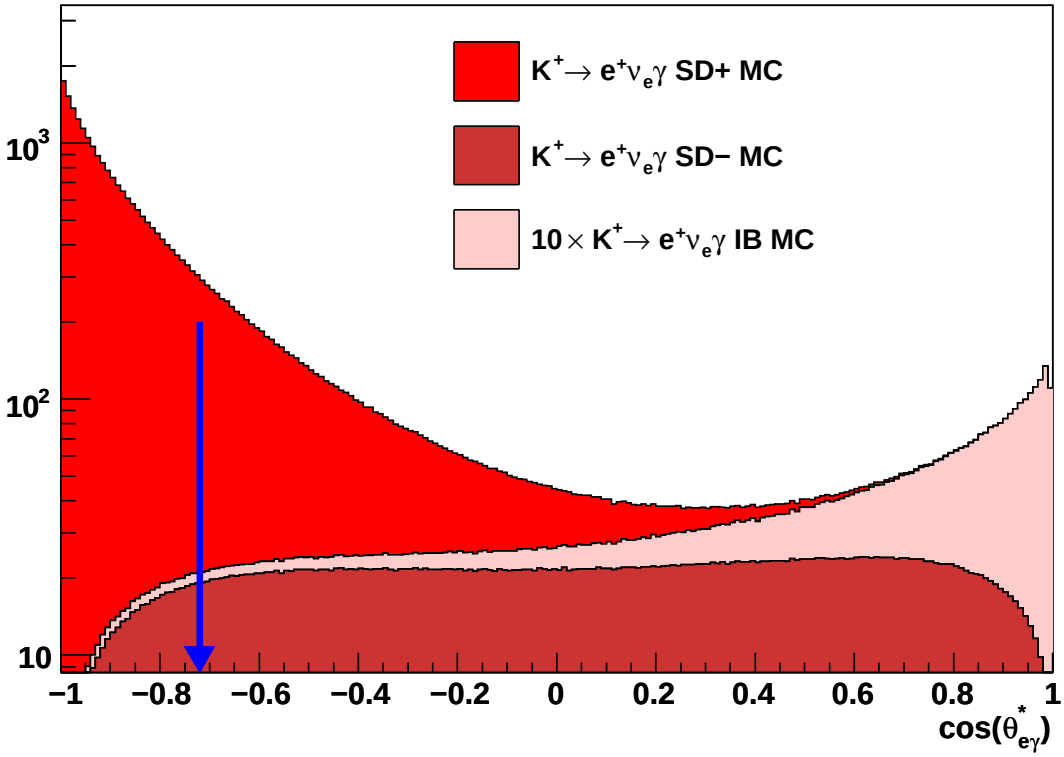

Figure 4.11: Angle between the positron and the photon in the kaon rest frame: MC of $K^+ \to e^+\nu\gamma(SD+)$, $K^+ \to e^+\nu\gamma(SD+)$ and $K^+ \to e^+\nu\gamma(IB)$ according to the legend, the blue arrow represents the cut applied in the selection. The distributions has been normalized accordind to the theoretical Branching Ratios, taken from table 1.1. The IB contribution has been multiplied by a factor of 10.

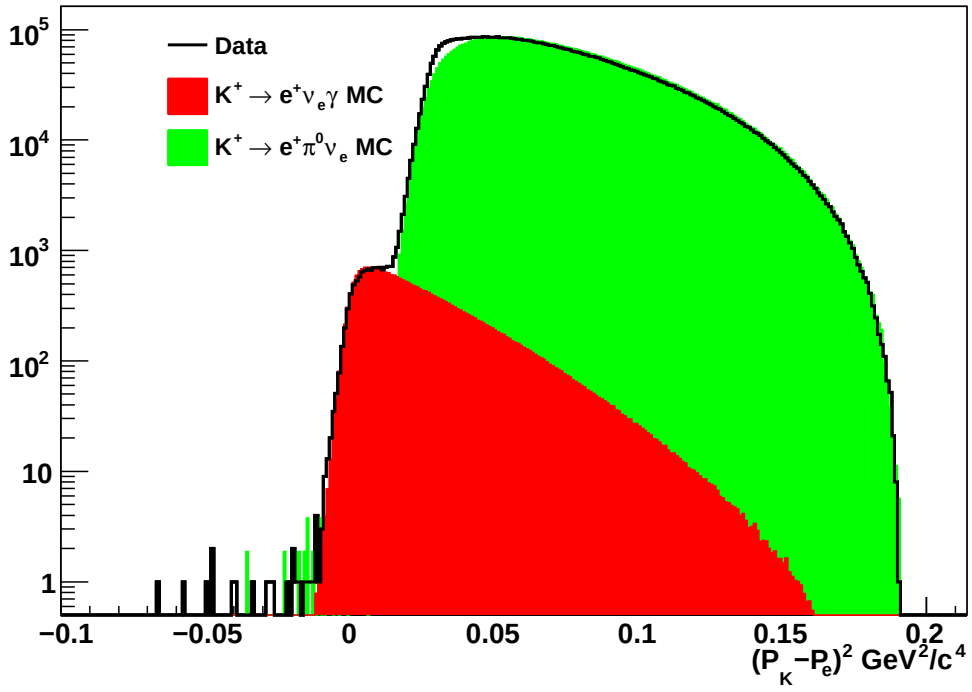

Figure 4.12: Squared missing mass distribution for Data, signal and $K^+ \to e^+\pi^0\nu_e$ MC according with the legend.

cut on the energy of the positron in the kaon rest frame $E_e^* > 0.235\ GeV$.

Another useful variable to discriminate the signal from the background is the 3-body squared missing mass defined as the difference between the 4-momentum of the kaon and the 4-momenta of the positron and the photon, $((P_K - P_e - P_\gamma)^2)$. For $K^+ \to e^+\nu_e\gamma$ events, this variable is the neutrino squared missing mass and the distribution should be a peak at 0 GeV^2/c^4. Figure 4.13 shows the distribution of the 3-body squared missing mass. The plot shows also a tail at negative values due to the residual $K^+ \to \pi^+\pi^0$ background.

In the selection, the cut $-0.012\ GeV^2/c^4 < (P_K - P_e - P_\gamma)^2 < 0.012\ GeV^2/c^4$ around the peak is applied.

Figure 4.14 shows the distribution of the variable $x = \frac{2 \cdot E_\gamma^*}{m_K}$. For the $K^+ \to e^+\nu_e\gamma$ decay, the kinematical region of the variable is $0 \leq x \leq 1 - r_e$, where $r_e = \frac{m_e^2}{m_K^2}$. As it can be seen from the figure, the x distribution spreads above the upper limit at ~ 1. This is due to resolution effects on the energy measurement, and on the background contamination. In order to respect the kinematical restriction, the final condition selects only the events with $0 \leq x \leq 1$.

Table 4.2 reports the reduction in the number of reconstructed events as a function of the most important cuts and conditions. At the beginning of the selection, the

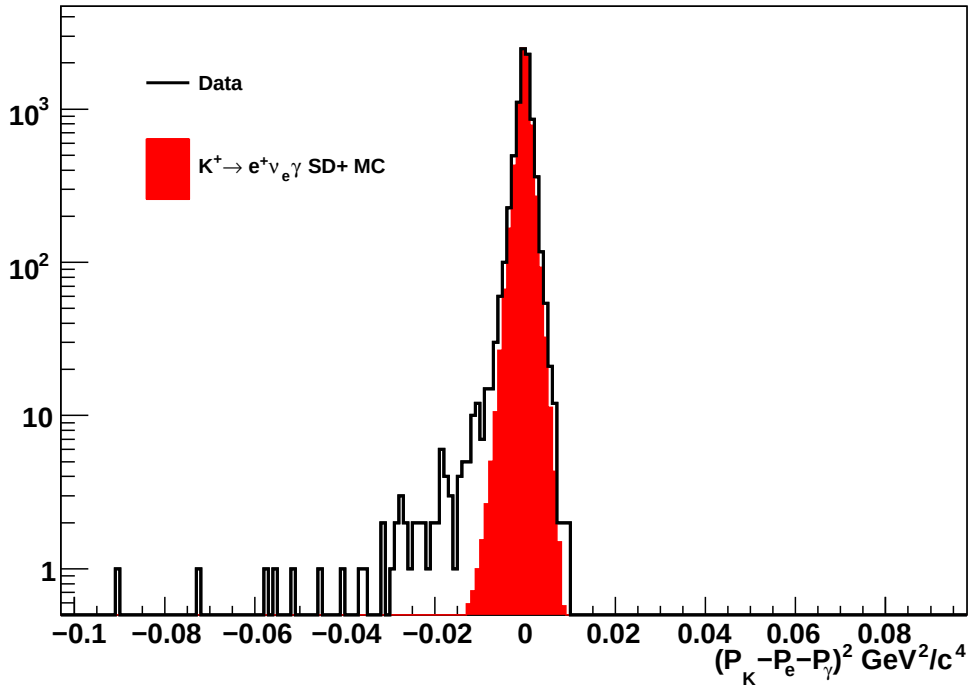

Figure 4.13: 3-body squared missing mass: Data in black lineand signal MC in red.

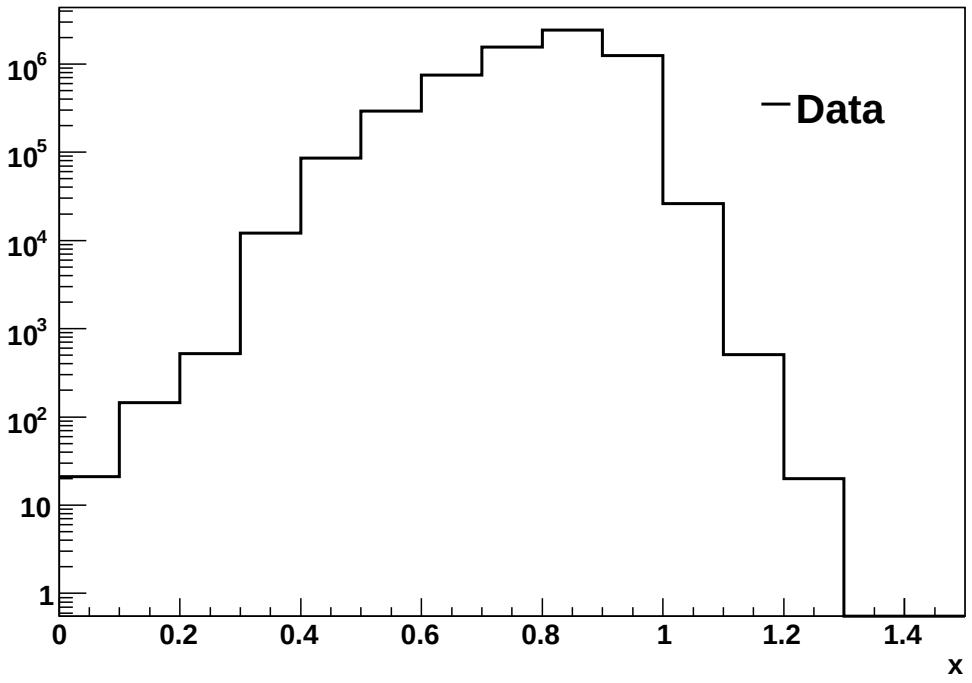

Figure 4.14: x distribution

Condition	N_{events}
Initial Sample	$2.14 \cdot 10^9$
1 good positive track	$1.39 \cdot 10^9$
Geometrical Acceptance	$1.24 \cdot 10^9$
Decay vertex	$8.3 \cdot 10^8$
Track momentum	$1.98 \cdot 10^8$
1 candidate cluster ass. to the radiative γ	$6.8 \cdot 10^7$
1 cluster associated to the positron	$4.9 \cdot 10^7$
$cos(\theta^*_{e\gamma})$	$2.05 \cdot 10^7$
3-body squared missing mass	$6.8 \cdot 10^6$
squared missing mass	8300
Final Sample	8278

Table 4.2: Reduction in the number of reconstructed events as a function of the most important selection cuts and conditions.

initial sample contains $2.14 \cdot 10^9$ reconstructed events, at the end of the selection the final sample consists of 8278 reconstructed events.

Chapter 5

Kaon flux measurement

Due to the fact that NA48/2 detector has no direct way to evaluate the number of kaon decays, the kaon flux has to be calculated using a different, well known decay. In this analysis, the best choice for the normalization channel is $K^+ \to e^+\pi^0\nu_e$ (Ke3) decay, due to the following reasons:

- the signal and this decay are very similar. They have one charged track only, a positron, and one photon of difference in the final state. For this reason, they have been acquired through the same trigger chain; this leads to smaller trigger efficiency systematics;
- the $K^+ \to e^+\pi^0\nu_e$ decay is virtually background free and very simple to select due to its high BR and its final state.

In order to not introduce possible systematic effect related to difference between the signal selection and the normalization one, most of the cuts are common to the two selections.

5.1 The $K^+ \to e^+\pi^0\nu_e$ selection

The charged track requirements and the decay vertex conditions are the same applied to the signal (section 4.2 and 4.3).

5.1.1 π^0 reconstruction

At the beginning of the π^0 reconstruction, all the clusters are paired and the invariant mass of the cluster is calculated. The candidate pair of clusters is the one with a minimum value of $|m_{\gamma\gamma} - m_{\pi^0}(PDG)|$, where the $m_{\gamma\gamma}$ is the invariant mass of the two clusters, and $m_{\pi^0}(PDG)$ is the mass of the neutral pion taken from the PDG

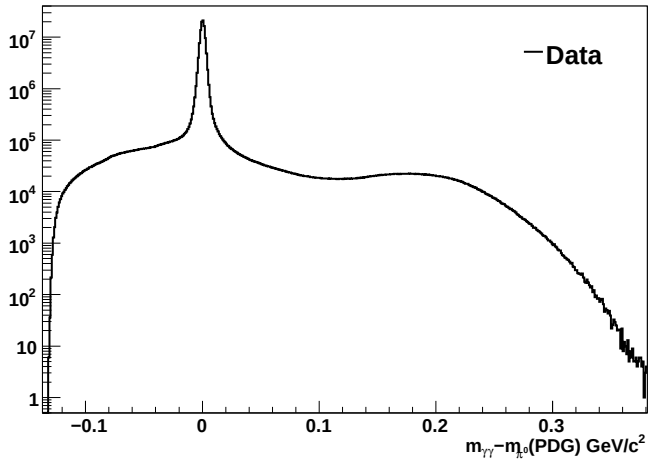

Figure 5.1: $m_{\gamma\gamma} - m_{\pi^0}(PDG)$ distribution.

[14]. Figure 5.1 shows the distribution of $m_{\gamma\gamma} - m_{\pi^0}(PDG)$. The big tails are due to the background.

The following conditions must be satisfied by the two candidate photons of the π^0 decay:

- the clusters must be in the same time window of the charged track $[118 \div 158]$ ns;
- the cluster-track time difference must be smaller than 5 ns;
- the cluster-cluster time difference must be smaller than 3 ns (figure 5.2);
- the clusters must be fully contained within the electromagnetic calorimeter active volume, the same acceptance region applied to the charged track impact point;
- the distance from the closest LKr dead cell must be greater than 2 cm to avoid any energy loss and ensure a good energy reconstruction;
- in order to avoid overlapping showers effects, a minimum distance of the clusters from the positron impact point at the LKr equal to 20 cm has been required;
- to avoid energy sharing effects between the clusters, a minimum distance equal to 20 cm between them has been required ;
- the energy of each cluster must be greater than 2 GeV;

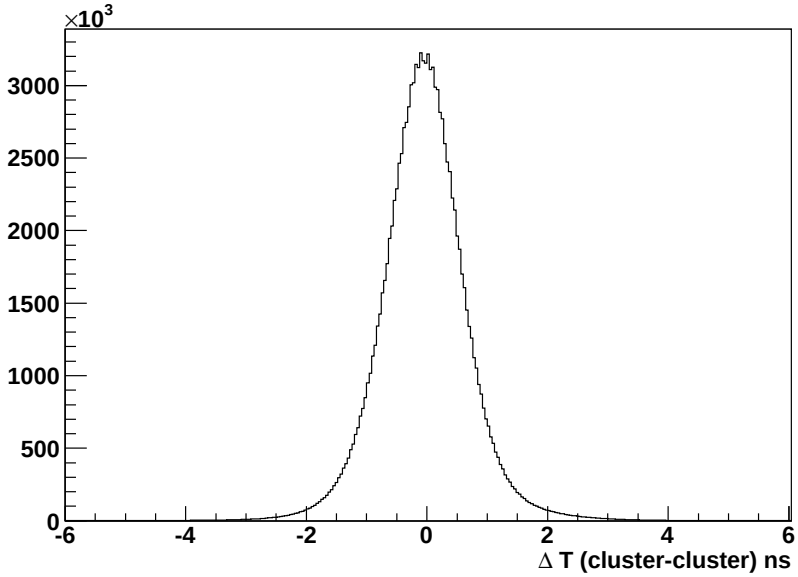

Figure 5.2: Cluster-cluster time difference.

- in order to reject events for which the photons are due to the charged track bremsstrahlung, a minimum distance of 6 cm between each cluster and the extrapolation of the positron to the calorimeter, without considering the magnet curvature, has been required.

The final π^0 reconstruction has been done by imposing a cut on $|m_{\gamma\gamma} - m_{\pi^0}(PDG)|$ to be smaller than 0.01 GeV/c^2.

5.1.2 Kinematical selection

At this level of the selection, the main contribution to the background to the $K^+ \to e^+\pi^0\nu_e$ decay is coming from the $K^+ \to \pi^+\pi^0$ decay, with the charged pion misidentified as a positron. In the Ke3 decay, the presence of the neutrino in the final state produces a loss of transverse momentum since the neutrino is not visible by the detector. In the $K^+ \to \pi^+\pi^0$ decay, all the particles of the final state are visible, and can be reconstructed in the detector. In figure 5.3, the distribution of the squared missing transverse momentum calculated with respect to the kaon direction is shown. As it can be seen, a cut at $p_T^2 > 0.02\ GeV/c$ can separate the Ke3 signal from the $K^+ \to \pi^+\pi^0$ background.

For a Ke3 decay, the variable $(P_K - P_e - P_{\pi^0})^2$, where P_K is the kaon 4-momentum, P_e is the electron 4-momentum and P_{π^0} is the 4-momentum of π^0, represents the neutrino squared missing mass. The distribution is peaked at 0 GeV^2/c^4, as it can be seen from figure 5.4. On the other hand for a $K^+ \to e^+\pi^0\nu_e\gamma$ event with one photon

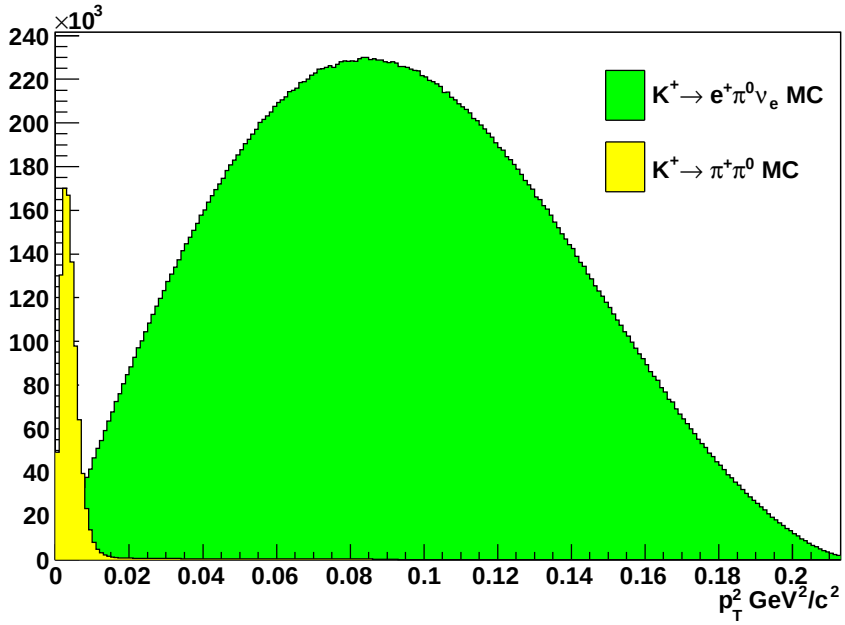

Figure 5.3: p_T^2 distribution: $K^+ \to e^+\pi^0\nu_e$ and $K^+ \to \pi^+\pi^0$ MC.

lost before the electromagnetic calorimeter or out of acceptance, $(P_K - P_e - P_{\pi^0})^2$ represents the squared missing mass of the system $\nu_e\gamma\gamma$, and the distribution assume a large tail, comparable with the peack, at positive value (figure 5.4). To reject this kind of background, the final condition selects only events with $|(P_K - P_e - P_{\pi^0})^2| < 0.01\ GeV^2/c^4$. All MC/Data comparisons concerning the Ke3 selection show a good agreement (section 3.4).

5.2 Kaon flux measurement

The kaan flux evaluation takes into account the fact that the selection described in the above sections select Ke3 events with the neutral pion decay in two photon. Once $K^+ \to e^+\pi^0\nu_e$ candidate events have been identified, the number of kaon decays can be extracted according to the formula:

$$\Phi(K^+) = \frac{N_{Ke3\gamma\gamma}}{BR(K^+ \to e^+\pi^0\nu_e) \cdot BR(\pi^0 \to \gamma\gamma) \cdot \eta_{Ke3\gamma\gamma} \cdot \epsilon_{Ke3\gamma\gamma}},$$

with $N_{Ke3\gamma\gamma}$ being the number of reconstructed Ke3 events with the π^0 decaying in 2γ, $BR(K^+ \to e^+\pi^0\nu_e) = (0.0507 \pm 0.0004)$ [14], $BR(\pi^0 \to \gamma\gamma) = (0.98823 \pm 0.00034)$ [14], $\eta_{Ke3\gamma\gamma}$ is the decay acceptance obtained with MC simulation, and $\epsilon_{Ke3\gamma\gamma}$ is the $Q1 \times LKrMBias \times 1TRKLM$ trigger efficiency measured from Data (see section 2.10.4 for the trigger definition), a detailed description of the trigger

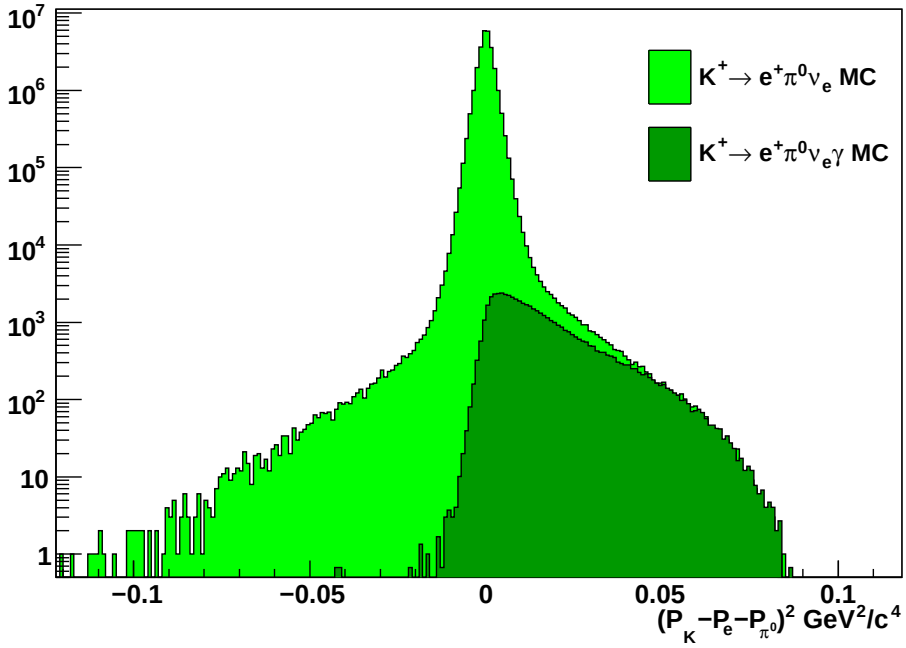

Figure 5.4: $(P_K - P_e - P_{\pi^0})^2$ distribution: $K^+ \to e^+\pi^0\nu_e$ and $K^+ \to e^+\pi^0\gamma\nu_e$ MC.

efficiency measurement will be explained in the next section. In the formula, the $BR(\pi^0 \to \gamma\gamma)$ has been considered to take into account the fact that the selection introduced in the first part of this chapter reconstructs only Ke3 events with a consecutive π^0 decay in two photons.

The acceptance is defined as the ratio between the number of MC Ke3 events reconstructed at the end of the selection divided by the number of Ke3 MC events generated in a given decay region, $(-1000 < Z_{gen} < 9000)$ cm, where Z_{gen} is the generated Z coordinate of the decay vertex, this region is the same taken into account for the signal acceptance.

Using the values listed below,

$$N_{ke3\gamma\gamma} = 47263397,$$

$$\eta_{ke3\gamma\gamma} = 0.11146 \pm 0.00002,$$

$$\epsilon_{ke3\gamma\gamma} = 0.99596 \pm 0.00012,$$

the result for the kaon flux is:

$$\Phi(K^+) = (8.50 \pm 0.07) \cdot 10^9.$$

This value represents the number of kaons decayed during the P5 Data sample in

the fiducial decay region between $(-1000, 9000)$ cm.

5.2.1 Trigger efficiency

The following general procedure has been adopted to measure the trigger efficiency: first, a control sample has been identified; then, the proper event selection has been performed on the chosen Data set, and, finally, a check whether the trigger condition is satisfied is performed.

The efficiency has been defined as the ratio between the number of reconstructed events satisfying the trigger condition, taken from the Pattern Units, and the total number of reconstructed decays in the control sample selected with the control trigger taken form the Trigger Word produced by the Trigger Supervisor. The corresponding error has been determined according to the binomial distribution. The main trigger requires a coincidence of 3 sub-signal. For the trigger efficiency measurement the signal is made performing the coincidence of the 3 sub-signals taken from the Pattern Units.

Given that the positron and the photons coming from Ke3 decay release all their energy in LKr, and that T0N gives positive decision consequently to an energy release in the electromagnetic calorimeter, the T0N, independent of the 3 signals producing the main trigger, has been chosen as control trigger. The T0N signal rate has been downscaled by a factor 150 with the consequence to reduce the sample for the trigger efficiency measurement. The corresponding trigger efficiency has been defined as:

$$\epsilon_{Q1\times LKrMBias\times 1TRKLM} = \frac{N_{T0N,Q1\times LKrMBias\times 1TRKLM}}{N_{T0N}},$$

and the error is:

$$\sigma^2_{\epsilon_{Q1\times LKrMBias\times 1TRKLM}} = \frac{\epsilon_{Q1\times LKrMBias\times 1TRKLM}\cdot(1-\epsilon_{Q1\times LKrMBias\times 1TRKLM})}{N_{T0N}},$$

where $N_{T0N,Q1\times LKrMBias\times 1TRKLM}$ is the number of reconstructed events in the control sample satisfying the main trigger conditions, while N_{T0N} is the number of events satisfying the T0N (the control sample).

The measured efficiency of the 3 single components and of the main trigger is reported in table 5.1. It is important to check the stability of the trigger efficiency with respect to the characteristic of the Ke3 decay. In order to understand the trigger stability, the efficiency has been evaluated as a function of some variables. In figure 5.5 and 5.6, the main trigger efficiency has been plotted as a function of

Trigger	Efficiency
Q1	(0.9977 ± 0.0001)
$LKrMBias$	(0.999997 ± 0.000003)
1TRKLM	(0.9992 ± 0.0001)
$Q1 \times LKrMBias \times 1TRKLM$	(0.99596 ± 0.00012)

Table 5.1: Trigger efficiency results.

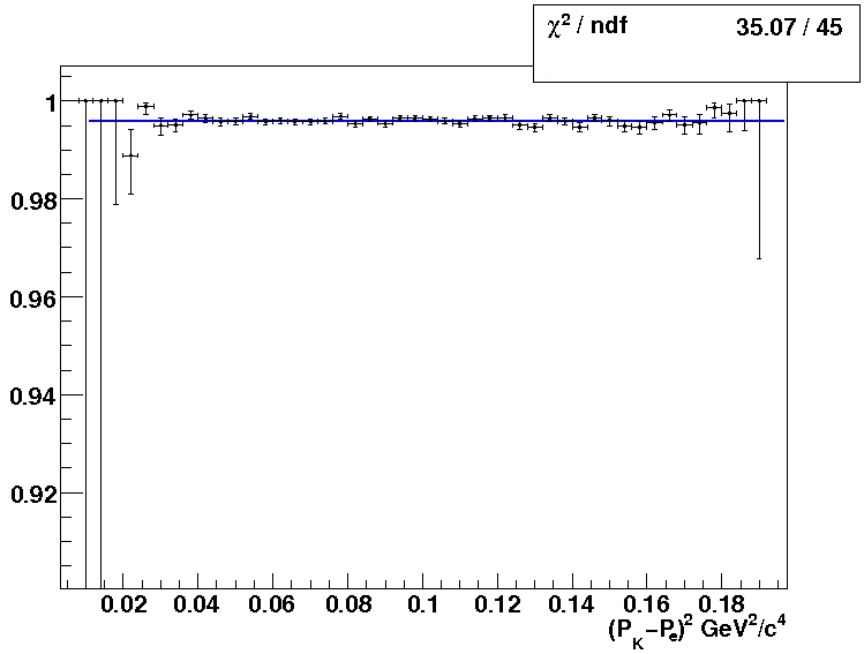

Figure 5.5: Trigger efficiency as a function of the squared missing mass.

the squared missing mass and the track momentum respectively. In these plots and in the all other with the asymmetric errors, the technique descibed in [42] has been used. As it can be seen from the figures the efficiency is stable with respect to the two variables.

5.2.2 Background rejection

A dedicated study of background events to the $K^+ \to e^+\pi^0\nu_e$ decay has been performed: the main background sources to the Ke3 decay are reported in table 5.2, with the relative Background to Signal ratio, calculated in the following way:

$$B/S = \frac{N_{bg_i}}{N_{Ke3}} \tag{5.1}$$

where

$$N_{bg_i} = \Phi_0 \cdot \eta_{bg_i} \cdot BR(bg_i)$$

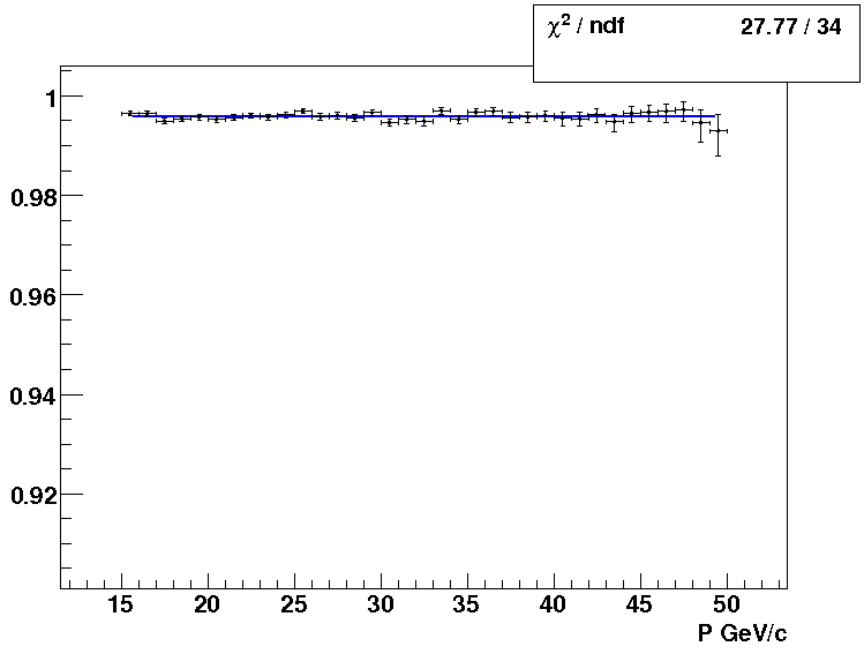

Figure 5.6: Trigger efficiency as a function of the track momentum.

and

$$N_{Ke3} = \Phi_0 \cdot \eta_{Ke3} \cdot BR(Ke3)$$

Φ_0 is an arbitrary kaon flux fixed at 10^{10}, $\eta_{bg_i,Ke3}$ is the background and Ke3 acceptance and BR is the Branching Ratio.

The very small amount of residual background ($\sim$ 0.12%), mainly due to the

Channel	**B/S**
$K^+ \to e^+\pi^0\nu_e\gamma$	$\sim 3.4 \cdot 10^{-4}$
$K^+ \to e^+\pi^0\nu_e \quad Dalitz$	$\sim 1.9 \cdot 10^{-5}$
$K^+ \to e^+\pi^0\pi^0\nu_e$	$\sim 9.8 \cdot 10^{-7}$
$K^+ \to \pi^+\pi^0$	$\sim 8.5 \cdot 10^{-4}$
$K^+ \to \pi^+\pi^0\pi^0$	$\sim 3.1 \cdot 10^{-5}$
$K^+ \to \mu^+\pi^0\nu_\mu$	$\sim 2.8 \cdot 10^{-6}$
$K^+ \to \mu^+\pi^0\nu_\mu \quad (\mu \to e)$	$\sim 7.3 \cdot 10^{-6}$

Table 5.2: Background contribution to the Ke3 decay.

$K^+ \to \pi^+\pi^0$ with the charged pion identified as an electron ($\sim$ 0.085%), has been neglected in the kaon flux measurement.

Chapter 6

Results

The $K^+ \to e^+\nu_e\gamma$ (SD+) Branching Ratio is given by:

$$BR(K^+ \to e^+\nu_e\gamma(SD+)) = \frac{N_{e^+\nu_e\gamma(SD+)} - N_{bg}}{\Phi(K^+) \cdot A_{e^+\nu_e\gamma(SD+)} \cdot \epsilon_{e^+\nu\gamma}} \tag{6.1}$$

where $N_{e^+\nu_e\gamma(SD+)}$ is the number of reconstructed candidate for signal decay, N_{bg} is the number of events cominf from residual background estimated with the *CMC* simulation, $\Phi(K^+)$ is the total kaon flux (see chapter 5) and $\epsilon_{e^+\nu\gamma}$ is the trigger efficiency. $A_{e^+\nu_e\gamma(SD+)}$ is the MC signal acceptance defined as the ratio between the number of reconstructed events at the end of the selection ($N^{end}_{e^+\nu_e\gamma(SD+)}$) and the number of generated events in a given decay region, ($-1000 < Z_{gen} < 9000$) cm, ($N^{in}_{e^+\nu_e\gamma(SD+)}$):

$$A_{e^+\nu_e\gamma(SD+)} = \frac{N^{end}_{e^+\nu_e\gamma(SD+)}}{N^{in}_{e^+\nu_e\gamma(SD+)}}$$

In table 6.1 the values of $N_{e^+\nu_e\gamma(SD+)}$ and $A_{e^+\nu_e\gamma(SD+)}$, evaluated using a signal MC simulation based on ChPT at $O(p^6)$ model, are reported.

The residual background has been evaluated using the formula:

$$N_{bg} = \Phi(K^+) \cdot \sum_{bg_i} BR(bg_i) \cdot A_{bg_i} \cdot \epsilon_{e^+\nu\gamma} \tag{6.2}$$

being $BR(bg_i)$ the single decay channel Branching Ratio taken from [14], and A_{bg_i} is the corresponding acceptance.

$N_{e^+\nu_e\gamma(SD+)}$	8278 ± 91
$A_{e^+\nu_e\gamma(SD+)}$	0.06108 ± 0.00005

Table 6.1: Number of reconstructed signal candidate and the $K^+ \to e^+\nu_e\gamma$ acceptance.

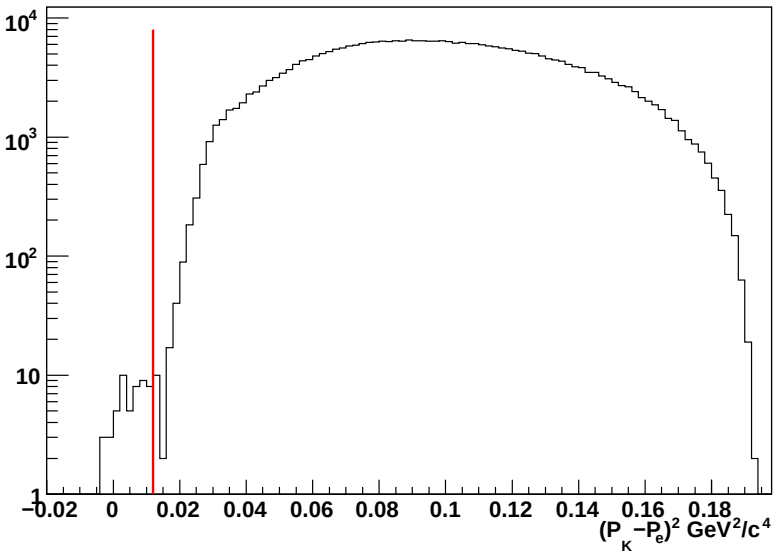

Figure 6.1: Squared missing mass distribution used for trigger efficiency measurement, the red line represents the upper cut applied in the selection.

6.1 Trigger efficiency

The procedure used for the trigger efficiency measurement is the same as described in section 5.2.1.

Table 4.2 shows that after the application of the squared missing mass condition the number of events are reduced by a factor of 10^3. As a consequence of this, the first measurement of the trigger efficiency has been done before the squared missing mass cut. Figure 6.1 shows the $(P_K - P_e)^2$ distribution used to evaluate the efficiency. The red line in figure represents the cut $(P_K - P_e)^2 < 0.012\ GeV^2/c^4$. As it can be seen from the figure, the missing mass cut limits the control sample to ~ 50 events only, which is not enough to evaluate the efficiency. In figure 6.2, the trigger efficiency has been plotted as a function of the squared missing mass. The red line in the plot represents again the cut upplied on missing mass. In the signal region, on the left hand side of the line, the efficiency is 100% due to the smallness of the control sample. Considering this situation, the efficiency has been measured in the region $(P_K - P_e)^2 > 0.012\ GeV^2/c^4$ (called background region) on the right hand side of the red line of figure 6.2, with the aim to use this value also in the signal region. The results are reported in figure 6.3 and in table 6.2.

Comparing the results of table 6.2 with those of table 5.1, the efficiency of Q1 and the $LKrMBias$ components are in perfect agreement. On the contrary, the 1TRKLM trigger is more inefficient if measured with the signal selection (once

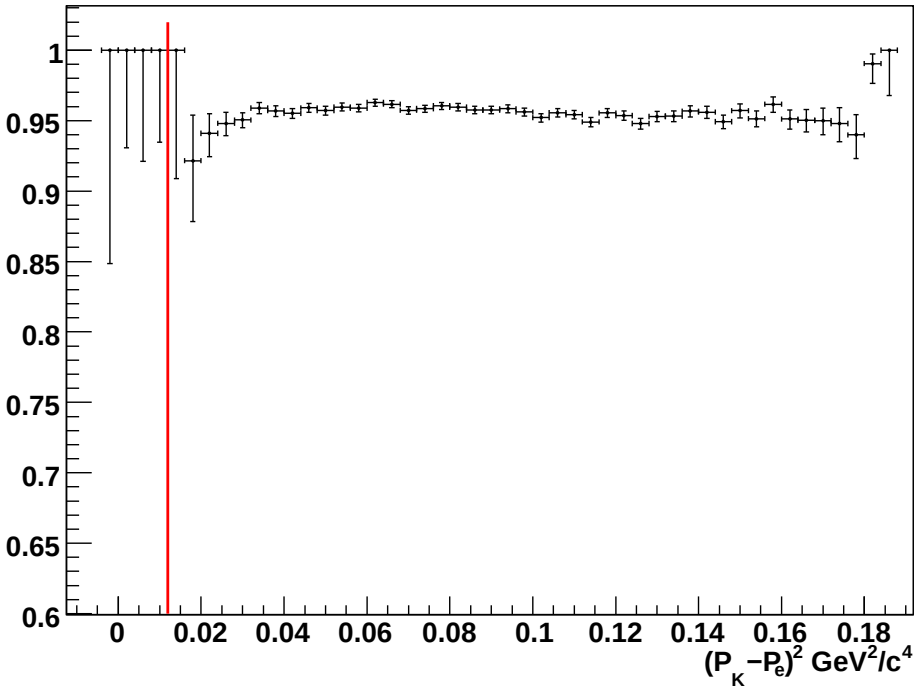

Figure 6.2: Trigger efficiency as a function of the squared missing mass, the red line represent the squared missing mass selection cut.

Trigger	Efficiency
Q1	(0.99755 ± 0.00013)
$LKrMBias$	$1.00000_{-0.00001}$
1TRKLM	(0.9622 ± 0.0005)
$Q1 \times LKrMBias \times 1TRKLM$	(0.9565 ± 0.0006)

Table 6.2: Trigger efficiency results.

the cut on missing mass is removed) with respect to that measured with the Ke3 selection.

This inefficiency can be explained as follows: the major contribution to the background, in region $(P_K - P_e)^2 > 0.012\ GeV^2/c^4$, are the $K^+ \to e^+\pi^0\nu_e$ decays with 1 lost photon. The photon can be lost in the following 2 ways:

1. the γ is out of the LKr calorimeter acceptance

2. the γ has been absorbed before the LKr

The first case is not relevant for the trigger. In the second case the photon can be absorbed in the region of the drift chambers producing a shower starting mainly in the beam pipe, due to the high Z of the material with respect to the helium. The

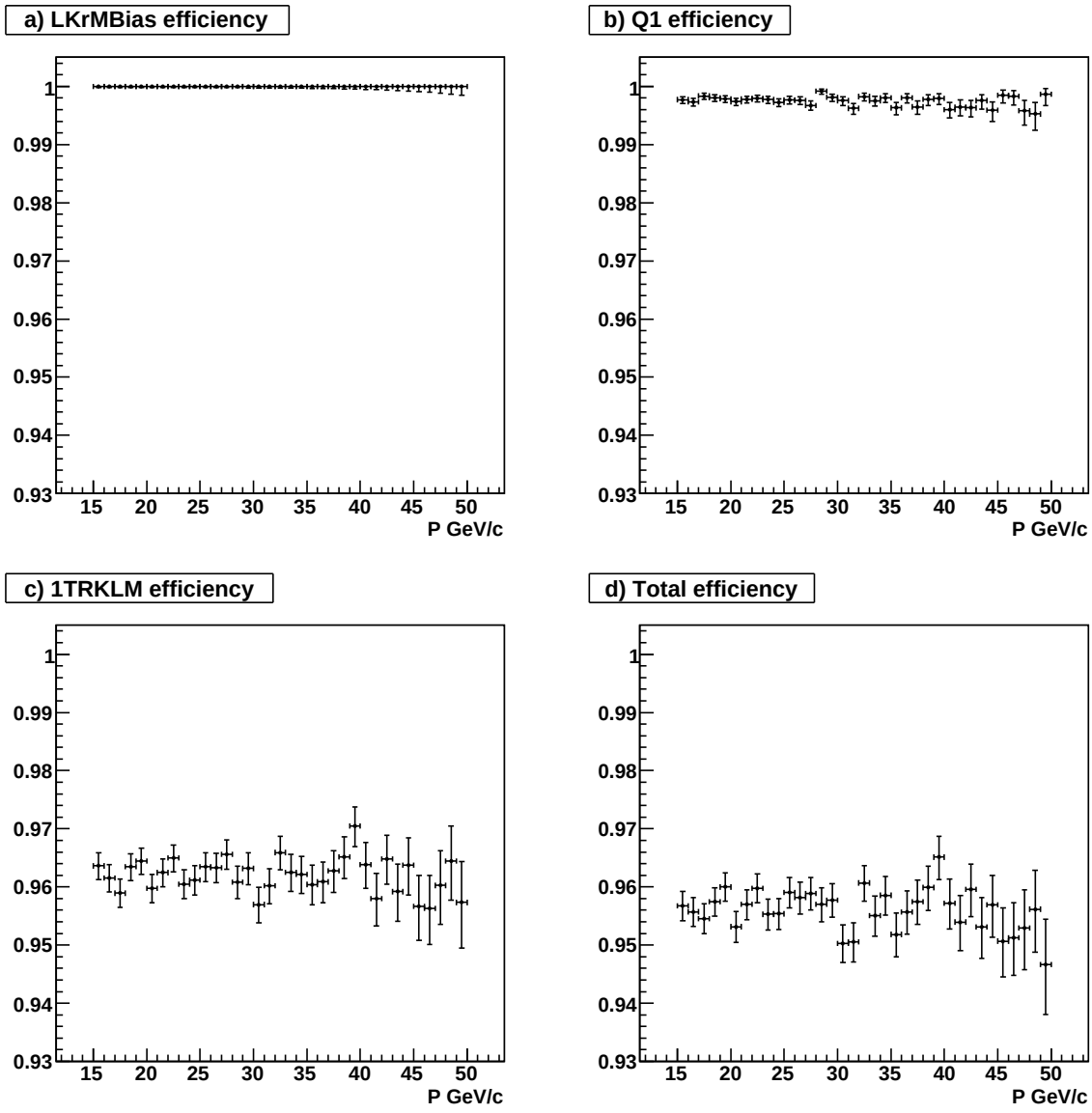

Figure 6.3: $LKrMBias \times Q1 \times 1TRKLM$ trigger efficiency as a function of track momentum: a) $LKrMBias$ component, b) Q1 component, c) 1TRKLM component and d) $LKrMBias \times Q1 \times 1TRKLM$.

charged particles of the shower can produce hits in the chambers of the spectrometer generating the 1TRKLM inefficiency. As a consequence, the measurement of the trigger efficiency in the background region gives a result which is not usable for the signal region because the signal and the main background, the Ke3 with one lost photon, have a different behaviour concerning the 1TRKLM efficiency.

To solve the problem of the trigger efficiency measurement, the following procedure has been adopted: the 1TRKLM efficiency has been assumed to be equal to 100% and only the $Q1 \times LKrMBias$ has been measured in the background region with the result $\epsilon_{e^+\nu\gamma}(Q1 \times LKrMBias) = (0.99705 \pm 0.00013)$.

The assumption of the 1TRKLM efficiency equal to 100% on Data imposes to apply another condition to the MC samples, both for signal and background, based on the number of hits in the drift chambers. This condition selects only the events with a number of hits less than 15 in all the 4 views of the 4 drift chambers. As a consequence of this other condition, the acceptance definition has been modified as:

$$A_{e^+\nu_e\gamma(SD+),bg_i}(hits) = \frac{N^{rec}_{e^+\nu_e\gamma(SD+),bg_i}(hits)}{N^{in}_{e^+\nu_e\gamma(SD+),bg_i}},$$

where $N^{rec}_{e^+\nu_e\gamma(SD+),bg_i}(hits)$ is the number of signal (background) events reconstructed at the end of the signal selection plus the hits condition, and $N^{in}_{e^+\nu_e\gamma(SD+),bg_i}$ is the initial number of signal (background) events generated with $(-1000 < Z_{gen} < 9000)$ cm. To prevent bias related to difference between the mechanism of the 1TRKLM trigger on Data and the hits condition on MC events the same condition has been applied also on the Data sample. At this point the two formulas, 6.1 and 6.2, have been modified becoming:

$$BR(K^+ \to e^+\nu_e\gamma(SD+)) = \frac{N_{e^+\nu_e\gamma(SD+)}(hits) - N_{bg}(hits)}{\Phi(K^+) \cdot A_{e^+\nu_e\gamma(SD+)}(hits) \cdot \epsilon_{e^+\nu\gamma}(Q1 \times LKrMBias)} \tag{6.3}$$

for the Branching Ratio and

$$N_{bg} = \Phi(K^+) \cdot \sum_{bg_i} BR(bg_i) \cdot A_{bg_i}(hits) \cdot \epsilon_{e^+\nu\gamma}(Q1 \times LKrMBias) \tag{6.4}$$

for the residual background.

The new values for $N_{e^+\nu_e\gamma(SD+)}(hits)$ and $A_{e^+\nu_e\gamma(SD+)}(hits)$ have been reported in table 6.3.

In figure 6.4, new results have been plotted for the trigger efficiency after the application of the procedure discussed above, the numerical values have been reported in table 6.4. Considering the results of table 6.4 and figure 6.4 c, the assumption

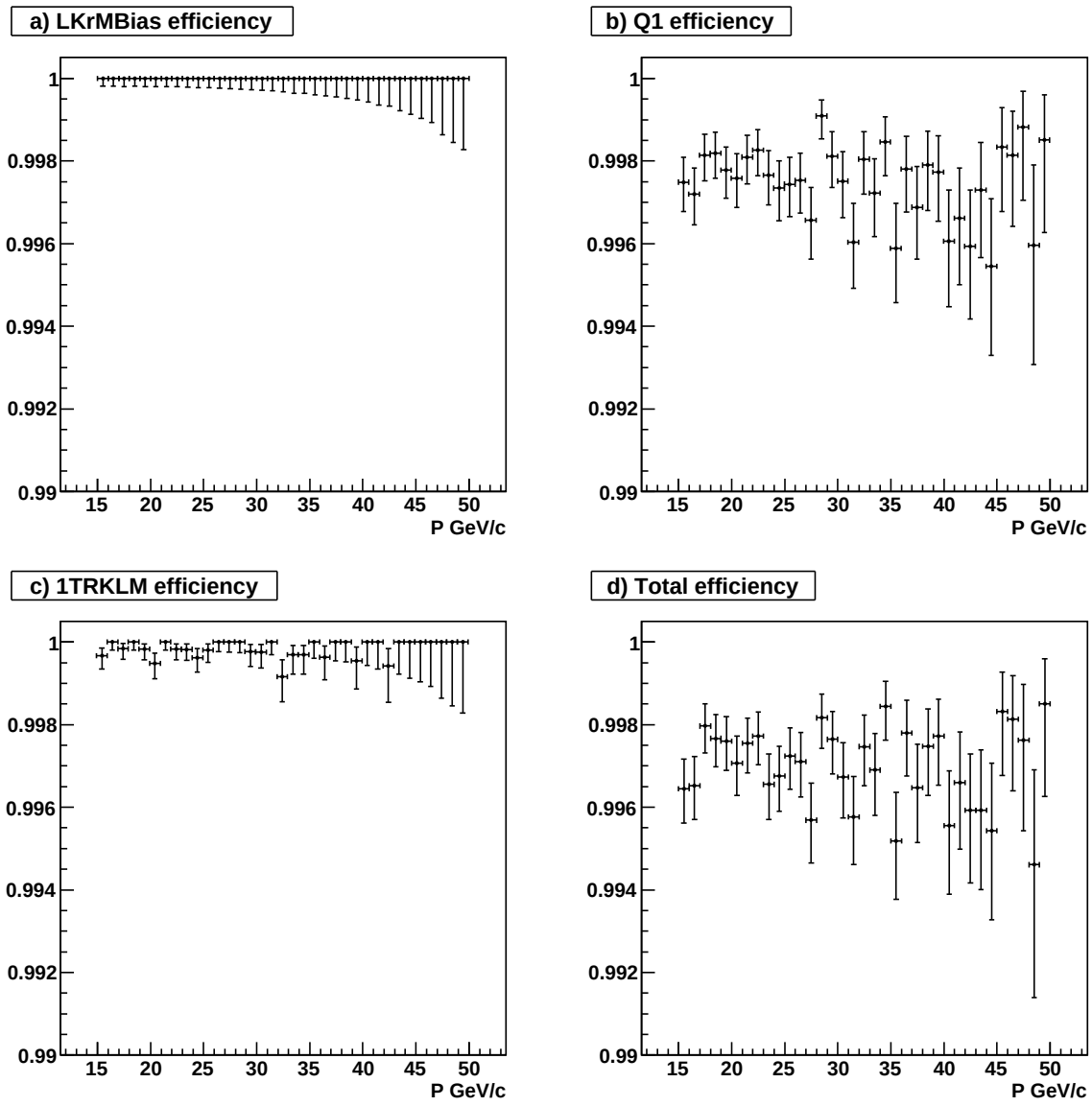

Figure 6.4: Trigger efficiency as a function of track momentum: a) $LKrMBias$ component, b) Q1 component, c) 1TRKLM component and d) $LKrMBias \times Q1$.

$N_{e^+\nu_e\gamma(SD+)}(hits)$	8230 ± 91
$A_{e^+\nu_e\gamma(SD+)}(hits)$	0.06092 ± 0.00005

Table 6.3: Number of reconstructed signal candidate and the $K^+ \to e^+\nu_e\gamma$ acceptance.

Trigger	**Efficiency**
Q1	(0.99755 ± 0.00013)
$LKrMBias$	$1.00000_{-0.00001}$
1TRKLM	(0.99982 ± 0.00004)
$Q1 \times LKrMBias$	(0.99705 ± 0.00015)

Table 6.4: Trigger efficiency results.

made for the 1TRKLM at the base of the above procedure, 100% efficiency, is correct.

6.2 Residual background

The $e^+\nu_e\gamma$ final state suffers of many background (BG) sources among which the most important are $K^+ \to e^+\pi^0\nu_e$ and $K^+ \to \pi^+\pi^0$. They both have a high Branching Ratio, compared to the signal one, and final state similar to that of the signal. The background has been studied both with MC simulations and with real Data.

For the evaluation of the acceptance in formula 6.4, the conditions related to the cluster-track association (see section 4.2) have been treated in a different way for MC channels with a charged pion or muon in the final state; the procedure applied is described in appendix A.

As it can be seen from table 6.5, where the contribution to the background evaluation has been reported for each decay channel, the main contribution comes from the $K^+ \to e^+\pi^0\nu_e$ and $K^+ \to \pi^+\pi^0$ decays. In the sum of equation 6.4 the channels for which only an upper limit could be computed have been excluded; these channels have been used, together with the others, to compute the error.

The final results for the residual background evaluation is the following:

$$N_{bg} = 235 \pm 32 \tag{6.5}$$

The total background contamination is $\sim 2.9\%$; the main contributions are shown in table 6.6, where the ratio between the background and the total number of reconstructed events has been reported.

Channel	N_{bg}
$K^+ \to e^+\pi^0\nu_e$	(141 ± 16)
$K^+ \to e^+\pi^0\nu_e Dalitz$	(4.6 ± 0.8)
$K^+ \to e^+\nu_e$	(1.98 ± 0.14)
$K^+ \to e^+\pi^0\nu_e\gamma$	< 0.26
$K^+ \to e^+\pi^0\pi^0\nu_e$	< 0.011
$K^+ \to \pi^+\pi^0$	(87 ± 23)
$K^+ \to \pi^+\pi^0\pi^0$	< 6
$K^+ \to \mu^+\nu_\mu$	< 0.00039
$K^+ \to \mu^+\nu_\mu(\mu \to e)$	< 2
$K^+ \to \mu^+\pi^0\nu_\mu$	< 0.0004
$K^+ \to \mu^+\pi^0\nu_\mu(\mu \to e)$	< 2
$K - less$	< 14

Table 6.5: Decay channels considered as background to the $K^+ \to e^+\nu\gamma(SD+)$ with the relative contribution to the background evaluation. The upper limits have been calculated at the 68% of CL.

Channel	B/S
$K^+ \to e^+\pi^0\nu_e$	$\sim 1.7 \cdot 10^{-2}$
$K^+ \to e^+\pi^0\nu_e \quad Dalitz$	$\sim 5.6 \cdot 10^{-4}$
$K^+ \to e^+\nu_e$	$\sim 2.4 \cdot 10^{-4}$
$K^+ \to \pi^+\pi^0$	$\sim 1.1 \cdot 10^{-2}$
Total	$\sim 2.9 \cdot 10^{-2}$

Table 6.6: B/S ratio.

6.3 MC/Data comparison

All the MC/Data comparisons reported in this section have been done in the following way: the Data distribution has been corrected for the trigger efficiency and each background channel has been normalized with the factor:

$$f_{bg_i} = \frac{\Phi(K^+) \cdot BR(bg_i)}{N^{in}_{bg_i}}$$

where the variables have the same meaning as in 6.4.

The MC/Data comparison has been performed at different stages of the analysis procedure, following the list of cuts, recalled below:

1. condition on the $cos(\theta^*_{e\gamma})$;

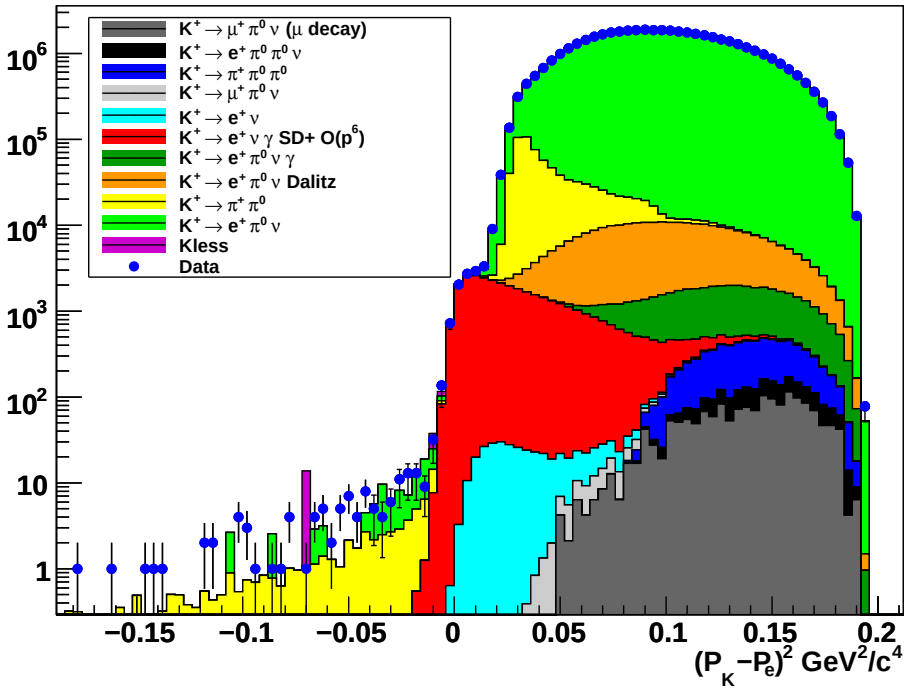

Figure 6.5: MC/Data comparison: squared missing mass before step 1.

2. condition on the 3-body squared missing mass;

3. condition on the squared missing mass;

The first comparison, see figure 6.5, has been done for the squared missing mass variable before step 1. The second comparison, shown in figure 6.6, considers the angle between the positron and the γ in the kaon rest frame; this comparison has been done again before step 1.

The third comparison, in figure 6.7, reports again the squared missing mass variable but this time after step 1. The fourth comparison, reported in figure 6.8, has been done using the squared missing transverse momentum calculated with respect to the kaon direction after step 1.

Figure 6.9 shows the fifth MC/Data comparison for the squared missing transverse momentum after step 2.

The three final comparisons, done at the end of the signal selection (after step 3), consider the 3-body squared missing mass, figure 6.10, the squared missing transverse momentum, figure 6.11, and the kinematical variable x, figure 6.12. All the MC/Data comparisons reported in this section show a good agreement, in particular in the background region.

A problem is visible in the ratio between the MC squared missing mass distribu-

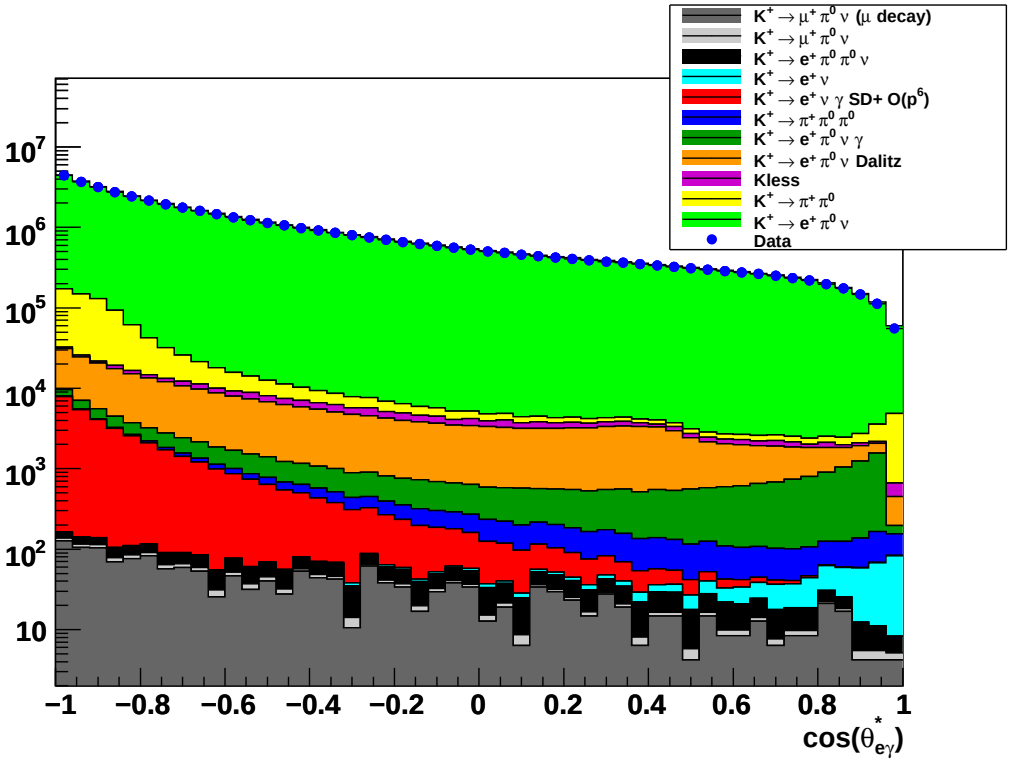

Figure 6.6: MC/Data comparison: angle between the positron and the photon in the kaon rest frame before step 1.

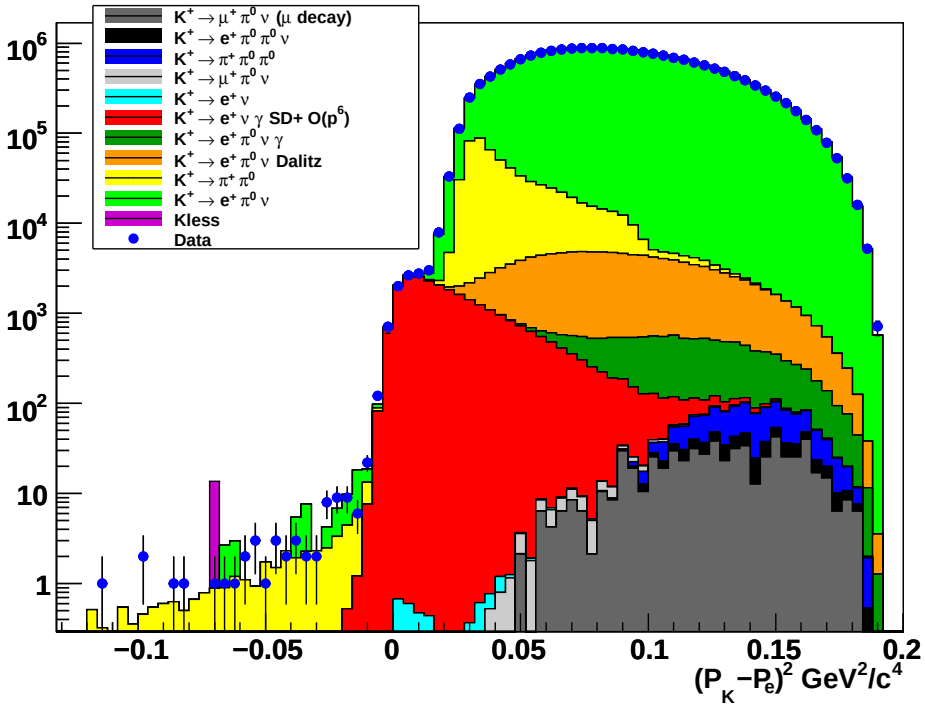

Figure 6.7: MC/Data comparison: squared missing mass after step 1.

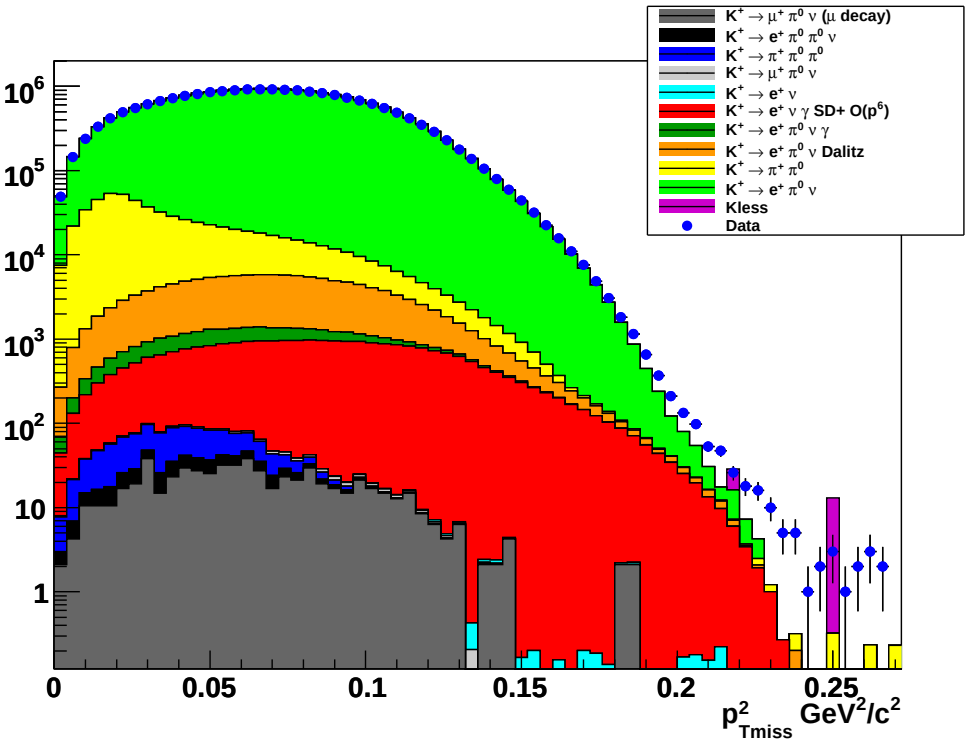

Figure 6.8: MC/Data comparison: p^2_{Tmiss} after step 1.

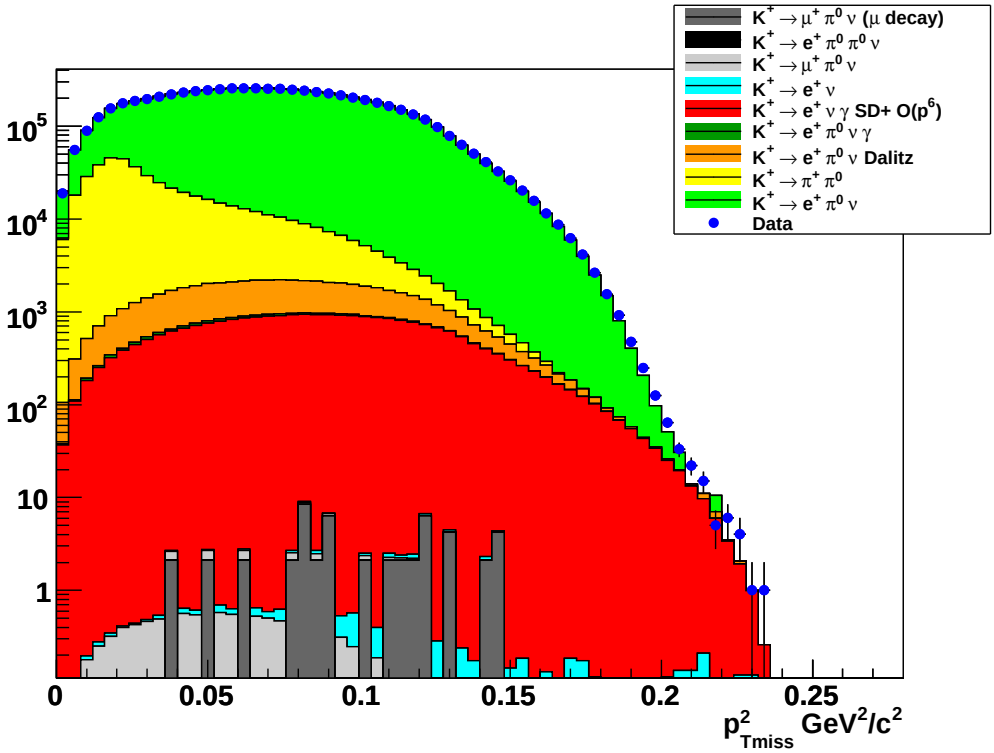

Figure 6.9: MC/Data comparison: p^2_{Tmiss} after step 2.

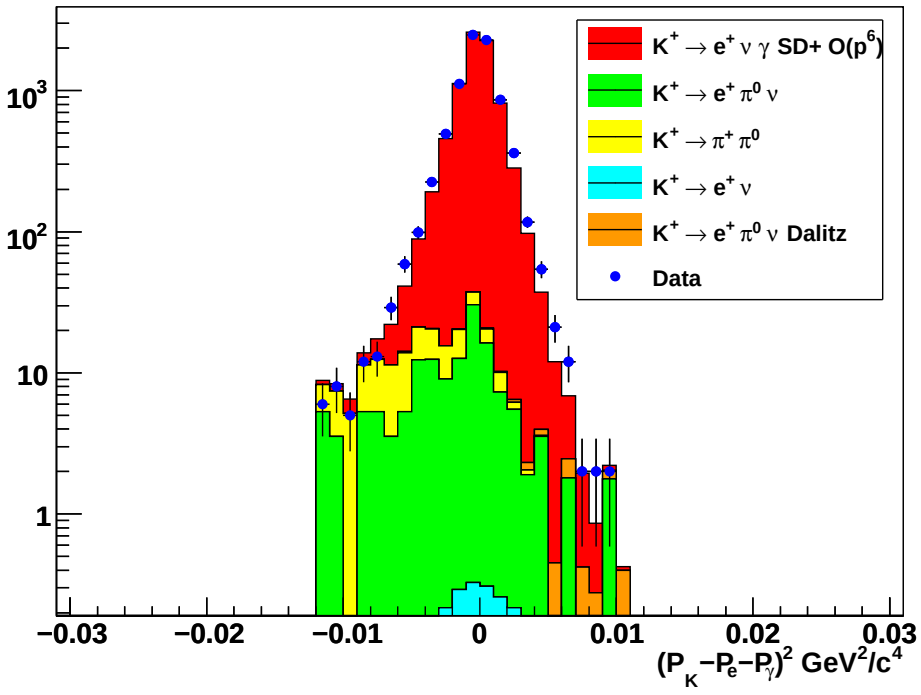

Figure 6.10: MC/Data comparison: 3-body squared missing mass after step 3.

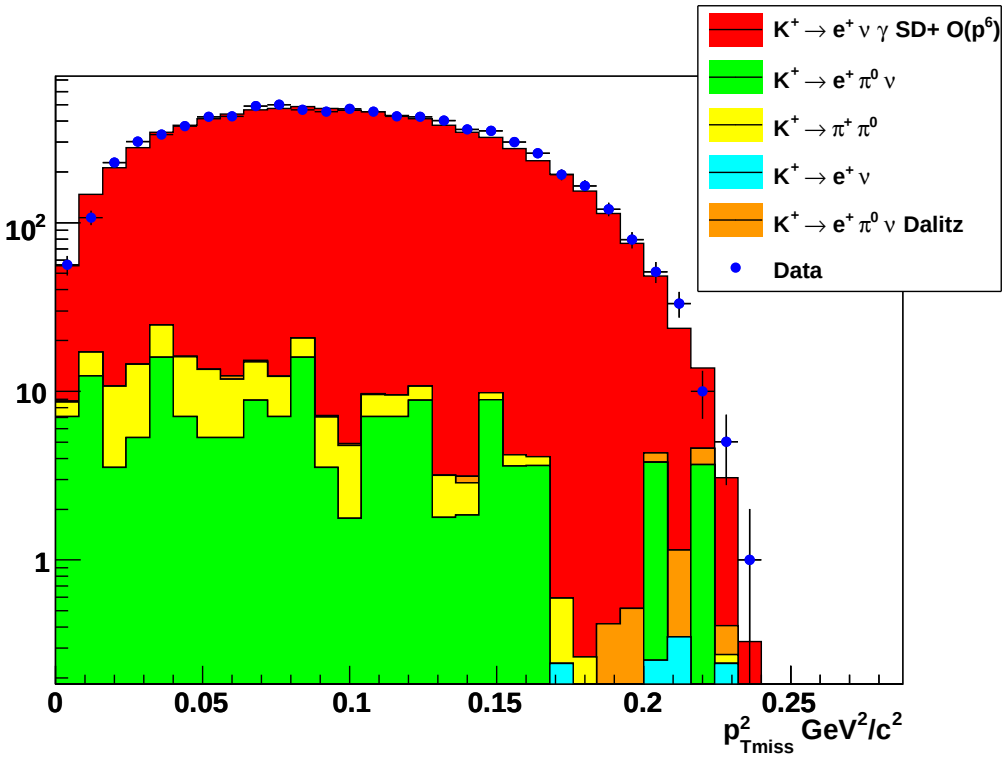

Figure 6.11: MC/Data comparison: p^2_{Tmiss} after step 3.

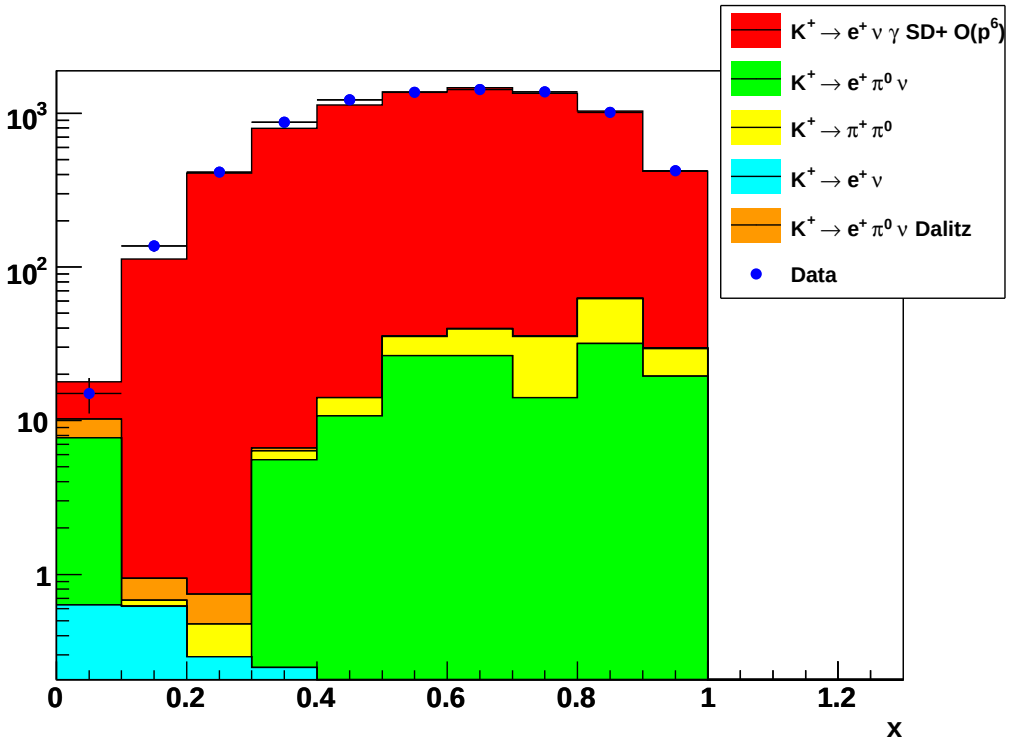

Figure 6.12: MC/Data comparison: the x variable after step 3.

tion and the Data one reported in figure 6.13 . This ratio has been obtained after step 1, the same point of the figure 6.7. As it can be seen from the figure in the region around 0.03 GeV^2/c^4, there is a hole due to a not perfect rejection of the $K^+ \to \pi^+\pi^0$ decay. Infact as it can be seen from the comparison reported in figure 6.7, that is the region of the $\pi^+\pi^0$ peak (yellow distribution).

6.4 The Branching Ratio measurement

All the quantities necessary to evaluate the $K^+ \to e^+\nu_e\gamma$ (SD+) Branching Ratio from the formula 6.3 are summarized in table 6.7.

Using the values listed in the table, the result for the Branching Ratio is:

$$BR(K^+ \to e^+\nu_e\gamma(SD+)) = (1.549 \pm 0.018_{stat} \pm 0.013_{sys^*} \pm 0.031_{sys}) \cdot 10^{-5}, \quad (6.6)$$

where the ΔBR_{stat} uncertainty takes into account the $K^+ \to e^+\nu_e\gamma$ statistic, ΔBR_{sys^*} is the first part of the systematic uncertainty that takes into account the errors on the acceptance correction, background evaluation, trigger efficiency and flux measurement, and ΔBR_{sys} is the second part of the systematic uncertainty described in the following sections. Figure 6.14 shows the ratio between the Data (background

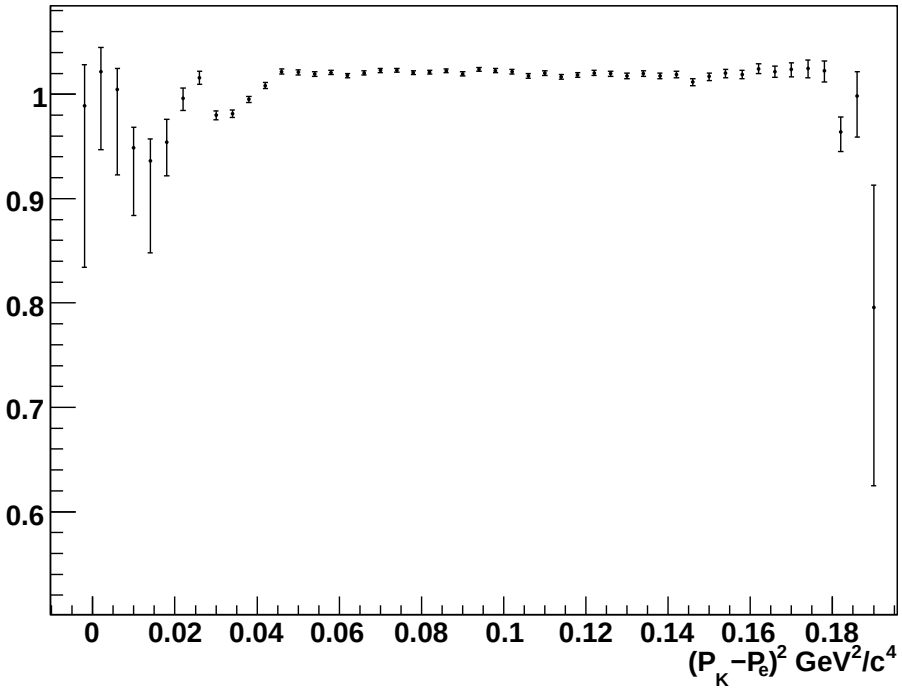

Figure 6.13: MC/Data squared missing mass ratio.

	Value
$N_{e^+\nu_e\gamma(SD+)}(hits)$	8230 ± 91
$N_{bg}(hits)$	235 ± 32
$\Phi(K^+)$	$(8.50 \pm 0.07) \cdot 10^9$
$A_{e^+\nu_e\gamma(SD+)}(hits)$	0.06092 ± 0.00005
$\epsilon_{e^+\nu\gamma}(Q1 \times LKrMBias)$	(0.99705 ± 0.00013)

Table 6.7: Summary of all the quantities necessary for the Branching Ratio measurement.

subtracted) and the MC simulation of the signal based on the ChPT at $O(p^6)$. The linear fit to the ratio shows a good agreement with a constant, this is a first evidence of a non negligible $O(p^6)$ contribution to the $K^+ \to e^+\nu_e\gamma$ form factors.

6.4.1 Comparison with the different theoretical models

The result reported in 6.6 is obtained using a signal MC simulation based on the ChPT at $O(p^6)$. The peculiarity of this model is to predict a linear dependence of the form factors (F_V and F_A) with respect to the kinematical variable x (see section 1.3.1). The ChPT, at $O(p^4)$, predicts a constant value for the form factors. If a MC based on the ChPT at $O(p^4)$ is used, the following value for the Branching Ratio is

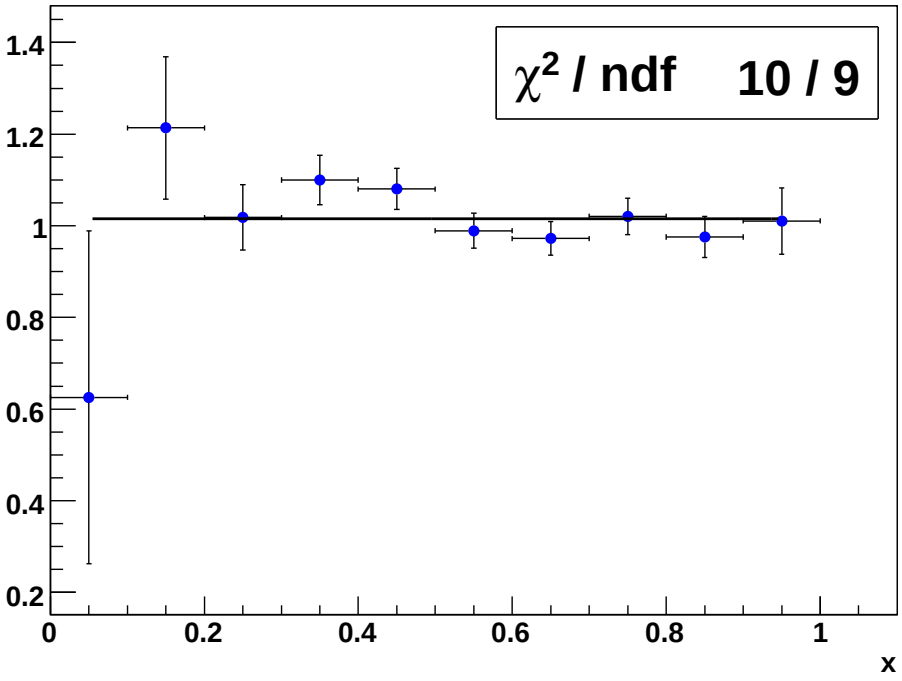

Figure 6.14: Ratio between the Data (background subtracted) and the MC simulation of the signal based on the ChPT at $O(p^6)$.

obtained:

$$BR(K^+ \to e^+\nu_e\gamma(SD+)) = (1.585 \pm 0.018_{stat} \pm 0.013_{sys^*} \pm 0.032_{sys}) \cdot 10^{-5} \quad (6.7)$$

with the same meaning for the two error contribution as in 6.6 and the second systematic contribution corresponds to the same amount ($\sim 2\%$) of 6.6. The difference between the two results, 6.6 and 6.7, is due to a different acceptance, which, computed using the ChPT model at $O(p^4)$ MC simulation is:

$$A_{e^+\nu_e\gamma(SD+)}(hits) = 0.05952 \pm 0.00003$$

The MC/Data comparison reported in figure 6.15 shows an agreement worse than the comparison reported in figure 6.12, obtained with signal MC simulation based on ChPT at $O(p^6)$. The ratio between the Data (background subtracted) and the MC simulation of the signal based on the ChPT at $O(p^4)$ has been reported in figure 6.16. The incompatibility of the linear fit with a constant is a second and more clear evidence of the $O(p^6)$ contribution to the $K^+ \to e^+\nu_e\gamma$ form factors.

Using the signal MC simulation based on the ChPT at $O(p^6)$ model with the form factors measured by the KLOE collaboration [28], the measurement of the

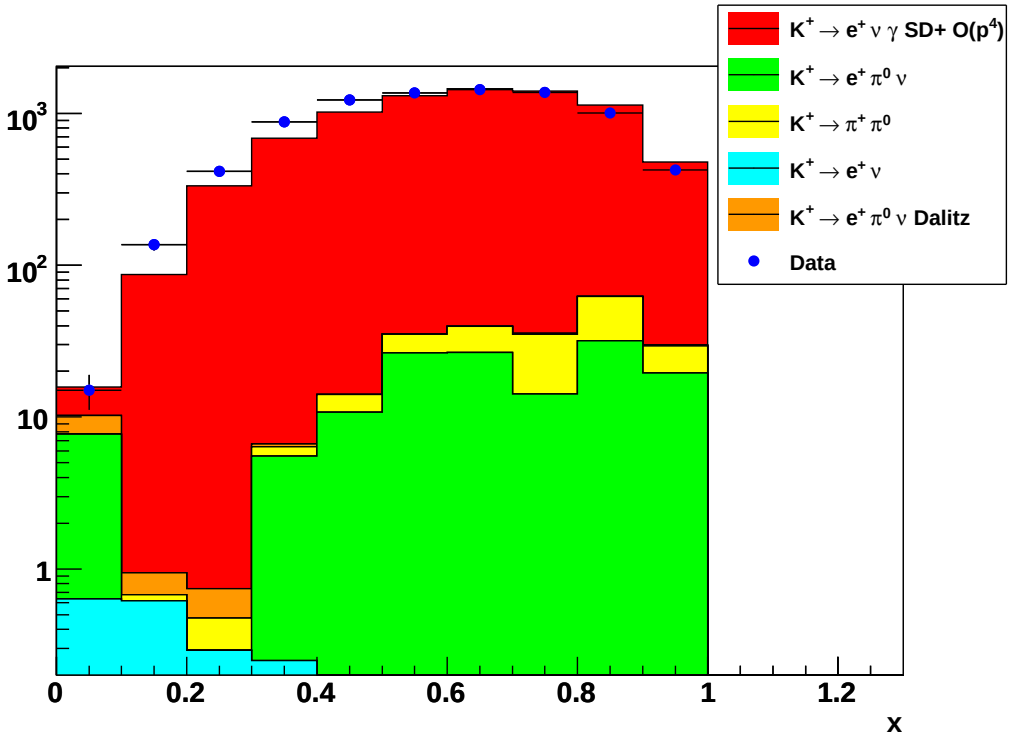

Figure 6.15: MC/Data comparison: the x variable at the end of signal selection.

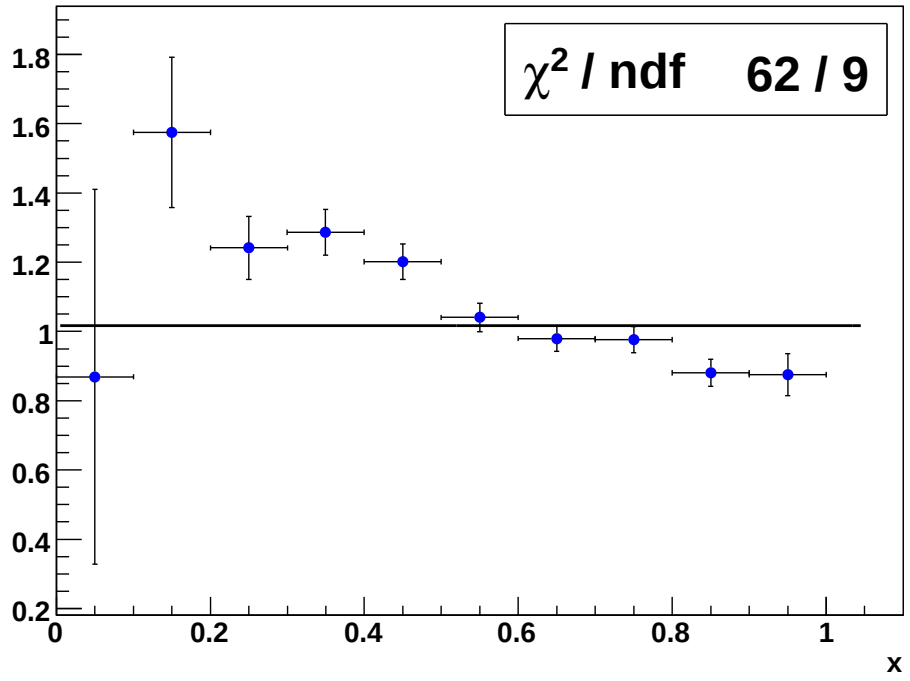

Figure 6.16: Ratio between the Data (background subtracted) and the MC simulation of the signal based on the ChPT at $O(p^4)$.

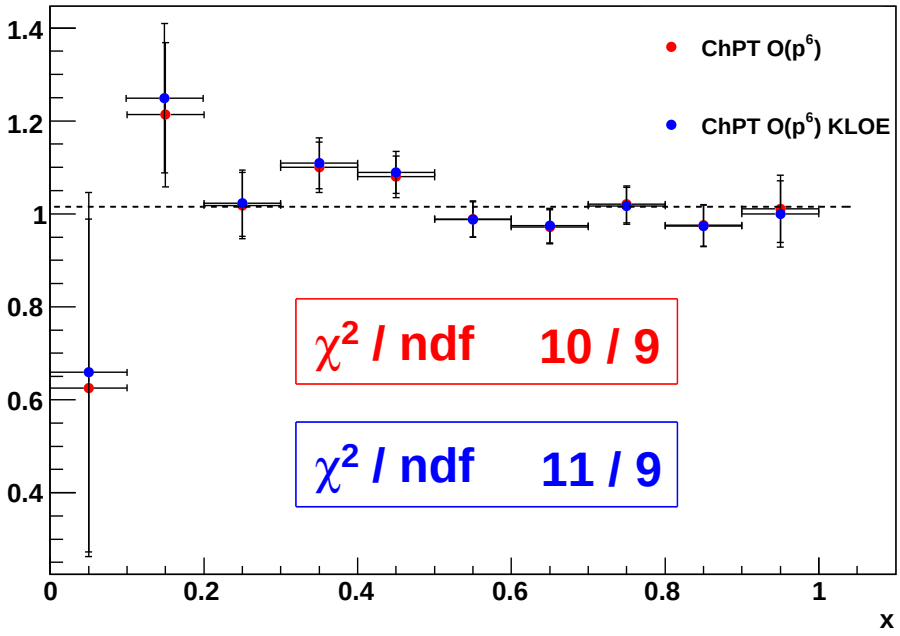

Figure 6.17: Ratio between the Data (background subtracted) and the MC simulation of the signal based on the ChPT at $O(p^6)$ with the form factors measured by KLOE in comparison with the ratio obtained using the form factors prediction of ChPT at $O(p^6)$.

$K^+ \to e^+\nu_e\gamma$ (SD+) Branching Ratio is:

$$BR(K^+ \to e^+\nu_e\gamma(SD+)) = (1.551 \pm 0.018_{stat} \pm 0.013_{sys^*}) \cdot 10^{-5}, \tag{6.8}$$

in perfect agreement with the result reported in equation 6.6. Figure 6.17 shows the ratio between the Data (background subtracted) and the MC simulation of the signal based on the ChPT at $O(p^6)$ with the form factors measured by KLOE in comparison with the ratio obtained using the form factors prediction of ChPT at $O(p^6)$. The two ratios are in perfect agreement.

Figure 6.18 reports the MC/Data comparison done using the signal MC simulation based on the LFQM. This theoretical model predicts a non trivial dependence of the two form factors on the x variable (see section 1.3.1). From the figure the MC/Data disagreement is a clear indication that the LFQM is not able to reproduce the Data shape of the distribution, as observed also by the KLOE collaboration [28].

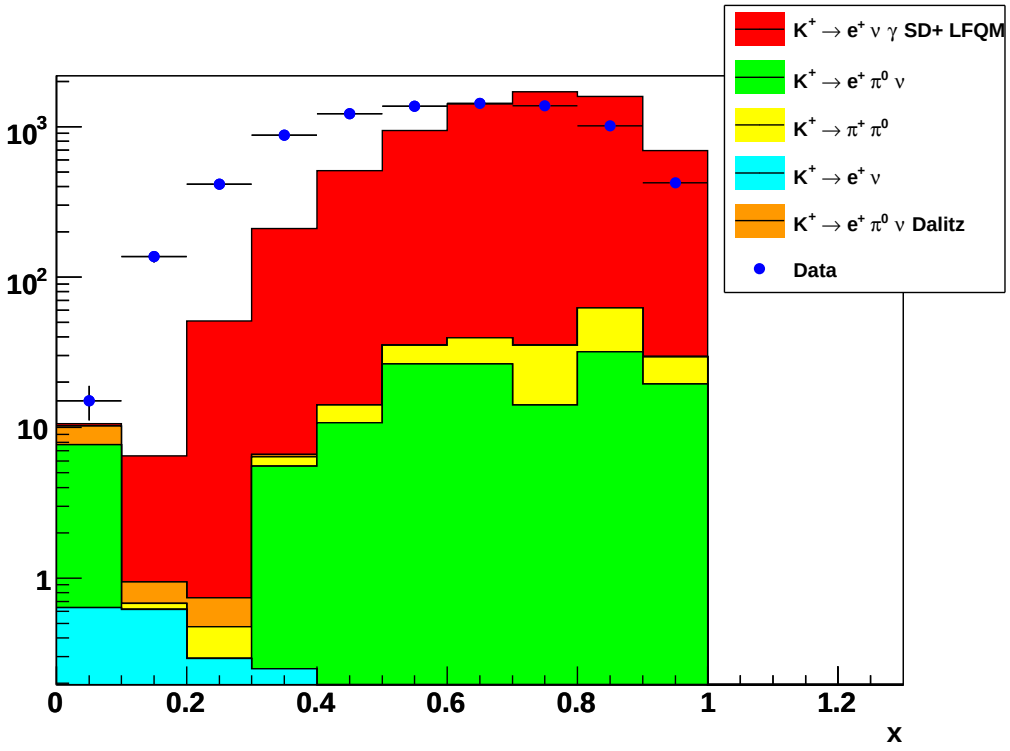

Figure 6.18: MC/Data comparison: the x variable at the end of the signal selection.

6.4.2 The Branching Ratio as a function of the x

To perform a model independent measurement of the $K^+ \to e^+\nu_e\gamma$ (SD+) Branching Ratio, it is useful to measure the BR as a function of the x variable. Using the MC simulation based on ChPT at $O(p^6)$ model, the value of the Branching Ratio in a given bin of x is:

$$BR(K^+ \to e^+\nu_e\gamma(SD+))_i = \frac{N_{e^+\nu_e\gamma(SD+)}(hits)_i - N_{bg}(hits)_i}{\Phi(K^+) \cdot A_{e^+\nu_e\gamma(SD+)}(hits)_i \cdot \epsilon_{e^+\nu\gamma}(Q1 \times LKrMBias)}, \quad (6.9)$$

where $N_{e^+\nu_e\gamma(SD+)}(hits)_i$ is the number of events reconstructed at the end of the signal selection in the bin i, $N_{bg}(hits)_i$ is the total background in bin i, $\Phi(K^+)$ is the kaon flux, $A_{e^+\nu_e\gamma(SD+)}(hits)_i$ is the signal acceptance in bin i, and $\epsilon_{e^+\nu\gamma}(Q1 \times LKrMBias)$ is the trigger efficiency.

The signal acceptance for each bin, $A_{e^+\nu_e\gamma(SD+)}(hits)_i$, is defined as the ratio between the number of reconstructed MC events in the bin i (generated in the same bin) and the number of generated events in the bin i with $(-1000 < Z_{gen} < 9000)$ cm. For the denominator, the bin is chosen considering the generated x. The Data has been then corrected for the bin to bin migration probability. This probability

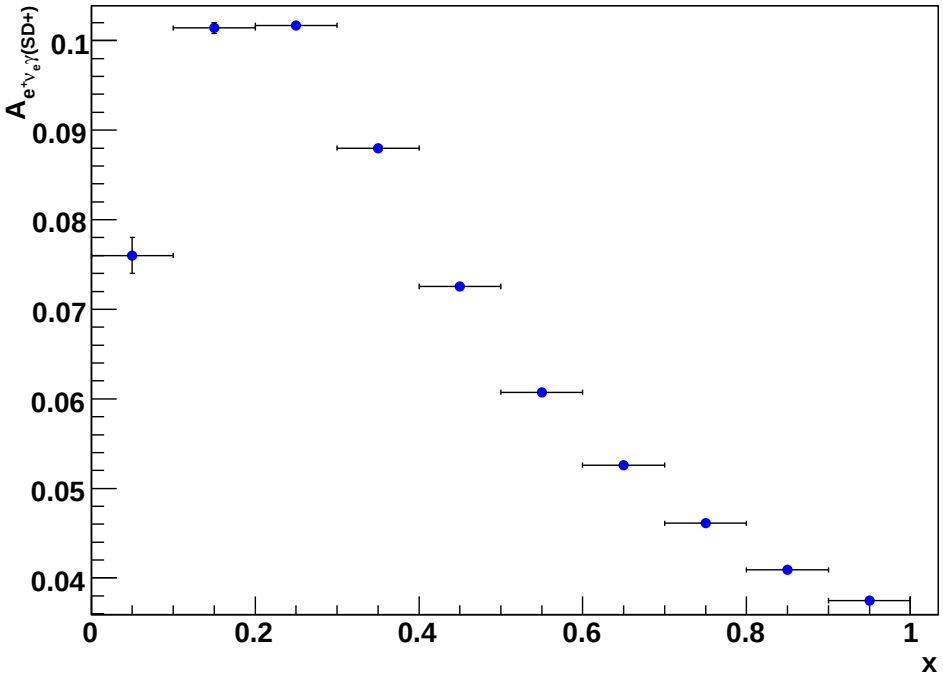

Figure 6.19: Signal acceptance as a function of x.

has been measured according the followinf formula:

$$P(i,j) = \frac{\sum_{j \neq i} N_{i,j}}{N_i}$$

where $N_{i,j}$ is the number of events generated in bin i and reconstructed in bin j and passing all the signal selection and N_i is the total number of events generated in bin i and passing the signal selection.

Figure 6.19 shows the signal acceptance as a function of x and figure 6.20 shows the bin to bin migration probability used to correct the Data distribution. To prove the model independent assumption in figure 6.21 has been reported the comparison between the acceptance as a function of x for a MC simulation based on ChPT at $O(p^4)$ model and for a MC simulation based on ChPT $O(p^6)$ model. Apart a small discrepancy (order of percent) in the two first bins, the two acceptances are practically the same, confirming that the x dependent measurement is model independent. The numerical results of the differential Branching Ratio as a function of the x are reported in table 6.8 and the plot is reported in figure 6.22.

The result obtained integrating the differential Branching Ratio of table 6.8 is:

$$BR(K^+ \to e^+\nu_e\gamma(SD+)) = (1.54 \pm 0.07) \cdot 10^{-5} \tag{6.10}$$

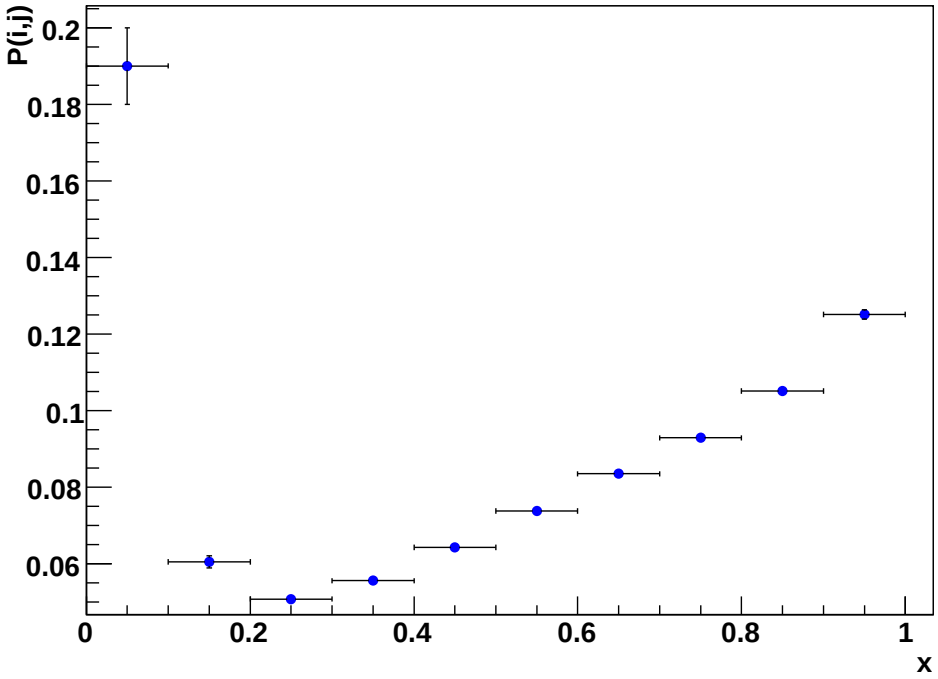

Figure 6.20: Bin to bin migration probability.

x	$\frac{dBR}{dx}$ (10^{-5})	$\Delta(\frac{dBR}{dx})$ (10^{-5})
$0 \leq x < 0.1$	0.01	0.03
$0.1 \leq x < 0.2$	0.15	0.02
$0.2 \leq x < 0.3$	0.45	0.03
$0.3 \leq x < 0.4$	1.10	0.05
$0.4 \leq x < 0.5$	1.84	0.07
$0.5 \leq x < 0.6$	2.38	0.09
$0.6 \leq x < 0.7$	2.80	0.10
$0.7 \leq x < 0.8$	3.10	0.11
$0.8 \leq x < 0.9$	2.43	0.12
$0.9 \leq x < 1$	1.08	0.09

Table 6.8: $\frac{dBR}{dx}$, results and relative errors

This result is in perfect agreement with that of 6.6 confirming again that the nature prefers non negligible contribution of the $O(p^6)$ term for the ChPT description of the $K^+ \to e^+\nu_e\gamma$ form factors.

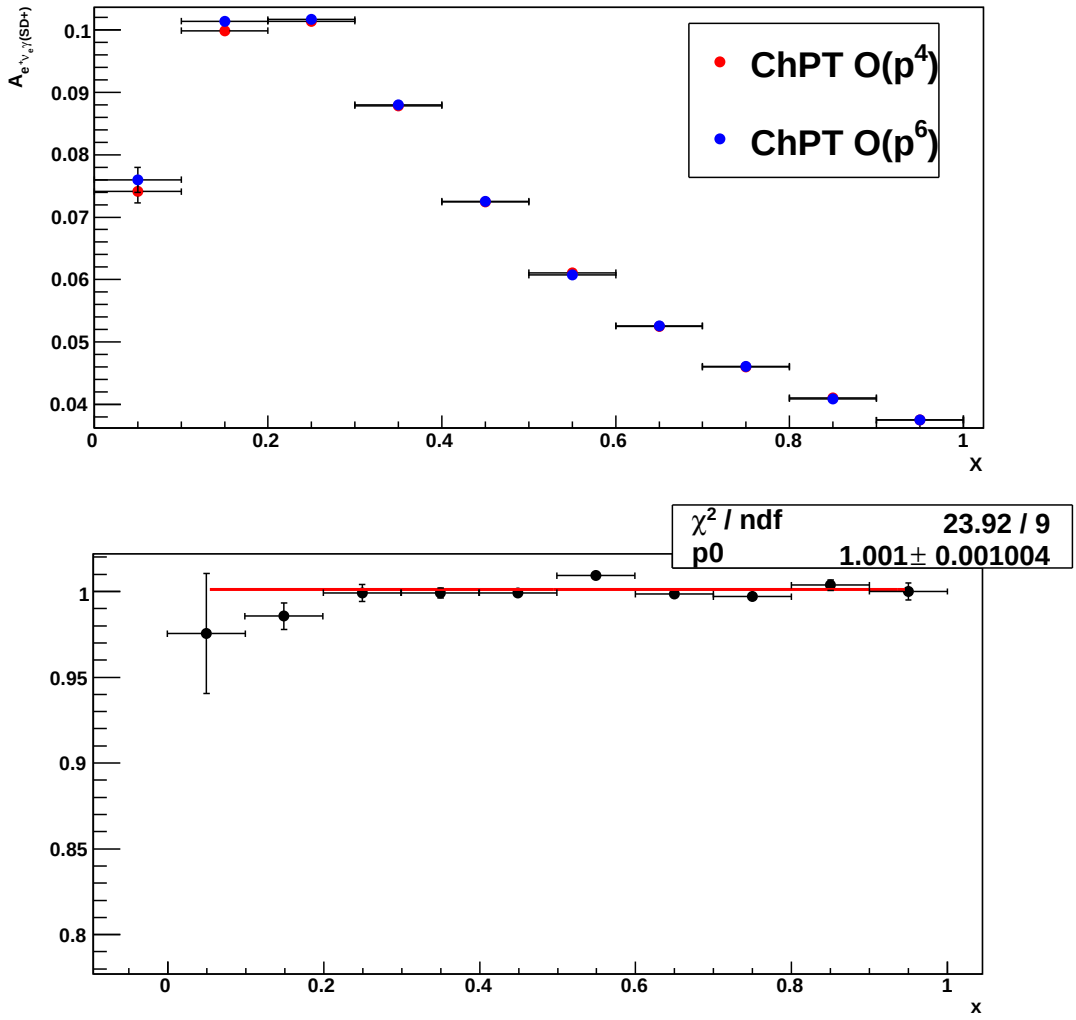

Figure 6.21: Comparison of the acceptances measured with the MC simulation based on the two different ChPT models (up) and the ratio between the two acceptances (down).

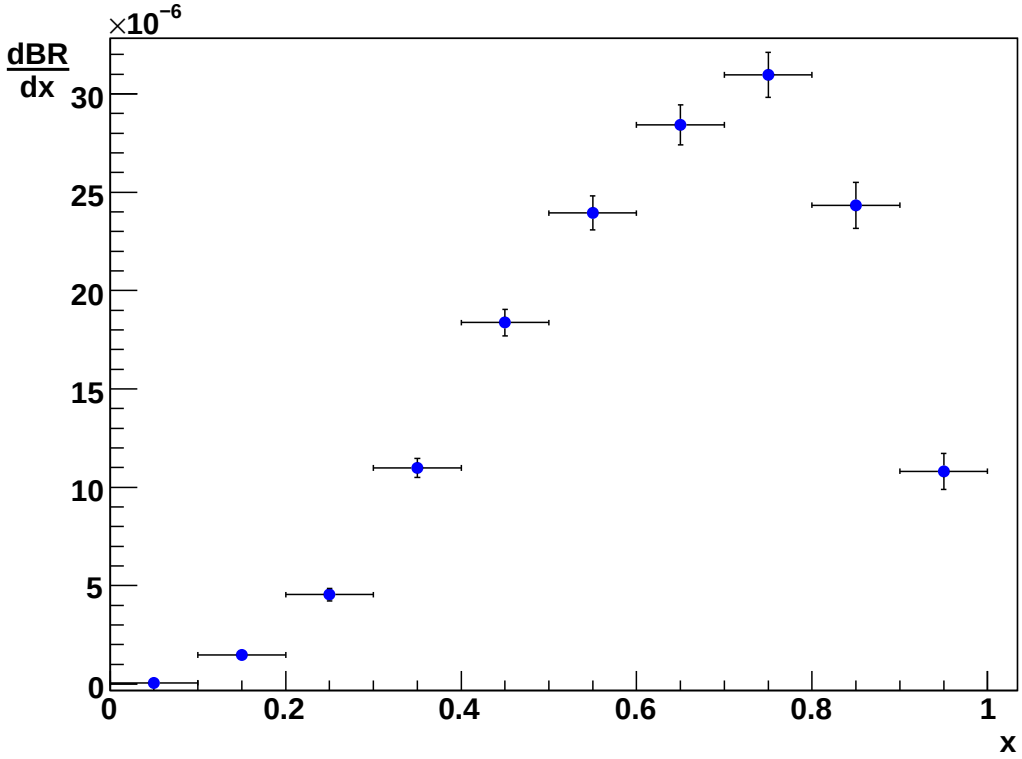

Figure 6.22: Differential Branching Ratio as a function of x.

6.4.3 Comparison with the present experimental status

As pointed out in the first chapter, the value of the Branching Ratio published in the PDG [14], $BR(K^+ \to e^+\nu_e\gamma(SD^+)) = (1.53 \pm 0.23) \cdot 10^{-5}$ with an accuracy of $\sim 15\%$, has been obtained considering constant form factors, as predicted in the ChPT at $O(p^4)$ model. To perform a correct comparison with the PDG value, the Branching Ratio obtained with the signal MC simulation based on ChPT at $O(p^4)$ has been used. In addition a cut at $x > 0.2$ ($E^*_\gamma >\sim 48MeV$) in the x distribution, has been applied. With this condition the Branching Ratio is:

$$BR(K^+ \to e^+\nu_e\gamma(SD+)) = (1.576 \pm 0.039) \cdot 10^{-5}$$

in agreement, within the errors, with the PDG value.

The recent KLOE result of the Branching Ratio based on ChPT at $O(p^6)$ is:

$$BR(K^+ \to e^+\nu_e\gamma(SD+)) = (1.409 \pm 0.065) \cdot 10^{-5}$$

with an accuracy of $\sim 4.5\%$. The result obtained in this work, 6.6 is:

$$BR(K^+ \to e^+\nu_e\gamma(SD+)) = (1.549 \pm 0.038) \cdot 10^{-5},$$

with an accuracy of $\sim 2.5\%$. The two results are in agreement within $\sim 2\sigma$.

6.5 Stability checks

In order to understand the stability of the Branching Ratio measurement with respect to critical points of the analysis several checks have been performed. When a variation of the BR value is found, it is taken into account in the systematic uncertainty computation.

The error associated to a given check has been estimated assuming uncorrelated uncertainties. The uncorrelated error on the Branching Ratio value obtained for the i^{th} cut variation has been evaluated with respect to the reference one as:

$$\sigma^2_{i,uncorrelated} = |\sigma^2_{reference} - \sigma^2_i| \tag{6.11}$$

where both $\sigma_{reference}$ and σ_i take into account the $K^+ \to e^+\nu_e\gamma$ total error that includes the statistical one and the uncertainties on the acceptance correction, background estimation, trigger efficiency and flux measurements.
The reference value is the result reported in 6.6.

6.5.1 Squared missing mass cut

The first check is performed on the squared missing mass, $(P_K - P_e)^2$, cut. The BR has been measured assuming different values of the upper cut; the result of this procedure is reported in figure 6.23. When the cut is moved above 0.015 GeV^2/c^4 there is a large increase of the B/S ratio, mostly due to the Ke3 contribution, as it can be seen from figure 6.24 where the B/S ratio is shown. As a consequence of this, a restricted region, below 0.015 GeV^2/c^4, has been considered for the check. The contribution to the systematic uncertainity coming from this cut, has been evaluated as the half difference between the point at 0.014 GeV^2/c^4 and the one at 0.006 GeV^2/c^4; it amounts to $\sim 2.2 \cdot 10^{-7}$ ($\sim 1.4\%$ of the BR).

6.5.2 Track momentum cut

The second check takes into account the condition applied to the track momentum. Figure 6.25 shows the variation of the BR measurement as a function of the momen-

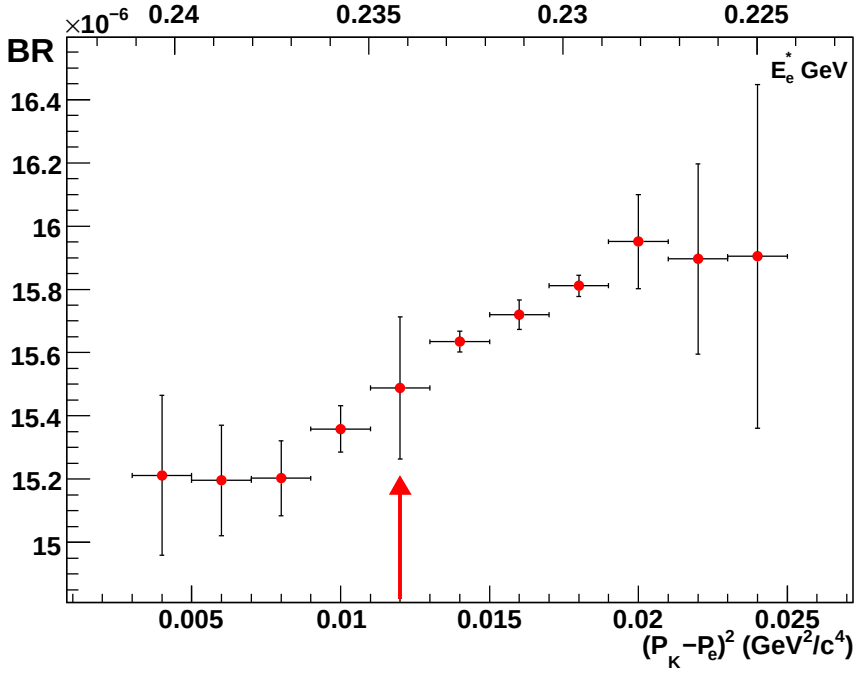

Figure 6.23: Branching Ratio value as a function of the squared missing mas cut. The red arrow shows the reference value. The upper axis reports the corresponding value of the positron energy in the kaon rest frame.

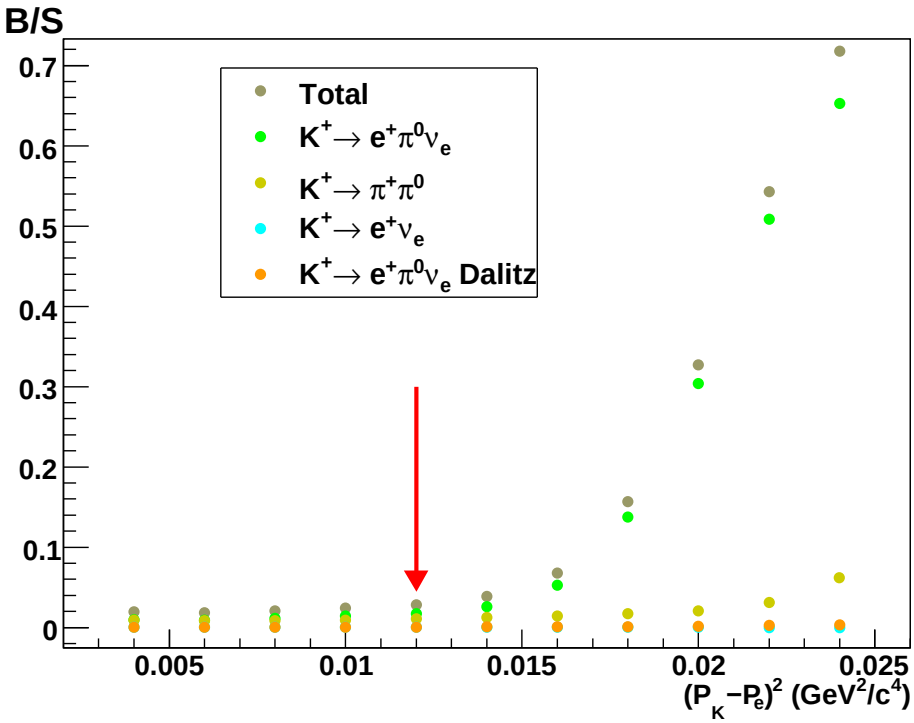

Figure 6.24: B/S ratio as a function of the squared missing mas cut. The red arrow shows the reference value.

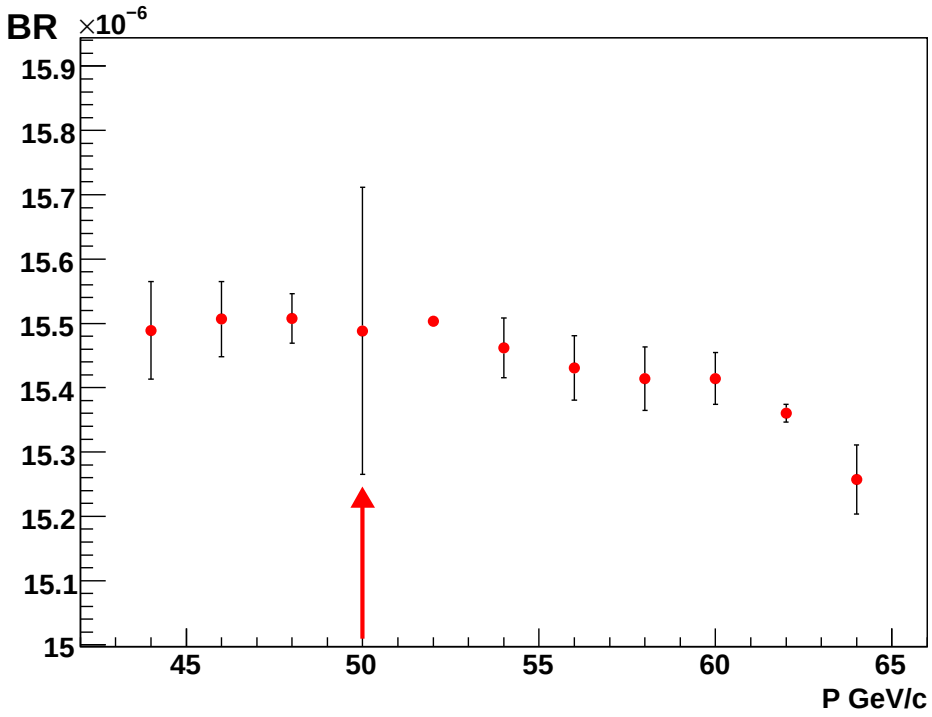

Figure 6.25: Branching Ratio value as a function of the track momentum cut. The red arrow shows the reference value.

tum upper cut. For track momentum value above 56 GeV/c there is a significant increase of the background mostly due to the $K^+ \to \pi^+\pi^0$ contribution as it can be seen from figure 6.26 where the ratio B/S is shown. For this reason the stability of the measurement is checked only for values of the cut below 56 GeV/c. In this region the discrepancy between the BR measurements are inside one uncorrelated σ and then no contribution to the systematic uncertainty is added.

6.5.3 Photon energy cut

The BR stability has been checked as a function of the condition applied to the energy of the cluster associated to the radiative photon, the variation is shown in figure 6.27. A value of 7 GeV has been choosen as upper limit for the check, in order to not introduce modification in the photon energy spectrum in the kaon rest frame resulting in a physical variation of the BR due to the restricted kinematical interval of the measurement. In figure 6.28 the scatter plot between the photon energy and the x variable is shown. The stability of the BR has been checked using all the range of checked values of the cut considering that the B/S ratio is practically stable, as it can be seen from the ratio B/S shown in figure 6.29. A variation of $\sim 4.6 \cdot 10^{-8}$

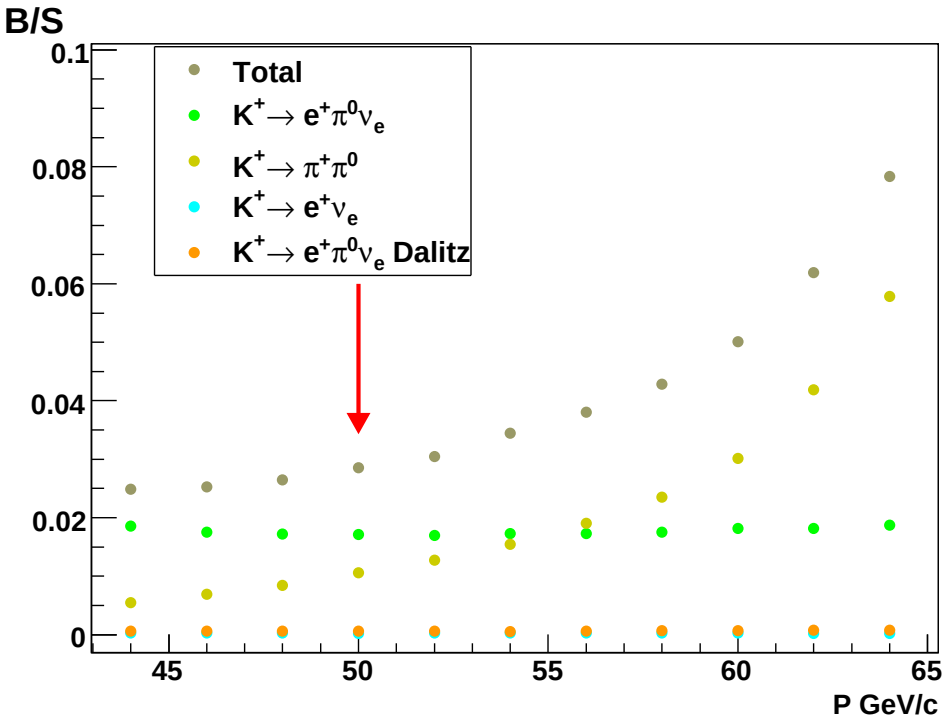

Figure 6.26: B/S ratio as a function of the track momentum cut. The red arrow shows the reference value.

($\sim 0.3\%$ of the BR) has been found between the point at 3 GeV and the last point at 7 GeV. The half difference, $\sim 2 \cdot 10^{-8}$, has been added to the systematic uncertainty.

6.5.4 Charged vertex condition

The check considers the stability of the measurement as a function of the charged vertex cut. Figure 6.30 shows the BR value as a function of the lower cut (left) and of the upper cut (right) variation. The B/S ratio has been reported in figure 6.31. The half discrepancy, $\sim 6 \cdot 10^{-8}$ ($\sim 0.4\%$ of the BR), observed in the left plot of figure 6.30, has been added to the systematic uncertainity.

6.5.5 Timing cuts

A crucial point of the analysis are the timing cuts due to the fact that the time measurements is not in the MC. Figure 6.32, shows the distribution of the difference between the time of the electromagnetic cluster associated to the charged track, measured with the calorimeter, and the hodoscope time of the charged track, $\Delta T(Lkr - Hodo)$, for Data events passing all the Ke3 selection cuts (top) and all

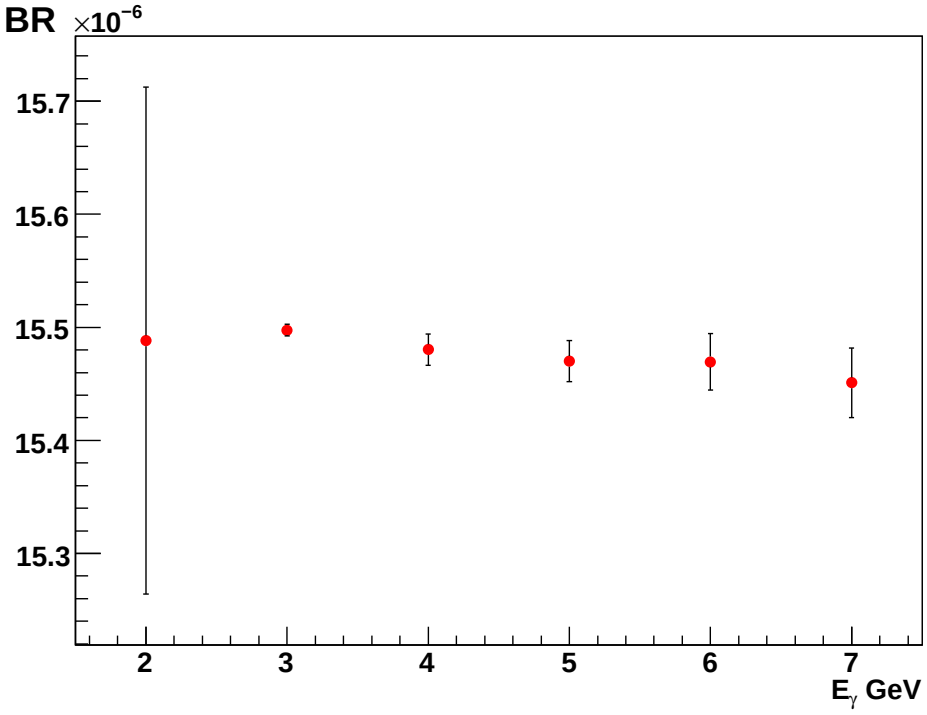

Figure 6.27: Branching Ratio value as a function of the energy of the cluster associated to the radiative photon cut.

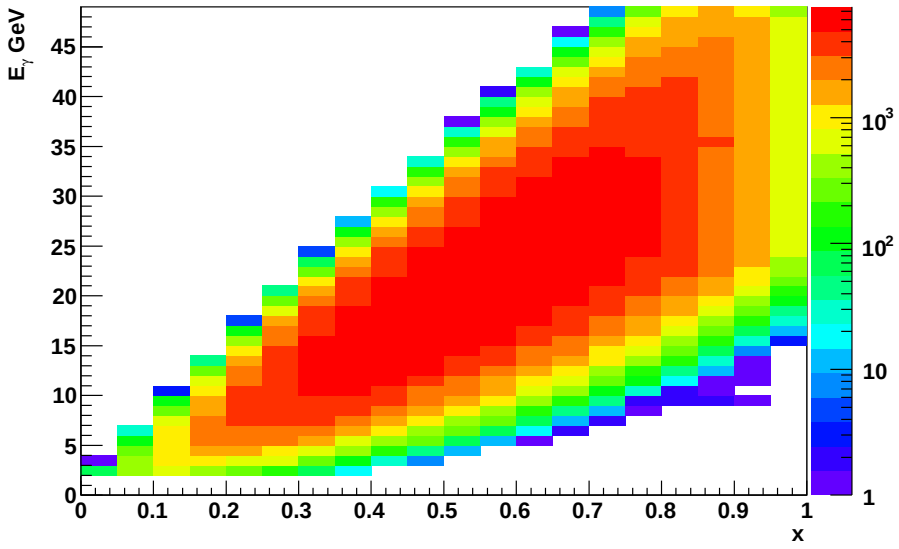

Figure 6.28: Scatter plot between the photon energy and the x variable for $K^+ \to e^+\nu_e\gamma$ (SD+) MC events.

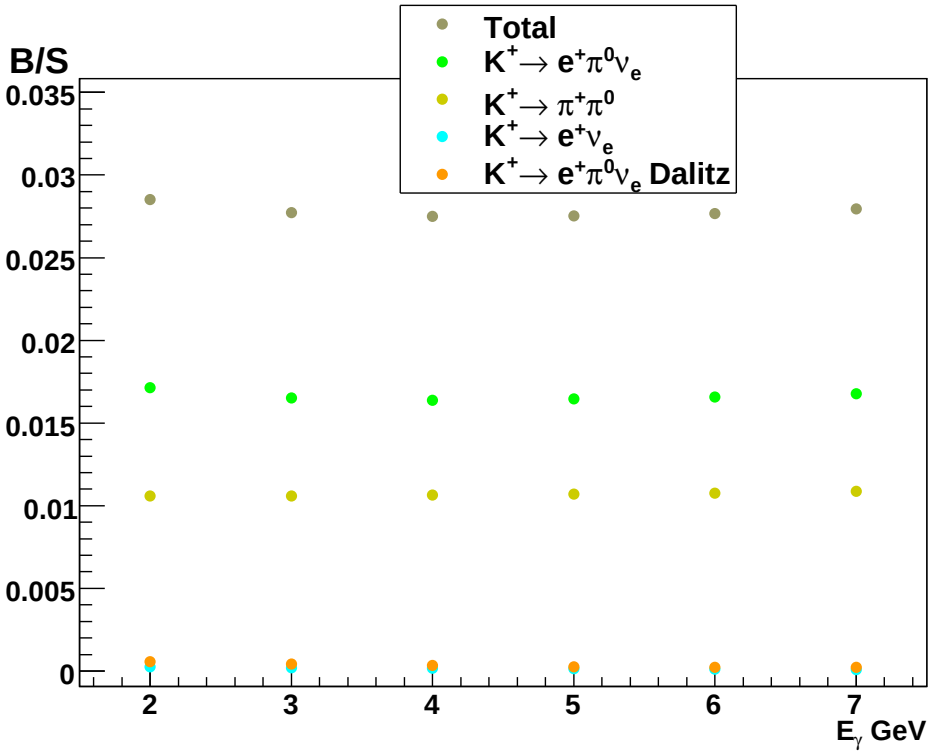

Figure 6.29: B/S ratio as a function of the energy of the cluster associated to the radiative photon cut.

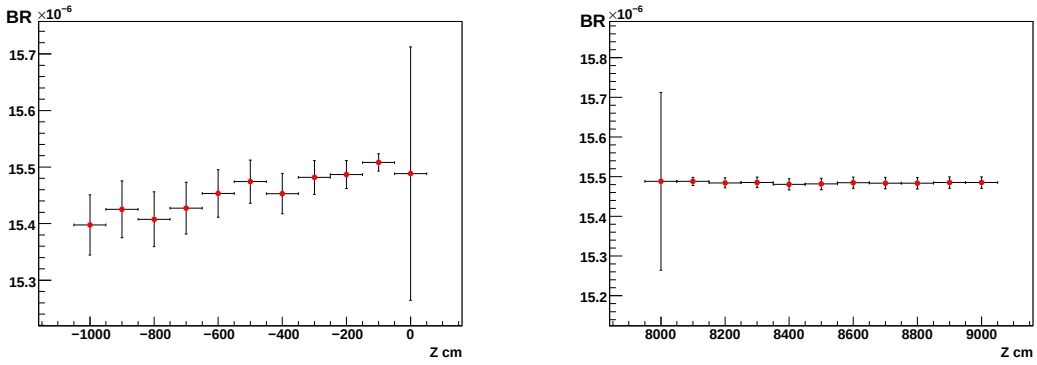

Figure 6.30: Branching Ratio value as a function of the: lower cut (left) and upper cut (right).

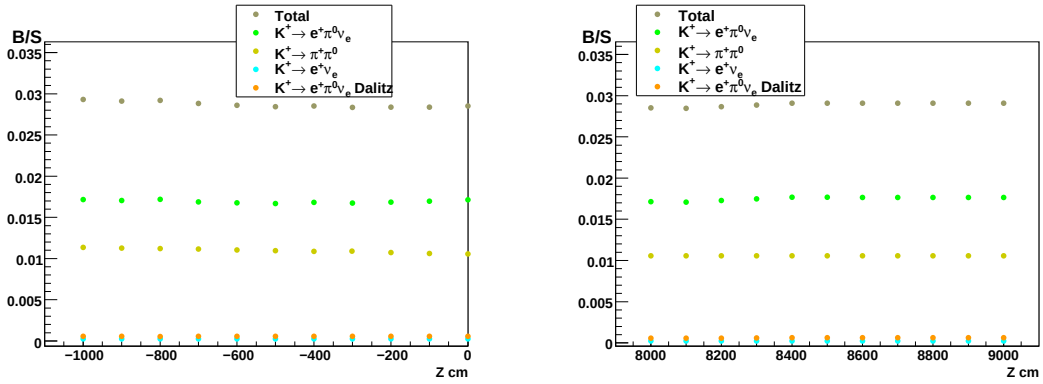

Figure 6.31: B/S ratio as a function of the: lower cut (left) and upper cut (right).

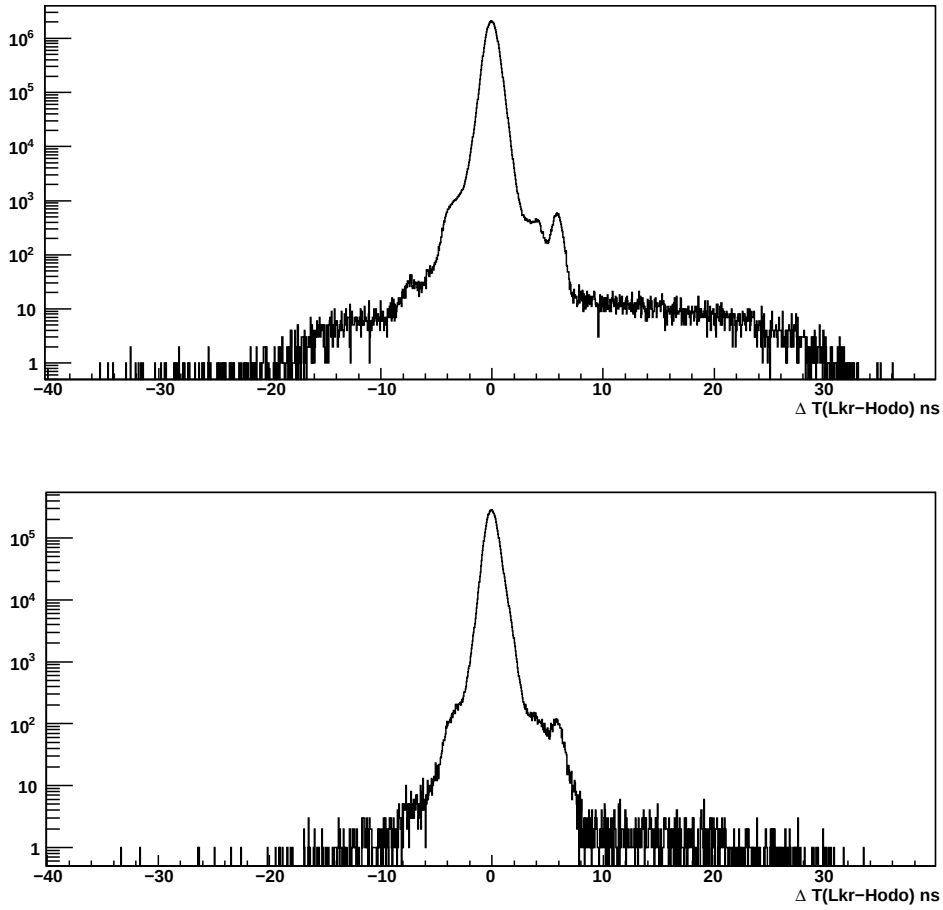

Figure 6.32: time difference between the electromagnetic cluster associated to the charged track, measured with the calorimeter, and the hodoscope time of the charged track, for Data events passing all the Ke3 selection cuts (top) and all the events passing the signal selection condition (excluding the squared missing mass cut to increase the statistic of the sample) (bottom).

the events passing the signal selection conditions (excluding the squared missing mass cut to increase the statistics of the sample) (bottom). From these distributions, the contamination, coming from accidentals, has been calculated. The time window used in the analysis is of 10 ns, between -5 ns and 5 ns, the residual accidental contamination has been evaluated integrating the distribution in a time window of 20 ns, between 10 ns and 30 ns, and then divided by two. For the Ke3 $\Delta T(Lkr - Hodo)$ distribution, figure 6.32 (top), the contamination is $\sim 3.2 \cdot 10^{-5}$; For the signal $\Delta T(Lkr - Hodo)$ distribution, figure 6.32 (bottom), the contamination is $\sim 3.3 \cdot 10^{-5}$. No corrections due to the accidental contribution has been applied considering that the effect is the same between the two selections and it cancels in the ratio for the BR evaluation.

A difference analysis approach is to take the charged track time meausured from the magnetic spectrometer; using the same number of σ for the timing cut, the result for the Branching Ratio computed with these conditions is:

$$BR(K^+ \to e^+\nu_e\gamma(SD+)) = (1.551 \pm 0.018_{stat} \pm 0.013_{sys^*}) \cdot 10^{-5}$$

The difference between this result and the one of equation 6.6 amaunts to $\sim 0.13\%$ of the Branching Ratio; it has been added to the systematic uncertainity.

6.6 Other systematic uncertainties

A first source of the systematic error is a residual MC/Data discrepancy in the background region of the order of $\sim 0.6\%$; in figure 6.33 the squared missing mass distribution is reported after the application of all the cuts and conditions of the signal selection. The value of the discrepancy has been taken from a linear fit of the distribution in the background region.

A second source takes into account the background due to the other $K^+ \to e^+\nu_e\gamma$ components, the SD- and the IB. As a consequence of the fact that there is no measurement of the Branching Ratio of the two components, for the background evaluation the theoretical prediction has been used, see table 1.1. They have not been considered in the total residual background estimation. Table 6.9 reports the contribution of the two components giving a B/S ratio of $\sim 7.9 \cdot 10^{-4}$ directly added to the systematic contribution.

Another source of systematic effects considers the hit filter procedure applied to solve the 1TRKLM problem in the trigger efficiency measurement for signal events (see section 6.1). Figure 6.34 shows the Data and MC distributions of the number of hits in the 4 drift chambers of the magnetic spectrometer; the Data distribution

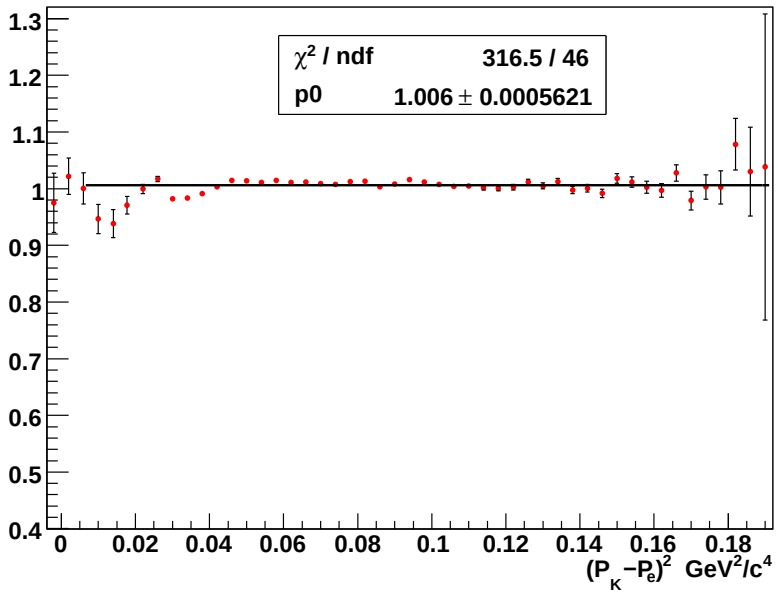

Figure 6.33: Squared missing mass MC/Data ratio at the end of signal selection without the $(P_K - P_e)^2$ cut.

Channel	N_{bg}
$K^+ \to e^+\nu\gamma(IB)$	(1.06 ± 0.02)
$K^+ \to e^+\nu\gamma(SD-)$	(5.48 ± 0.08)

Table 6.9: Background contribution of $K^+ \to e^+\nu_e\gamma$ IB and $K^+ \to e^+\nu_e\gamma$ SD-.

has been obtained using a sample selected with the signal selection without the invariant masses conditions and aquired from the $Q1 \times LKrMBias/100$ trigger condition (minimum bias trigger). The MC distribution has been obtained using Ke3 MC events.

The systematic contribution has been evaluated considering the probability to have a number of hits greater than 14 in all views of the drift chamber1, drift chamber3 and drift chamber4. This corresponds to select events inefficient for the 1TRKLM condition.

The results are, for the Data:

$$P_{Data} = 0.0523 \pm 0.0004$$

and for MC:

$$P_{MC} = 0.0642 \pm 0.0001$$

The difference between the two probabilities, $P_{MC} - P_{Data} \simeq 1.2\%$ has been added

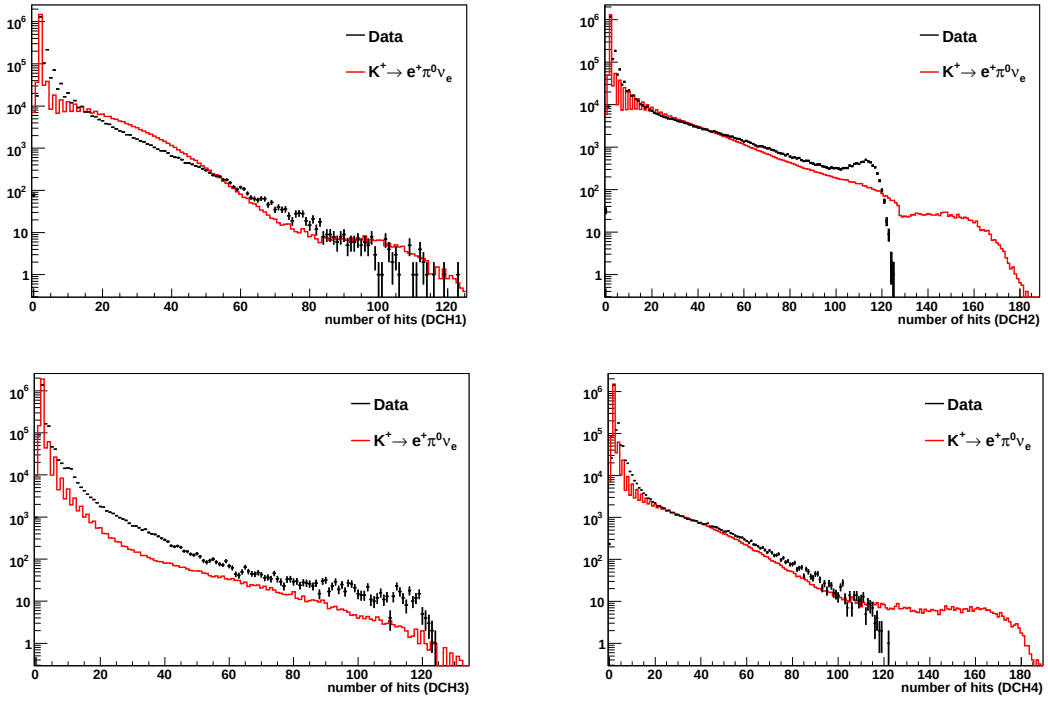

Figure 6.34: Data and MC distributions of the number of hits for the 4 drift chambers of the magnetic spectrometer.

to the systematic uncertainity.

Table 6.10 reports a summary of all the systematic uncertainties.

Contribution	$\Delta BR\ 10^{-7}$	%
$(P_K - P_e)^2$ cut	2.2	1.4
E_γ cut	0.2	0.2
lower Z cut	0.6	0.4
timing condition	0.2	0.1
hit filter procedure	1.9	1.2
Residual MC/Data discrepancy	0.9	0.6
$K^+ \to e^+\nu_e\gamma$ (SD-,IB) contribution	0.1	0.1
Total	3.1	2.0

Table 6.10: Summary of all the systematic uncertainties.

Conclusion

In this work an analysis of the BR of the $K^+ \to e^+\nu_e\gamma$ (SD+) has been discussed. The largest world sample ($\sim$ 8000 events) on this channel has been reconstructed among a restricted sample ($\sim$ 40%) of the Data collected by the NA62 (Phase I) experiment during the 2007 Data taking period.

The final result obtained for this measurement, using a signal MC simulation based on ChPT at $O(p^6)$ theoretical model, is:

$$BR(K^+ \to e^+\nu_e\gamma(SD+)) = (1.549 \pm 0.038) \cdot 10^{-5}$$

with a residual background contamination of $\sim 3\%$. This result, with an accuracy of $\sim 2.5\%$, is in agreement within $\sim 2\sigma$ with the recent result obtained by the KLOE collaboration. The comparison with the PDG value has been performed using a signal MC simulation based on ChPT at $O(p^4)$ and in a restricted kinamatical x region ($x > 0.2$); the two result are in good agreement within the errors. our measurements has improved the accuracy by a factor ~ 6.

A model independent measurement of the $K^+ \to e^+\nu_e\gamma$ (SD+) BR has been performed evaluating the acceptance as a function of the x variable. Integrating the obtained BR distribution the result is:

$$BR(K^+ \to e^+\nu_e\gamma(SD+)) = (1.54 \pm 0.07) \cdot 10^{-5}$$

in perfect agreement with the previous value.

This work has shown the eveidence of a non negligible contribution of the Chiral Perturbation Theory $O(p^6)$ term in the description of the $K^+ \to e^+\nu_e\gamma$ process and in the mean time the failure of the LFQM.

Appendix A

A.1 Cluster-track association for pions

The *CMC* doesn't perform a good simulation of the hadronic interactions in the electromagnetic calorimeter, as a consequence the energy released by a pion in the LKr is not well reproduced. As an example in figure A.1 has been reported the MC/Data comparison for the E/P ratio of pion interacting in the calorimeter. Moreover the overall probability to have a reconstructed cluster for pions in the LKr is wrong in the *CMC* simulation.

In the signal selection the cluster track association assumes a relevant importance, in fact, as explain in section 4.2 the positron-pion discrimination is performed applying a cut on the E/P distribution requiring $0.95 < E_{LKr}/P < 1.1$ for positrons.

Then in order to prevent acceptance problem related to not well simulated pion interactions in the LKr, in the Monte-Carlo with a charged pion in the final state the E/P cut hasn't been applied. To correctly evaluate the acceptance, the number of events reconstructed at the end of the selection has been rescaled for a factor obtained directly from the Datawith the procedure described in the following section.

A.1.1 The weighted technique

The probability for a pion to interact in the calorimeter and to produce a cluster with $0.95 < E_{LKr}/P < 1.1$ has been measured with a Data sample of pions collected with an ad-hoc selection reconstructing $K^+ \to \pi^+\pi^0$ events. The selection criterias have been taken the most possible similar to those of the signal selection. The events have been selected asking the same control trigger used for the trigger efficiency measurement. In fact the main trigger chain includes also the *L3* filter which has, among other conditions, also a cut on the E/P and then it is not useful for this study. The decay vertex conditions and the track momentum region selected are

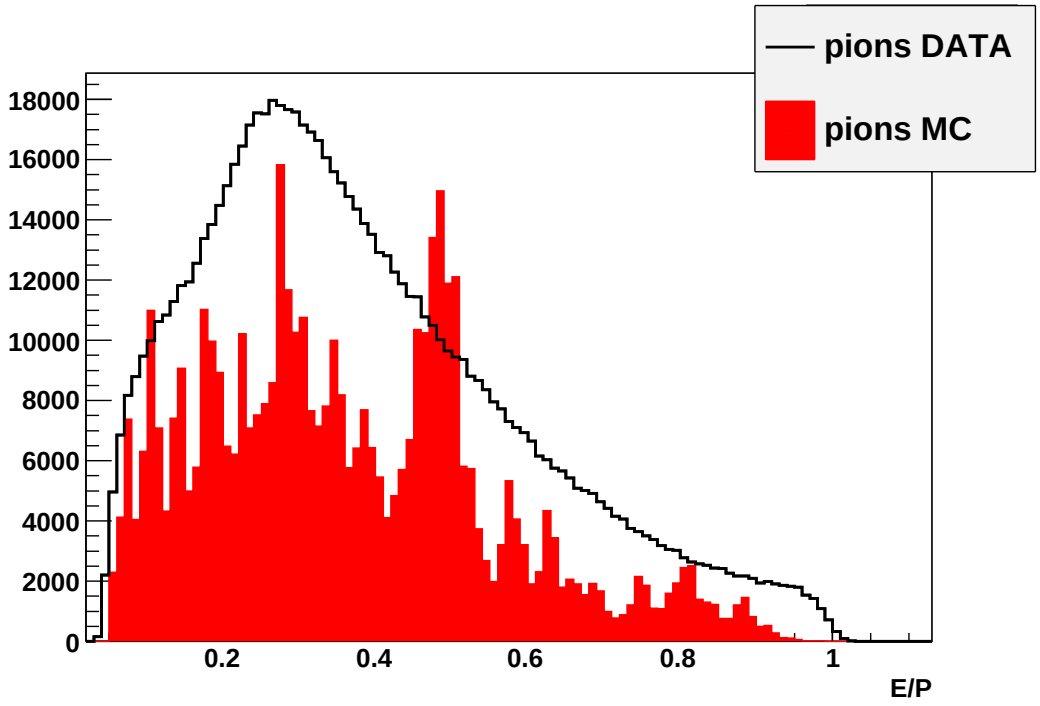

Figure A.1: The E/P distribution for pions: Data black line and MC red.

the same of the analysis. The π^0 has been reconstructed through the same conditions of section 5.1.1.

The probability has been measured in bin of track momentum with the following formula:

$$p(P_i) = \frac{N_i(E/P)}{N_i}$$

where $N_i(E/P)$ is the number of pions of momentum P_i with $0.95 < E_{LKr}/P < 1.1$ and N_i is the total number of pions selected with momentum P_i. The result has been reported in table A.1 and figure A.2.

For a given P_i the rescaling factor for the events has been taken from a gaussian distribution with the mean equal to $p(P_i)$ and with the sigma equal to the error associated to $p(P_i)$.

There is another measurement of this probability used by the collaboration to study the background of the $K^+ \to \pi^+\pi^0$ to the $K^+ \to e^+\nu_e$ for the measurement of the ratio R_K. In this case to measure the probability, $K_L \to \pi^+ e^- \bar{\nu_e}$ events are used. The Data used have been taken during a special run with a K_L beam. The selection used considers cuts comparale with the standard analysis for the R_K measurement. The results are reported in table A.2 and figure A.3. In figure A.4 the comparison between the two measurements of the probability to have a pion with $0.95 < E_{LKr}/P < 1.1$ is reported. The difference between the two probabilities,

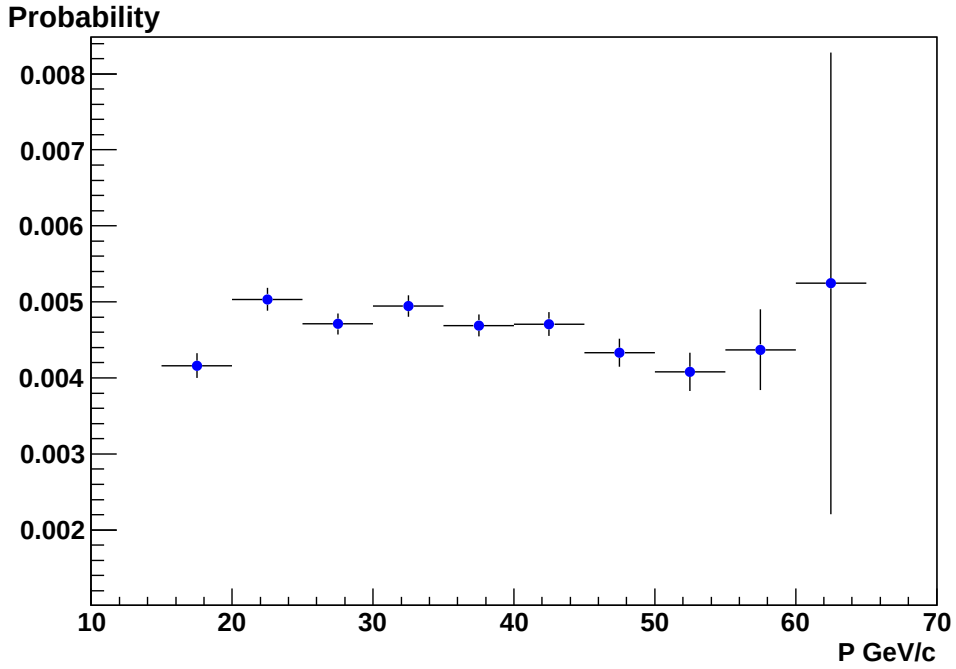

Figure A.2: Probability of a pion to produce a cluster in the electromagnetic calorimeter with $0.95 < E_{LKr}/P < 1.1$ measured with $K^+ \to \pi^+\pi^0$ events; every bin has a 5 GeV/c width.

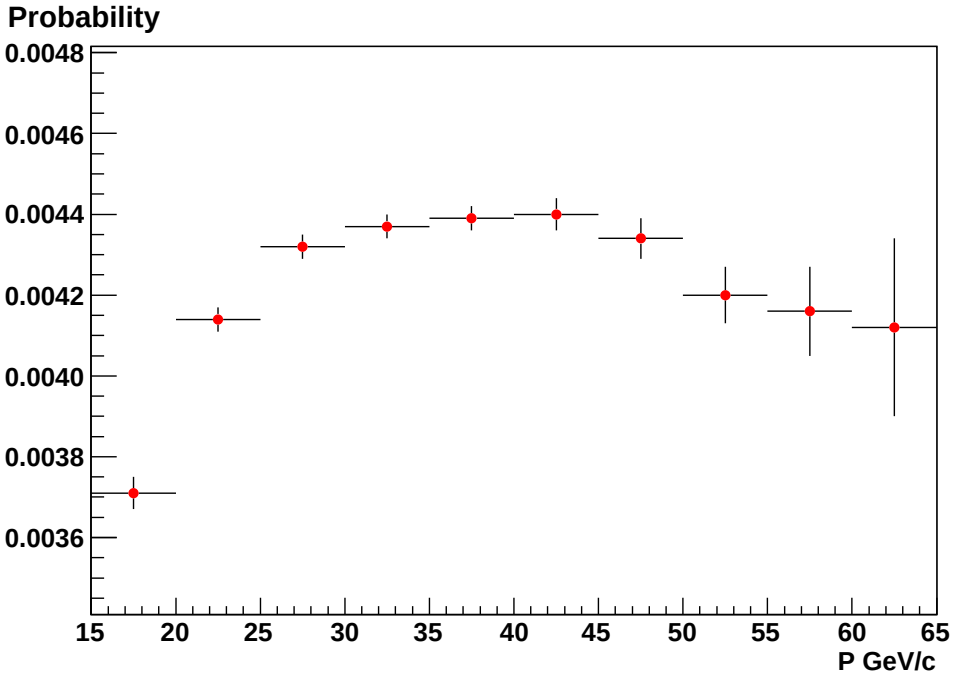

Figure A.3: Probability of a pion to produce a cluster in the electromagnetic calorimeter with $0.95 < E_{LKr}/P < 1.1$ measured with $K_L \to \pi^+ e^- \bar{\nu}_e$ events; every bin has a 5 GeV/c width.

P (GeV/c)	Probability	ΔProbability	ΔProbability/Probability (%)
15 to 20	0.00416	0.00016	4
20 to 25	0.00503	0.00015	3
25 to 30	0.00471	0.00014	3
30 to 35	0.00495	0.00014	3
35 to 40	0.00469	0.00014	3
40 to 45	0.00471	0.00016	3
45 to 50	0.00433	0.00018	4
50 to 55	0.0041	0.0003	7
55 to 60	0.0044	0.0005	11
60 to 65	0.005	0.003	60

Table A.1: Probability of a pion to produce a cluster in the calorimeter with $0.95 < E_{LKr}/P < 1.1$ measured with $K^+ \to \pi^+\pi^0$ events.

P (GeV/c)	Probability	ΔProbability	ΔProbability/Probability (%)
15 to 20	0.00371	0.00004	1
20 to 25	0.00414	0.00003	0.7
25 to 30	0.00432	0.00003	0.7
30 to 35	0.00437	0.00003	0.7
35 to 40	0.00439	0.00003	0.7
40 to 45	0.00440	0.00004	0.9
45 to 50	0.00434	0.00005	1
50 to 55	0.00420	0.00007	2
55 to 60	0.00416	0.00011	3
60 to 65	0.0041	0.0002	5

Table A.2: Probability of a pion to produce a cluster in the calorimeter with $0.95 < E_{LKr}/P < 1.1$ measured with $K_L \to \pi^+ e^- \bar{\nu_e}$ events.

figure A.4, is due to the different selections used for this study (the measurement depends strongly from the selection criterias).

A.2 Cluster-track association for muons

The simulation of the interaction of muons with the LKr suffers of the same problem encountered for the pions. With the muons the main problem is in the number of times that a particle interacting with the calorimeter produce an energy release with the right characteristics to be reconstructed as a cluster (section 2.6.1). For the evaluation of the acceptance for the MC with a muon in the final state has been applied the same procedure used for the pions. In this case the probability for a muon to produce a cluster with $0.95 < E_{LKr}/P < 1.1$ (mis-identified as a positron) has been measured with special run taken during the standard Data taking with a

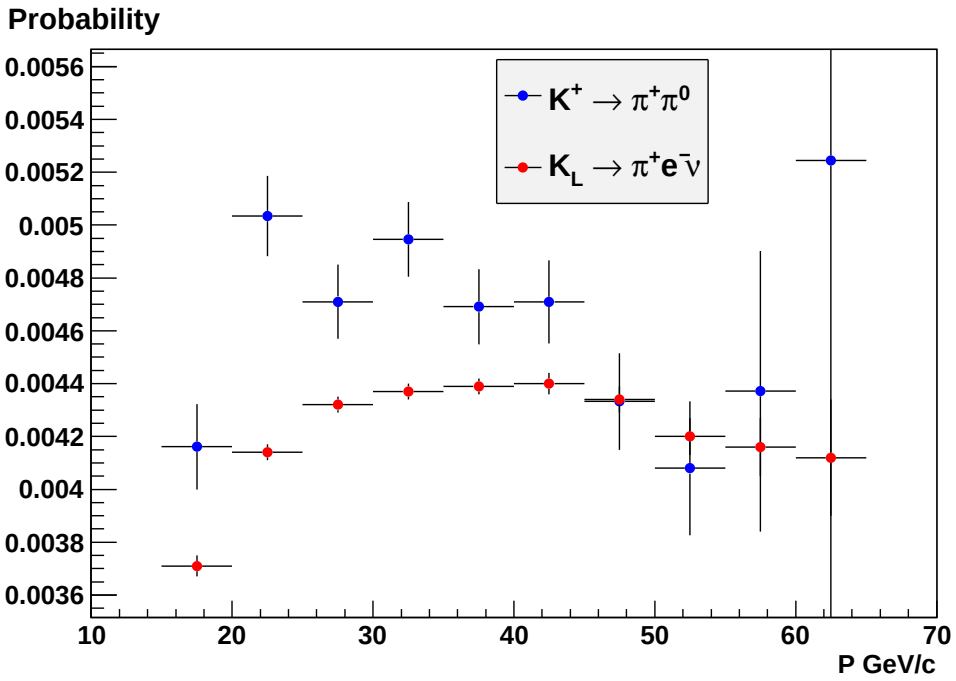

Figure A.4: Comparison between the two probability measurements.

muon beam. The results are reported in table A.3 and in figure A.5.

P (GeV/c)	Probability (10^{-6})	ΔProbability (10^{-6})	ΔProbability/Probability (%)
15 to 20	3.08	0.19	6
20 to 25	3.5	0.2	6
25 to 30	4.1	0.2	5
30 to 35	3.3	0.2	6
35 to 40	4.2	0.3	7
40 to 45	4.2	0.3	7
45 to 50	4.0	0.3	7
50 to 55	4.4	0.3	7
55 to 60	5.3	0.3	6
60 to 65	5.3	0.3	6

Table A.3: Probability of a muon to produce a cluster in the calorimeter with $0.95 < E_{LKr}/P < 1.1$.

A.2.1 The probability measurement

The measurement is based on the presence of a lead wall, positioned between the two planes of the charged hodoscope, before the LKr (covering $\sim 30\%$ of the LKr geometrical acceptance), used to stop all the particles except the muons. One good event is an event producing one track in the magnetic spectrometer, beeing in the

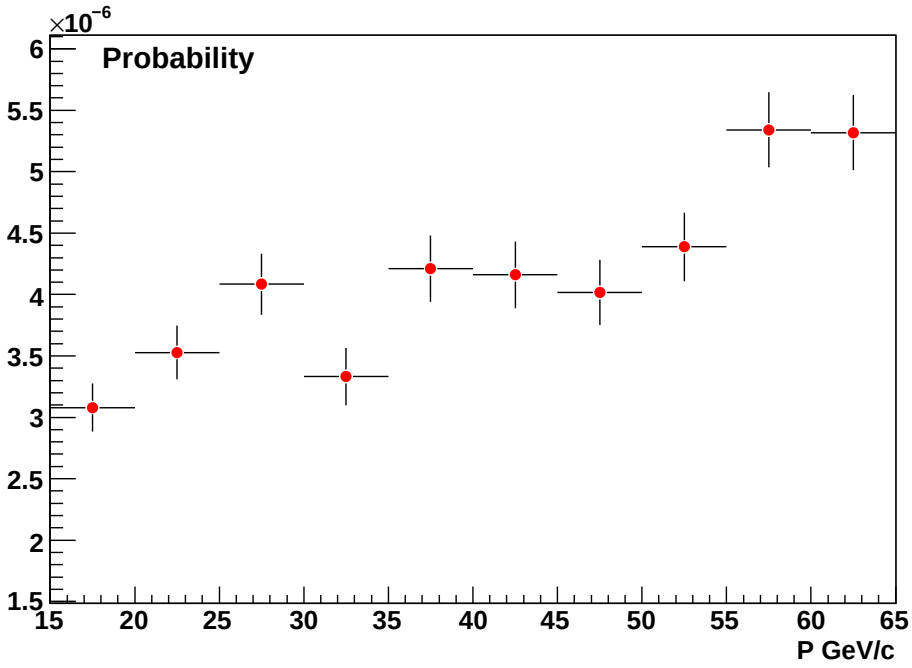

Figure A.5: Probability of a muon to produce a cluster in the calorimeter with $0.95 < E_{LKr}/P < 1.1$, every bin has a 5 GeV/c width.

geometrical acceptance of the lead wall and producing a signal in the second plane of the charged hodoscope compatible with a minimum ionizing particle (mip) to reject events with showers produced inside the lead wall.

The probability is the ratio between the events with $0.95 < E_{LKr}/P < 1.1$ and the total number of events selected by the conditions described before.

Bibliography

[1] D. J. Gross and F. Wilczek, Phys. Rev. Lett. **30** (1973) 1343.

[2] H. D. Politzer, Phys. Rev. Lett. **30** (1973) 1346.

[3] S. Weinberg, Physica A **96** (1979) 327.

[4] J. Gasser and H. Leutwyler, nnals Phys. **158** (1984) 142.

[5] M. Gell-Mann and Y. Ne'eman, *The Eightfold Way* (Benjamin,New York, 1964).

[6] J. Goldstone, Nuovo Cim. **19**, 154 (1961).

[7] J. Gasser and H. Leutwyler, Nucl. Phys. B **250**, 517 (1985).

[8] A. Pich, Int. J. Mod. Phys. A **20**, 1613 (2005).

[9] J. Wess and B. Zumino, Phys. Lett. B **37**, 95 (1971).

[10] E. Witten and H. Leutwyler, Nucl. Phys. B **223**, 422 (1983).

[11] P. A. Dirac, Rev. Mod. Phys. **21**, 392 (194).

[12] C. R. Ji and S. J. Rey, Phys. Rev. D **53**, 5815 (1996).

[13] H. M. Choi and C. R. Ji, Phys. Rev. D **58**, 071901 (1998).

[14] C. Amsler, *et al.* [Particle Data Group], Phys. Lett. B **667**, 1 (2008) and the 2009 online vertion.

[15] J. T. Goldman and W. J. Wilson, Phys. Rev. D **15**, 709 (1977).

[16] D. A. Bryman, *et al.*, Phys. Rept. **88**, 151 (1982).

[17] J. Bijnens, *et al.*, Nucl. Phys. B **396**, 81 (1993).

[18] C. Ametler, *et al.*, Phys. Lett. B **303**, 140 (1993).

[19] C. Q. Geng, I. L. Ho and T. H. Wu, Nucl. Phys. B **684**, 281 (2004).

[20] C. H. Chen, C. Q. Geng and C. C. Lih, Phys. Rev. D **77**, 014004 (2008).

[21] C. Q. Geng, C. C. Lih and C. C. Liu, Phys. Rev. D **62**, 034019 (2000).

[22] C. Q. Geng, C. C. Lih and W. M. Zhang, Phys. Rev. D **56**, 5697 (1998).

[23] O. Strandberg, arXiv:hep-ph/0302064.

[24] G. Amoros, J. Bijnens and P. Talavera, Nucl. Phys. B **602**, 87 (2001).

[25] M. Knecht and A. Nyffeler, Eur. Phys. J. C **21**, 659 (2001).

[26] K. S. Heard, *et al.*, Phys. Lett. B **55**, 324 (1975).

[27] J. Heintze, *et al.*, Nucl. Phys. B **149**, 365 (1979).

[28] F. Ambrosino *et al.* [KLOE Collaboration], arXiv:hep-ex/0907.3594v2.

[29] V. Fanti *et al.* [NA48 Collaboration], Nucl. Instrum. Meth. A **574** (2007) 433.

[30] V. Fanti *et al.* [NA48 Collaboration], *Prposal for a Precision Measurement of* ϵ'/ϵ *in CP violating* $K^0 \to 2\pi$ *decays* CERN-SPSC-90-22 (1990).

[31] J. R. Batley *et al.* [NA48/2 Collaboration], *Prposal for a Precision Measurement of Charged Kaon Decay Parameters with an Extended NA48 Setup* CERN-SPSC-2000-003 (2000)

[32] V. Cirigliano and I. Rosell, Phys. Rev. Lett. **99**, (2007) 231801.

[33] A. Masiero, P. Petronzio and P. Paradisi, Phys. Rev. D **74**, 011701 (2006).

[34] G. Anelli *Proposal to Measure the Rare Decay* $K^+ \to \pi^+\nu\bar{\nu}$ *at CERN SPS* CERN-SPSC-2005-013 (2005)

[35] G. Anelli *et al.* [NA62 Collaboration], *NA62-P326 Status Report* CERN-SPSC-2007-035 (2007)

[36] A. V. Artamonov *et al.* [E949 Collaboration], Phys. Rev. Lett. **101**, (2008) 191802.

[37] R. Arcidiacono *et al.*, Nucl. Instrum. Meth. A **443** (2000) 20.

[38] C. Biino *et al.*, *COmPACT 7.3* User's Guide, (2007).

[39] M. De Beer, NASIM User's Guide, NA48 Internal Note, NA48-00-23, (2000)

[40] R. Brun *et al. Detector Description and Simulation Tool* CERN Program Library Long Writeup W5013.

[41] B. Bloch-Devaux, Alpha and Beta correction for NA48/2 simulated events, NA48 Internal Note, NA48-05-05, (2005)

[42] M. Paterno, D0 Note N. 2861 (1996), FNAL.